PIEZOELECTRIC FUSED SILICA RESONATORS FOR TIMING REFERENCES

by

Adam Edmund Peczalski

A dissertation submitted in partial fulfillment
of the requirements for the degree of
Doctor of Philosophy
(Electrical Engineering)
In the University of Michigan
2016

Doctoral Committee:

Associate Professor Mina Rais-Zadeh, Chair
Professor Yogesh Gianchandani
Professor Karl Grosh
Professor Khalil Najafi

© Adam Peczalski

All rights reserved

2016

To Holly

And My Parents

Acknowledgements

I would like to start by thanking by advisor, Professor Mina Rais-Zadeh, for her support throughout my graduate career. Her support, advice, and patience through the years has made the work presented here possible. I also want to thank my thesis committee members, Professor Yogesh Gianchandani, Professor Karl Grosh, and Professor Khalil Najafi for their patience and assistance through coursework, advising, and research over the years. The support you all have provided is extremely appreciated and was critical to my success.

I would also like to thank my group members, both past and present, for the comradery and assistance they have provided over the years. They have served as my adoptive family for my years spent in Michigan, and I am extremely thankful for their time. Yonghyun, Zhengzheng, Vikrant, and Vikram all welcomed me into the group with open arms and made my first few years that much more enjoyable. Azadeh arrived in the group shortly before I did, but her cheerfulness and positive attitude through the coursework, as well as the natural ups and downs of research has made my graduate career all the better. More recently, the addition of Muzhi, Mohsen, and Milad continues the tradition of friendliness and comradery, and I am thankful for the conversations and events they enabled. An additional thanks to the post-doctoral students in our group, Feng, Roozbeh, and Haoshen, who have been extremely generous with their ideas, time, and company. You all have contributed to making the thesis possible.

The work done here would not have been possible without the help of the staff at the Lurie Nanofabrication Facility at the University of Michigan. The consistently helpful and understanding

staff have been invaluable in achieving the fabrication described in this work, and without them none of this would have been possible. I thank the staff for their infinite patience while fixing tools, cleaning up after my messes, and going along with my crazy schemes. Many of my colleges in the cleanroom have been extremely helpful in my research as well, with an especially big thank you to Yi Yuan, Dr. Zongliang Cao, Dr. Katherine Knisely, Dr. Zhengzheng Wu, and Dr. Vikram Thakar. Your efforts have been a major factor in my success and are much appreciated.

A large thank you to my friends at the University of Michigan, too numerous to name individually. Your company, distraction, and frequent coffee breaks were the highlight of my days. I want to give an especially thank you to Kevin Owen, David Sebastian, and more recently Tal Nagourney for keeping me alive and fed through many late nights of fabrication and providing adventures away from work when needed. I hope this is only the beginning of our time together, and I look forward to many more years of fun.

A final thank you to my family for their support through the years, I would not have made it anywhere close to here without your support, patience, and encouragement. An especially large thank you to my wife Holly, whose patience and understanding during our long period of separation have enabled the opportunities I have today. I look forward to many more years spent in your company.

Table of Contents

Dedication ii

Acknowledgements iii

List of Figures viii

List of Tables xviii

List of Abbreviations xx

Abstract xxiii

Chapter 1: Introduction 1

- **Motivation** 1
- **Applications for Miniaturized Timing References** 3
- **Current State-of-the-Art Timing References** 5
- **Fused Silica as a Resonant Material** 6
- **Quality Factor and Loss Mechanisms** 7
- **Resonator Actuation Methods** 11
- **Temperature Compensation of Resonators** 14
- **Dual-Mode Resonators** 15
- **Research Objectives and Contribution** 16
- **Organization** 18

Chapter 2: Piezoelectric Fused Silica Resonators 26

Fused Silica Resonator Considerations 27
Fabrication of Fused Silica Resonators 28
Fused Silica Dogbone Resonator Design 32
Simulation and Optimization of Dogbone Devices 34
Measured AlN-on-Silica Results 36

Chapter 3: Loss Effects in Fused Silica Resonators 47

TED in Single Material Resonators 47
TED in Multi-Layer Resonators 48
PZT-on-Silica Resonators 53
AlN-on-Silica Sidewall-Smoothed Resonators 57
Alternate Loss Mechanisms in Fused Silica Resonators 61
Charge Redistribution Loss in Piezoelectric Resonators 63
Modeling of Charge Redistribution Loss 66
Experimental Verification of Charge Redistribution Loss 68
Measurement of Charge Redistribution Variations 72

Chapter 4: Temperature Compensation of Fused Silica 79

Active Temperature Compensation 79
Passive Temperature Compensation in Fused Silica 82
Passive Temperature Compensation with Nickel-Refilled Trenches 84
Combining Passive and Active Compensation Methods 91

Chapter 5: Dual-Mode Fused Silica Resonators 97

Acoustic Phonon Trapping 98
Design of Dual-Mode Phonon Trap Devices 100
Temperature Sensitivity of Dual-Mode Phonon Trap Resonators 102

Fabrication of Dual-Mode Phonon Trap Resonators 104
Measured Results of Dual-Mode Phonon Trap Resonators 107

Chapter 6: Summary and Future Work 110

Experimental Verification of Charge Redistribution 111
Implementation of Dual-Mode Acoustically Engineered Oscillators 112
Dual-Mode Oscillators for Use in Ovenized Architecture 116

List of Figures

Fig. 1.1: (Left) Photograph of a fabricated inertial navigation platform on a U.S. Penny. (Right) A SEM view of the stacked platform showing multiple layers containing the inertial sensors. Images adapted from [10]. 4

Fig. 1.2: Example resonator response demonstrating a common method of calculating Q from measured results. 8

Fig. 2.1: Fabrication flow of the piezoelectric-on-silica resonators. 29

Fig. 2.2: SEM image of a fabricated AlN-on-silica dogbone resonator. The white scale bar is 500 µm in length. 31

Fig. 2.3: (Left) A cross-section view of the fused silica DRIE trench profile. Note the trapezoidal shape of the center tether beam. Image adapted from [20]. (Right) A cross-section view of a DRIE trench showing the roughness introduced to the trench sidewall during the etch process. The white scale bars are 10 µm in length. 31

Fig. 2.4: 3-D model of the piezoelectric-on-silica MEMS resonator design and mode shapes of in-phase and out-of-plane coupled radial extensional mode. 32

Fig. 2.5: Dimensions of the fused silica dogbone design. The piezoelectric stack dimensions are shown on the right. 34

Fig. 2.6: Measured S_{21} response and mode shape of an in-phase (right) and out-of-phase (left) fused silica dogbone resonator. Inset shows a SEM of a fabricated resonator with labeled inputs. Background shows simulated mode shape for each mode.. 39

Fig. 2.7: Measured S_{21} responses for an in-phase shear mode and mode shape at 2.9 MHz (left) and a third-order radial extensional response and mode shape at 16.39 MHz (right). Images adapted from [20]. 39

Fig. 2.8: Measured power handling of a radial extensional fused silica resonator showing a power-handling higher than -5 dBm. Background shows simulated mode shape. Image adapted from [20]. 40

Fig. 2.9: Measured frequency shift via temperature for three different modes on a fabricated fused silica resonator. Note that the temperature sensitivity in uncompensated silica is substantially higher than that found in silicon. Image adapted from [20]. 40

Fig. 2.10: Measured frequency stability (aging) for the radial extensional mode of an AlN-on-silica resonator over a 98-hour period. The first two hours from the 100-hour measurement period were excluded for device burn-in. The total frequency drift over the measurement period was 536 Hz (109 ppm), or if only the last 60 hours are considered a total drift of 257 Hz (52 ppm) is measured. 42

Fig. 3.1: Comparison of the Q_{TED} for a pure silica beam versus a silica beam with a 1 µm AlN film. Note the frequency decrease in the Q minima for the pure beam and the order of magnitude increase in Q_{TED}. 50

Fig. 3.2: Parameter sweep plots of Q_{TED} versus angular frequency. A 1 µm AlN film on a 50 µm silica beam has one material parameter of the AlN film swept from low to high. Inset shows the TED damping for the same beam over a normalized frequency. a.) Sweep of Young's Modulus from 50 GPa to 500 GPa.in 50 GPa increments b.) Sweep of thermal coefficient of expansion (CTE) from 0.5×10^{-6} to 5×10^{-6} in 0.5×10^{-6} increments. c.) Sweep of density from 500 kg/m^3 to 5,000 kg/m^3 in 500 kg/m^3 increments. d.) Sweep of thermal conductivity from 10 W/mK to 100 W/mK in 10 W/mK increments. 51

Fig. 3.3: Analytical Q_{TED} comparison for a 1 µm AlN film or a 1 µm PZT film on a 50 µm silica beam. Inset shows a schematic of the AlN-on-silica beam. Note that as predicted the PZT-on-silica beam predicts a substantially better Q_{TED} than the AlN-on-silica beam. 53

Fig. 3.4: Fabrication flow for the PZT-on-silica process. The piezoelectric stack is blanket deposited and then patterned to create ground contact and routing as necessary. 55

Fig. 3.5: Measured S-parameter response for an in-phase PZT-on-silica resonator with inserts demonstrating simulated mode shape and optical micrograph image. The center frequency is 4.8 MHz, with a Q of 17,849 and a post-processing insertion loss of 56 dB. 57

Fig. 3.6: Fabrication flow for the sidewall-smoothed AlN-on-silica resonators. This flow utilizes a fused silica DRIE-first approach to smooth sidewalls through thermal oxidation and etching of LPCVD polysilicon. 58

Fig. 3.7: SEM images of silica DRIE sidewalls pre (left) and post (right) sidewall smoothing with insets highlighting zoomed view of striations. Scale bars are 10 µm in length. Average sidewall roughness is measured to be reduced to 165 nm from 350 nm using this smoothing process. 60

Fig. 3.8: Measured S-parameter response for an in-phase AlN-on-silica sidewall-smoothed resonator. Center frequency is measured at 5.01 MHz with a Q of 17,567 and an insertion loss of 17.2 dB. Inset shows a labeled SEM image of a fabricated resonator, while simulated mode shape is displayed in the background. 61

Fig. 3.9: (Top) A schematic outlining the charge redistribution concept for a one-port piezoelectric resonator. The width extensional mode of a resonator is actuated through a piezoelectric stack on a TPoS structure. Time t=0 is chosen to be the point of full device contraction. (Bottom) A graphical representation of the motional charge created by the piezoelectric layer during a harmonic cycle. A cross-sectional cut of the resonator width is shown, with cross-sectional mode shapes shown at each time point. Figures adapted from [19]. 66

Fig. 3.10: Simulated X-directional strain profile for an AlN- and PZT-on-silica dogbone resonator. The non-uniform strain gradient causes a non-uniform charge gradient which redistributes during the harmonic cycle, causing loss. Differences in loss between the AlN- and PZT-on-silica are due to the larger electromechanical coupling coefficient of PZT over AlN, causing larger motional charge gradients. Insert shows simulated mode shape with labeled direction of plotted X-directional strain. 67

Fig. 3.11: Schematic and simulated strain profile for each of the three charge redistribution designs. (Left) A dual-tined flexural mode creates a strain gradient near the center coupling beam. The designed mode has a resonance frequency of 1 MHz (Middle) A length extensional mode with a resonance frequency of 10 MHz. The strain profile of these resonators is maximum at the center and tapers off toward the edge. (Right) A dogbone resonator in the fundamental radial-extensional

mode at 10 MHz. The strain profile of these devices is relatively uniform across its length, but slowly decreases from inner to outer radius. 69

Fig. 3.12: Schematic of designs for total coverage variations. The base design, shown in Fig. 3.11, has the least electrode coverage with these two variations showing more top metal coverage. It is expected that these devices show lower Q_{CR} as compared to the base designs. 70

Fig. 3.13: Schematic of designs for equivalent area variations. Each design has equivalent area to the base design in Fig. 3.11 but covers a wider strain gradient on the device. It is expected that these devices show lower Q_{CR} as compared to the base designs. 71

Fig. 3.14: Schematic of designs for equivalent k_t^2 variations. Each design has the same amount of motional charge under the electrodes as the base design shown in Fig. 3.11, but covers a much wider gradient. It is expected that these devices show lower Q_{CR} as compared to the base designs. Due to the relatively low gradient seen in the dogbone devices on the right, it was not possible to compare the equivalent K_t^2 design to the base. Instead, the two designs compare directly against each other. 71

Fig. 3.15: Fabrication flow of the charge redistribution devices with schematic showing cross-section details. The devices have a highly doped 20 μm substrate layer with 1 μm of AlN and 75 nm of Al for metal routing. No ground layer is required due to the low resistivity of the silicon substrate, reducing potential interface losses. 72

Fig. 4.1: SEM image of a fabricated fused silica ovenized platform. The platform is isolated from the substrate with long, thin isolation beams and heated through the use of a thin metal heating strip along the outside edge of the platform. An RTD in the center of the platform acts as the

temperature sensor, while the reference resonator provides the timing signal. Image adapted from [13]. 80

Fig. 4.2: Simulated COMSOL temperature distribution of a fused silicon ovenized platform. The outside temperature is set at 233K, the platform is heated with 4.3 mW of driving power through the heating strip, and the resonator is driven under 40 μW of oscillation power. The large temperature difference between the RTD and the resonator body is caused by the driving power and large thermal resistance of the dogbone tethers. Image is adapted from [13]........ 81

Fig. 4.3: Schematic and simulated mode shapes for the temperature compensated fundamental radial-extensional dogbone devices. The nickel-refilled trenches are placed in the center of each ring to maintain symmetry and maximize strain density across the trench. The simulation data, including predicted TCF, for both trench variations is included. Nickel TCE is assumed to be of -600 ppm/K for these simulations. The nickel trench depth was chosen to be 30 μm out of the 50 μm device thickness, with two different trench widths of 20 μm and 35 μm. 84

Fig. 4.4: Simulated TCF design space for the temperature compensated dogbone resonators with varied compensation trench and depth and width. Starred data points correspond to the selected dimensions for the fabricated resonators outlined in Fig. 4.3. Nickel is simulated with a TCE of -600 ppm/K. Inset shown sketch of compensated resonator. 85

Fig. 4.5: Fabrication flow for the temperature compensated nickel-refilled embedded trench AlN-on-silica resonators 86

Fig. 4.6: (Left) A SEM image of a fabricated temperature compensated AlN-on-silica resonator. (Top Right) A zoomed in image of a single dogbone ring with the embedded nickel-refilled trench

outlined in red. (Bottom Right) A cross-section SEM of a nickel-refilled trench showing complete refill of the trench. The measured depth of this trench was shown to be 20 μm, 10 μm shallower than designed. 88

Fig. 4.7: S-parameter response and measured parameters for a compensated, undercompensated, and uncompensated dogbone in the fundamental radial extensional mode. Background image shows the simulated mode shape. 88

Fig. 4.8: Measured temperature sensitivity of the fabricated temperature compensated AlN-on-silica resonators. The TCF of three designs are shown, the uncompensated reference resonator, the undercompensated trench design, and the fully compensated trench design. The inset shows the simulated mode shape. 89

Fig. 4.9: Simulated TCF design space for the fitted temperature compensated AlN-on-silica devices with the device schematic in the inset. With data taken from SEM geometry measurements, the trench depth was reduced to 20 μm from 30, and the overall device thickness was reduced to 40 μm from 50. The assumed nickel TCE for these simulations was -200 ppm/K. It is important to note that complete compensation of these devices will require a large amount of added material. 90

Fig. 4.10: Measured TCF results of a fabricated temperature compensated AlN-on-silica device with multiple modes on the same device. The first mode, a traditional fundamental radial extensional mode, shows a TCF of +50 ppm/K. In comparison, a second mode on the same device, thought to be a third-order radial extensional mode, has a TCF of +21 ppm/K. There is a TCF different of +29 ppm/K between modes on the same device volume, which opens up a potential application as dual-mode resonators. 92

Fig. 5.1: Simulated dispersion curve (wavenumber versus frequency) for a selection of possible branches for an infinite beam 62.5 µm wide and 20 µm thick. The vertical black line notes the line between propagating (positive K) waves and evanescent (negative K) waves. Inset shows the simulated mode shapes for each wave branch, from top to bottom: a fundamental flexural mode, a fundamental width extensional mode, and a fundamental shear mode. 98

Fig. 5.2: (Left) Simulated dispersion curves for a selection of possible branches for a series of infinite beams 57 µm to 62.5 µm wide and 20 µm thick. Insets show the simulated mode shapes for each branch. (Right) A zoomed view of the flexural branch for a device that slowly decreases in width. Each dispersion color represents a specific region on the geometry shown above, effectively synthesizing a propagating mode with a number of evanescent modes. The inset shows the simulated mode shape of the flexural branch. The vertical black line notes the line between propagating (positive K) waves and evanescent (negative K) waves for both images................ 99

Fig. 5.3: A schematic of the dual-mode phonon trap resonator. The overall length of the device is 900 µm, a 250 µm tether region which is 116 µm wide, a 100 µm transition region that slowly transfers from 116 µm to the final width of 125 µm for the main phonon trapped region, which is 200 µm in length. The device is 20 µm thick with a 1 µm thick AlN piezoelectric layer. The simulated mode shapes for each trapped mode are shown with their respective frequency....... 101

Fig. 5.4: Simulated strain density for the designed dual-mode phonon trap resonators versus position across the device. Each strain line is matched to a simulated mode shape for reference. Note that the majority of energy in each mode is isolated in the center of the device, demonstrating successful phonon trapping... 101

Fig. 5.5: Simulated TCF for each dispersion branch. Inset shows simulated mode shape for each branch. Note how the evanescent mode shows a large shift in TCF over the evanescent modes. This allows for some TCF modification of the synthesized mode. 103

Fig. 5.6: Process fabrication flow for the silicon dual-mode phonon trap resonators. 105

Fig. 5.7: SEM image of a fabricated dual-mode phonon trap resonator. Input and output pads are labeled with a ground pad that allows access to the highly doped silicon layer......................... 106

Fig. 5.8: Measured S-parameters for the fabricated dual-mode phonon trap resonators. Background shows the simulated mode shapes and measured resonator parameters. 106

Fig. 5.9: Measured frequency drift on a dual-mode phonon trapped resonator due to temperature fluctuation. Inset shows the simulated mode shape and extracted turnover temperature from second-order polynomial fitting. At the WE mode's turnover point the equivalent TCF of the flexural mode is extracted to be -6.89 ppm/K.. 107

Fig. 6.1: A schematic of a dual-mode oscillator made from a single dual-mode phonon trapped resonator. Each amplification path is isolated through the use of a bandpass filter, leading to two separate output frequency signals with different temperature characteristics. 112

Fig. 6.2: Filter response for the 11 MHz lowpass filter and the 31 MHz bandpass filters provided through Mini-Circuits. Insertion loss is plotted versus frequency for both branches, while photographs of both surface mount filters and generalized layout for the LC filters are shown below. Images for lowpass filter adapted from [1] and 31 MHz filter adapted from [2]. 113

Fig. 6.3: Dual-mode circuit layout for the fabricated acoustically engineered resonators. Top branch is for the 11 MHz resonance mode and has two-stage amplification for extra gain. Bottom branch is for the 31 MHz mode and has only single stage amplification. Both output stages use a buffer prior to oscillator output. 114

Fig. 6.4: Frequency spectrum measurement of the 31 MHz oscillator around its carrier frequency. The major harmonic frequency and powers are included in the left inset. Right inset shows a time domain measurements of the oscillator output showing a sine wave with little harmonic influence. 115

Fig. 6.5: A schematic for an ovenized platform architecture utilizing a phase detector as part of a PLL. The accuracy of this system increases as the TCF difference between the two modes increases. Image adapted from [6]. 117

List of Tables

Table 1.1: Some Applications for Miniaturized Timing References 3

Table 1.2: Comparison Between State-of-the-Art Commericial Timing References 6

Table 2.1: COMSOL Simulation Parameters for Fused Silica Resonators 33

Table 2.2: COMSOL Simulated Performance for Various Piezoelectric Layers (Radial Extensional Mode) 36

Table 3.1: Material Constants Used in COMSOL Simulations 54

Table 3.2: COMSOL Simulation Results for QTED of Fused Silica Resonators in Radial Extensional Mode 54

Table 3.3: Summary of Measured Performance for Fabrication Piezoelectric-on-Silica Resonators 62

Table 3.4: Combined Simulation Results of Multiple Loss Mechanisms for Piezoelectric-on-Silica Resonators 68

Table 3.5: Measured and Simulated Performance Results for Flexural Charge Redistribution Resonators 74

Table 3.6: Measured and Simulated Performance Results for Dogbone Charge Redistribution Resonators 74

Table 3.7: Measured and Simulated Performance Results for Length Extensional Charge Redistribution Resonators 74

Table 5.1: Material Parameters of Doped Silicon and AlN for Phonon Trap Simulations 104

List of Abbreviations

Abbreviation	*Definition*
Al	Aluminum
AlN	Aluminum Nitride
ARL	Army Research Laboratory
Au	Gold
BAW	Bulk Acoustic Wave
BHF	Buffered Hydrofluoric Acid
BJT	Bipolar Junction Transistor
BOX	Buried Oxide Layer
CMOS	Complementary Metal Oxide Semiconductor
Cr	Chrome
CSD	Chemical Solution Deposition
CTE	Coefficient of Thermal Expansion
DRIE	Deep Reactive Ion Etch
FEM	Finite Element Modeling
GaN	Gallium Nitride
GPS	Global Positioning System
HRG	Hemispherical Resonator Gyroscope

IFF	Interrogate Friend or Foe
IoT	Internet of Things
IPA	Isopropyl Alcohol
LPCVD	Low-Pressure Chemical Vapor Deposition
MEMS	Microelectromechanical Systems
Mo	Molybdenum
PCB	Printed Circuit Board
PECVD	Plasma Enhanced Chemical Vapor Deposition
PML	Perfectly Matched Layer
Pt	Platinum
PZT	Lead Zirconate Titanate
Q	Quality Factor
RIE	Reactive Ion Etch
RTD	Resistance Temperature Detectors
SEM	Scanning Electron Microscope
SOI	Silicon-on-Insulator
TCE	Temperature Coefficient of Elasticity
TCF	Temperature Coefficient of Frequency
TED	Thermoelastic Damping
TIA	Trans-impedance Amplifier
TPoS	Thin-Piezoelectric-on-Substrate

TTV	Total Thickness Variation
WE	Width Extensional
ZnO	Zinc Oxide

ABSTRACT

Piezoelectric Fused Silica Resonators for Timing Applications

by

Adam Edmund Peczalski

Chair: Associate Professor Mina Rais-Zadeh

MEMS resonators have the capability to match or exceed the performance of state-of-the-art quartz timing references at a fraction of the size, power, and cost. To enable this capability, this work investigates the use of fused silica as a substrate for piezoelectrically actuated resonators for applications in timing references.

This thesis presents the design and fabrication of a piezoelectrically actuated fused silica resonator. The fabricated resonators show a quality factor (*Q)* of 19,671 at 4.96 MHz with an insertion loss of 16.9 dB, and is the first reported example of a piezoelectrically actuated fused silica resonator in literature. An in-depth investigation into loss mechanisms in fused silica is performed in order to identify and address the major losses in the device and maximize potential performance. Multiple experimental and analytical investigations are presented, with a new form of loss, known as charge redistribution, presented as a possible dominant loss in these piezoelectric resonators. This loss mechanism is analytically modeled and simulated to have a *Q* of 25,100, within 20% of the experimentally measured devices.

The temperature sensitivity of fused silica is also addressed; as fused silica shows a temperature coefficient of elasticity almost three times higher than that shown in uncompensated silicon. Both active and passive methods of temperature compensation are implemented, including a fused silica ovenized platform and nickel-refilled trenches for temperature compensation. The nickel-refilled trenches are shown to reduce temperature sensitivity in piezoelectrically actuated fused silica resonators from 78 ppm/K to 50 ppm/K, with larger compensation possible but complete compensation infeasible from passive techniques alone. From this, a dual-mode system is proposed for use in ovenized systems where two modes are simultaneously activated in a single device volume. In this system, one mode acts as a stable reference frequency and the second mode acts as a temperature sensor, allowing for extremely accurate ovenization. A silicon-based prototype is developed, showing a +14 ppm/K temperature difference between the two modes, with additional temperature differential possible through the addition of material-based passive compensation.

Chapter 1: Introduction

Motivation

Accurate timekeeping has been a focus of scientific attention for hundreds of years. From the days of nautical exploration, where timekeeping was an essential part of navigation, to modern days' Global Positioning System (GPS) and communication requirements for nanosecond accuracy, the demand for accurate timing references has been relentlessly driven forward. Modern technology uses both quartz crystals and atomic clocks to fit their high-performance timing needs, but there is a distinct lack of small, precise, low-cost timing references to meet the rising demand for miniaturized applications such as wearable sensors, mobile devices, and small science platforms like picosatellites. For currently available technology, atomic clocks are extremely accurate and represent the pinnacle of timing accuracy. However, they are large, power hungry, and very expensive, with the cheapest units running in the thousands of dollars. Quartz crystals, on the other hand, have become the ubiquitous timing reference of the modern era, seeing use in cell phones, watches, automobiles, and numerous other applications [1]. Nevertheless, these crystals are difficult to micro-machine and therefore are having troubles meeting the size and power requirements for the next generation of miniaturized devices.

Microelectromechanical systems, or MEMS, can address the need for small and low power timing references. This technology leverages silicon semiconductor fabrication technology to achieve micrometer-scale devices that are competitive with the performance offered by quartz crystals. MEMS devices have the added benefit of batch-fabrication, allowing for mass production

and economy of scale to drive cost to or below the established market price of quartz crystals. While attempts have been made towards the miniaturization and batch fabrication of quartz, performance and throughput have so far been difficult to achieve [2]. Conversely, silicon MEMS resonators have had a number of commercialization attempts and are beginning to see success in the industrial market [3]. This initial success has opened up the market for more niche MEMS alternatives, such as ovenized resonators. These ovenized MEMS resonators would be used in applications where environmental robustness and extremely high performance are required, but cannot come at the cost of size, power, and weight. One such application that is seeing increasing interest is in picosatellites, small space science or communication stations with an emphasis on low size and cost [4]. Other potential applications include wearable electronics, disposable sensors, inertial navigation in GPS-denied environments, and in ever-shrinking mobile or internet of things (IoT) based devices.

For these ovenized applications, the choice of substrate material is critical to achieve the desired performance within the size and power constraints of the system. Most commercial devices are currently fabricated on silicon, which can be formed with excellent purity, has an easily grown oxide, and has a variety of crystal planes to modify its material properties. Silicon also has many decades of industrial and academic research and development into fabrication methods and techniques, creating many useful techniques for three-dimensional MEMS processing. However, silicon has a relatively large thermal conductivity, is optically opaque in critical wavelengths for optical applications, has a significant thermal expansion coefficient, and is relatively expensive despite large economies of scale. A material that can provide a higher quality resonator, especially for environmentally-stable ovenized systems, is fused silica. Fused silica is extremely pure amorphous silicon dioxide with extremely high transmittance in the sub-2000 nm wavelength

range [5], exceptionally low thermal expansion and conductivity, and can be made substantially cheaper than silicon due to its amorphous state. These physical properties allow for more efficient device ovenization, as less power is needed to maintain a temperature set point. The physical properties of fused silica, combined with an exceptionally low material loss [6, 7], make it an intriguing material for high-performance, environmentally-stable ovenized systems and for integration with optical systems or sensors.

Table 1.1
Some Applications for Miniaturized Timing References. Adapted from [8].

Military-Aerospace	**Industrial**	**Consumer**	**Automotive**
Communication	Communications	Watches & Clocks	Engine Control
Navigation	Telecommunications	Toys and Games	Radio
Radar	Mobile/Cellular	Home Computers	Clock
IFF	Aviation	Mobile/Cellular	Navigation
Surveillance	Marine	Radio	Sensors
Guidance Systems	Navigation	Wearable Electronics	Safety
Satellites	Instrumentation	Security Systems	
	Digital Systems	Navigation	
	Computers		

Applications for Miniaturized Timing References

As mentioned, miniaturized timing references are used almost universally in modern electronics, with a partial list of applications shown in Table 1.1 [9]. As the demand for smaller and more robust versions of these applications rises, the demand for performance also increases, especially in the realms of communication and inertial navigation. As an example, a one millisecond timing error introduced into a GPS would correspond to almost 300 kilometers of distance error, a clearly unacceptable result for the meter-range accuracy on civilian GPS [9]. Coupling this accuracy with the extremely low signal power that needs to be received, equivalent

to the brightness of a flashlight in Los Angeles as seen from New York City, and it can be seen how critical it is to have an incredibly stable and precise timing reference [9]. Similar demands are found in military and civilian radar, as well as in inertial navigation through dead reckoning.

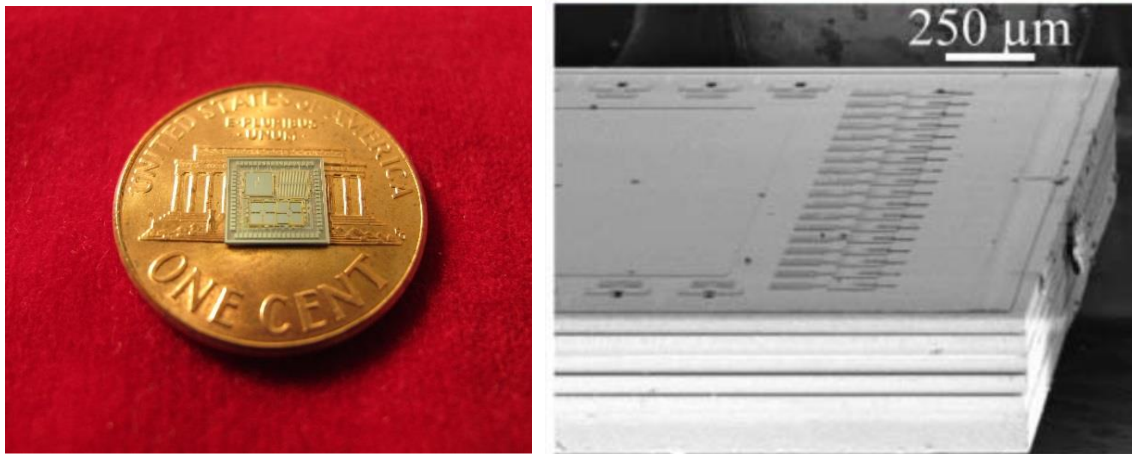

Fig. 1.1: (Left) Photograph of a fabricated inertial navigation platform on a U.S. Penny. (Right) A SEM view of the stacked platform showing multiple layers containing the inertial sensors. Images adapted from [10].

One application area that is seeing a surge of interest in miniaturization is in the realm of inertial navigation. Currently available technology for inertial navigation using dead reckoning involves the use of large, power hungry systems [11, 12] and there is a growing interest in shrinking these devices while maintaining extremely high performance. One prototype, shown in Fig. 1.1, involves a multi-layer stack of devices containing the requisite accelerometers, gyroscopes, and a singular timing reference to provide accurate navigational data in a volume less than 10 mm^3 [10]. The timing reference in this system needs to be extremely accurate to properly clock the inertial navigation units inside, along with an extreme resistance to shock, acceleration, and radiation. Another potential application for environmentally robust miniaturized timing references is in space-based picosatellite applications [13]. Picosatellites, typically defined as spacecraft smaller than $5\times5\times10$ in^3 and/or <1 kg, are designed for short-lived in-orbit science or communication. These smaller satellites can be launched on larger spacecraft platforms for a fraction of the cost and with specialized sensors for science or communication purposes. However,

the shrinking size of these devices requires high performance at a fraction of the size of current satellites, pushing the need for highly robust miniaturized timing references.

Current State-of-the-Art Timing References

There are two general types of timing references currently available on the commercial market, quartz crystal oscillators and atomic oscillators. Quartz oscillators are made from single-crystal silicon dioxide (SiO_2), cut at different angles depending on the application and utilizing quartz's natural piezoelectricity to mechanically actuate and read out electrical signals. They typically operate between low kHz to low GHz frequency ranges, with the majority in the low- to mid-MHz frequency range. For commercially available quartz oscillators, there are various levels of cost and accuracy, ranging from uncompensated crystal oscillators to oven controlled and temperature compensated oven controlled oscillators. These typically vary in cost from just tens of cents to hundreds or thousands of dollars, depending on the amount of compensation and accuracy required [9]. Atomic oscillators tend to have larger volumes, consuming much more power and costing substantially more in exchange for exceptional stability and accuracy. Atomic oscillators work at much higher frequencies than quartz, between one and ten GHz, and function though the utilization of stable energy gaps between atomic states. These devices typical show orders of magnitude more stability than quartz oscillators, but typically cost in the tens of thousands of dollars and consume an order of magnitude more power [9]. A comparison between quartz and atomic oscillators, including preliminary results of the MEMS timing references discussed in this work, are shown in Table 1.2. For environmentally challenging applications in space and inertial navigation, stability at least on the order of ovenized quartz is required and therefore is the performance target for MEMS resonators throughout this work. From Table 1.2, it can be seen that MEMS resonators can be made cheaper and smaller than the currently available

alternatives, although additional work is needed on improving device performance. This work is focused on investigating and addressing loss mechanisms and sources of instability in order to match the performance of ovenized quartz, all at a fraction of the size, power, and price.

Table 1.2
Comparison Between State-of-the-Art Commercial Timing References. Adapted from [9].

	MEMS (This Work)	*Quartz*	*Ovenized Quartz*	*Atomic Rubidium*	*Atomic Cesium*
Accuracy (seconds per year)	N/A	2×10^{-6}	1×10^{-8}	5×10^{-10}	2×10^{-11}
Temperature Stability (-40-85°C)	1×10^{-6}	2×10^{-6}	2×10^{-6}	3×10^{-10}	2×10^{-11}
Size (cm^{-3})	0.001 (Unpackaged)	10	20-200	200-800	6,000
Power (W)	0.001	0.04	0.6	20	30
Price ($)	<$10	$10-100	$200-2000	$2,000-8,000	$50,000

Fused Silica as a Resonant Material

While silicon MEMS are an established technology that can provide excellent performance [14, 15], alternate materials for specific applications have not been heavily explored. Fused silica is a promising material that shows low internal losses [16], a low coefficient of thermal expansion, and low thermal conductivity [5]. It is created by flame-purifying amorphous silicon dioxide, creating an ultra-pure material with minimal defects. These factors make it an appealing material not only for low-loss resonant devices, but also for low-power ovenization and robust, stable packaging.

Fused silica has a history of use as a resonant material in a number of non-MEMS applications. For example, fused silica was investigated in the 1970's for its very low internal losses, demonstrating quality factors (Qs) of well over one million [6, 16]. From this, fused silica rods were used as anchors for gravitational wave detectors, as their ultra-low loss maximizes the sensitivity of the detector [17]. Fused silica has also been used for millimeter-sized gyroscopes for

space-based inertial navigation. These gyroscopes, known as hemispherical resonator gyroscopes (HRGs), utilize wineglass modes with Qs in the millions and proven reliability over multiple decades of demanding space-based applications [18]. This concept has been recently extended to a batch-fabricated three-dimensional glass blown resonator, also showing Qs in the millions at a fraction of the size of HRGs [19, 20]. These long-term space-based gyroscope applications demonstrate the extremely high reliability and performance of fused silica as a resonant material. On the MEMS resonator front, there has also been recent work demonstrating micro-machined capacitive cantilevers on fused silica [21], but these devices suffered from large actuation gaps and had insertion losses of over 100 dB, making them unlikely candidates for integration in accurate timing references.

Besides being used in device applications, fused silica as a packaging material has also been investigated. A recent publication demonstrating a multi-stack fused silica package with multiple inertial and timing devices has shown fused silica as a potential device packaging material [10]. The package is made of multiple thinned fused silica layers bonded together, with each layer containing various inertial devices. These fused silica packages have excellent mechanical and thermal characteristics that can provide a more robust package than what is offered by silicon-based packaging.

Quality Factor and Loss Mechanisms

There are a number of mechanisms in mechanical resonators that cause loss. In general, loss is measured using a quantity known as Q, which is defined as:

$$Quality\ Factor\ (Q) = 2\pi \frac{Total\ Energy\ in\ System}{Energy\ Lost\ per\ Cycle} \qquad \text{(Equation 1.1)}$$

The most common way to measure this metric in mechanical resonators is through the measured S-parameters of the resonator, as shown in Fig 1.2. The Q is found by taking the width of the resonance peak at 3dB below the peak amplitude, or:

$$Quality\ Factor\ (Q) = \frac{Center\ Frequency}{-3dB\ Bandwidth} = \frac{f_0}{\Delta f} \quad \text{(Equation 1.2)}$$

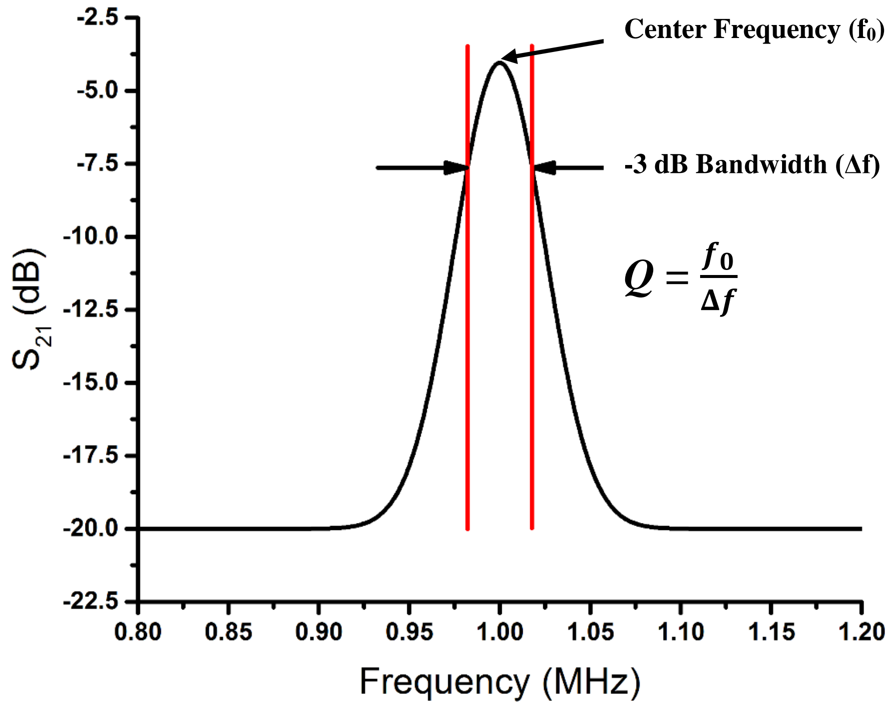

Fig. 1.2: Example resonator response demonstrating a common method of calculating Q from measured results.

The final Q of a resonator is typically a combination of many different loss mechanisms. The most common loss mechanisms in MEMS resonators include anchor or support loss [22], thermoelastic damping (TED) [23], viscous damping [24], surface losses [25], interface losses [26], and phonon-phonon losses [27, 28]. All these losses can be expressed as a single, combined Q through the following equation:

$$\frac{1}{Total\ Q} = \frac{1}{Q_{anchor}} + \frac{1}{Q_{TED}} + \frac{1}{Q_{damping}} + \frac{1}{Q_{surface}} + \frac{1}{Q_{interface}} + \frac{1}{Q_{phonon}} \quad \text{(Equation 1.3)}$$

As Eq. 1.3 outlines, the lowest Q will typically dominate the overall Q, and by eliminating or mitigating the dominant loss mechanism the overall Q of the device can be improved.

The dominant loss mechanism depends on the designed frequency, geometry, and operating environment of the timing reference. Typically, resonators in the hundreds of MHz to low GHz regime are dominated by phonon-phonon loss, known as Akheiser loss, which is caused by localized phonon perturbation from acoustic waves and the subsequent redistribution across the created gradient [27]. This loss enforces a constant product of frequency and Q, known as a $f \times Q$ product. The exact $f \times Q$ product varies by material, but typically is in the range of 10^{13} to 10^{16} [7]. At a high enough frequency, for example at around 2 GHz in silicon, this model breaks down and a new quantum regime, first introduced by Landau and Rumer, is applied [29]. This regime is no longer limited by a set $f \times Q$ product and the limit increases logarithmically with frequency.

At lower frequencies, TED becomes a significant concern for mechanical resonators. This loss is caused by the creation of thermal gradients in a resonator that lag behind the strain field created during harmonic oscillation. These gradients are then resolved at a net loss of energy, and typically is highly sensitive to material parameters and resonance frequency [23]. This loss is typically maximum in the hundreds of kHz to tens of MHz, where the thermal gradients begin to lag behind the typical harmonic cycle period. At low frequencies, the thermal gradients have time to match the relatively slow strain cycles and little loss is seen. At higher frequencies, typically above 100 MHz, thermal gradients cannot begin to resolve before the next strain cycle and losses again diminish [23]. This effectively creates a maxima of loss in the low MHz range, where is typically in the frequency range where many timing references operate. This loss can be mitigated through a combination of design decisions, mode selection, and material choices, but cannot be entirely eliminated.

A loss mechanism that affects resonators at any frequency is known as anchor, clamping, or support loss. This loss mechanism is due to acoustic energy being lost through resonator connections to the substrate, which are required for mechanical stability and signal routing [22]. To minimize this, most devices are designed to have the narrowest anchors possible, which can lead to robustness and power handling problems. Anchor loss can be partially mitigated through proper design, for example through the use of nodal points [30, 31], acoustic reflectors [32], soft tethers [33], or acoustic engineering [34, 35], and can be accurately simulated using finite element modeling (FEM) software in the design phase [22, 36, 37]. This source of loss is fairly well understood and has a good number of mitigation strategies, and therefore is less of a dominant loss mechanism in modern timing references.

There are a number of loss mechanisms in addition to the methods listed above, such as viscous damping, surface losses, and interface losses. Viscous damping is typically an issue for low frequency resonators in pressurized or ambient conditions, and is caused by the resistance of air or liquid to movement during resonance [24]. This is typically avoided through the operation of resonators in vacuum, hermitically sealed environments, or through resonator operation in the mid- to high-frequency regime. Surface losses are directly related to the surface roughness of a resonator, which causes wave scattering and phase incoherency in a standing wave mode in a device volume. This can be addressed through fabrication optimizations, and a number of smoothing processes during fabrication exist to mitigate this loss [25]. Interface losses are a less well-understood loss mechanism that relates to interfaces between different materials on a resonator. There are a number of theories regarding the specific loss mechanism, such as an instantaneous strain boundary at material interfaces causing heat generation [26], but there is yet to be a general consensus of the precise mechanism.

The overall device *Q* is a critical factor for timing references due to its direct correlation to frequency stability of a timing reference. A timing reference with poor stability will exhibit notable frequency shifts around its center frequency, which is unacceptable for high bit rate clocking, signal detection or demodulation, or any number of other modern data processing or communication applications. Frequency stability is often expressed through a metric known as phase noise, which can be qualitatively predicted by Leeson's model, which is written as [38]:

$$L(\Delta f) = 10log\left\{\frac{k_bTF}{P_{sig}}\left[\frac{1}{4Q_L^2}\left(\frac{f_0}{\Delta f}\right)^2 + 1\right]\right\} \quad \text{(Equation 1.4)}$$

where k_b is Boltzman's constant, T is temperature, F is the noise figure, P_{sig} is the input power of the signal, Q_L is the loaded quality factor of the resonator, f_0 is the center frequency, and Δf is the frequency offset from f_0. It can be noted from this equation that *Q* is inversely proportional to the phase noise, and is especially significant at frequencies close to the center frequency. A high *Q* (>10,000) minimizes this close-to-carrier instability and can provide an excellent timing reference for a number of critical applications. In order to achieve this, an understanding of each loss mechanism is important in order to properly address them and improve the overall performance.

Resonator Actuation Methods

There are multiple actuation methods for MEMS resonators, with the most popular including capacitive, piezoelectric, magnetic and thermal actuation. Capacitive actuation is one of the most common methods used in MEMS devices, and typically results in minimal *Q* loading at the cost of high insertion loss and low power handling [39]. This approach is difficult to implement in the case of fused silica, as a conductive surface is required for charge to build up to create capacitive force. It can be done, as in [21], by coating the material sidewalls with a conductive material, but this creates additional interfaces that can reduce performance. Other than capacitive

actuation, magnetic actuation requires specific ferromagnetic materials for actuation, which creates a similar issue to capacitive actuation in non-magnetic fused silica [40, 41]. Thermal actuation works via displacement created through thermal expansion, but requires large amounts of power and larger thermal conductivity, limiting viable implementations in fused silica [42].

The most practical actuation method for fused silica is piezoelectric actuation. This method takes advantage of the piezoelectric effect, which converts electrical signals into mechanical force and vice versa. Piezoelectric actuation is the main method for quartz crystals, and has additionally seen use in a variety of MEMS devices from filters and timing references [43-45], to various sensors and actuators [46, 47]. The piezoelectric effect is typically seen in Wurzite crystals, where a mechanical strain creates a crystal lattice displacement that generates a net electric field. This net dipole in the crystal structure forms an overall material polarization, effectively converting mechanical energy to electric energy, or from electric to mechanical energy if the process is reversed. This process is governed by the following equations [48]:

$$T_{ij} = c_{ijkl}S_{kl} - e_{kij}E_k \qquad \text{(Equation 1.5)}$$

$$D_k = e_{kij}S_{ij} + \epsilon_{ki}E_i \qquad \text{(Equation 1.6)}$$

where T_{ij} is the mechanical stress tensor, c_{ijkl} are the coefficients of elasticity, S_{kl} is the strain tensor, e_{kij} is the piezoelectric stress tensor, E_k is the electric field tensor, D_k is the electric displacement vector, and ϵ_{ki} is the dielectric constant tensor.

Piezoelectric films have been used to make a number of MEMS resonators, with popular materials including aluminum nitride (AlN) [49], zinc oxide (ZnO) [50], lead zirconate titanate ceramic (PZT) [51], and gallium nitride (GaN) [52]. One of the most flexible piezoelectric films is AlN, due to its CMOS compatibility and low temperature sputtering. Due to material

compatibility, high quality deposition, and ease of fabrication the fused silica devices of this work are actuated with AlN, but other piezoelectric materials are further investigated in Chapter 3.

As noted, piezoelectric actuation was chosen as the actuation method for these fused silica resonators to actuate non-conductive fused silica. Choosing piezoelectric actuation avoids the need to create conductive surfaces for capacitive actuation, but also provides benefits in lower insertion loss and higher power handling in a tradeoff for additional interfaces. To better understand this choice, it is useful to examine the tradeoffs inherent for capacitive actuation. One of the most critical issue with capacitive actuation lies in the gap sizes necessary to achieve low insertion loss. The equation for motional resistance, which is directly related to insertion loss and relates to increased output current for a given voltage, can be expressed as:

$$R_m = \frac{K g_d^4}{Q \epsilon_0 A_d^2 V_p^2 \omega_m} \quad \text{(Equation 1.7)}$$

where K is the mechanical stiffness of the resonator, g_d is the gap between electrode and resonator, Q is the device quality factor, ϵ_0 is the dielectric constant, A is the cross-sectional surface area of the electrode/resonator region, V_P is the applied DC bias voltage, and ω_m is the operating frequency of the resonator in radians.

Immediately it can be noted that the gap distance is related to the motional resistance by a power of four, emphasizing the extreme sensitivity of the motional resistance to gap size. For fused silica, where high-aspect ratio structures are difficult to achieve, it quickly becomes difficult to achieve the low motional impedance that piezoelectric actuation offers. As an example, for the fused silica devices presented in Chapter 2 the minimum feature size set by the fused silica DRIE leads to a 20 μm minimum gap size. Typical capacitive gap sizes in literature to reach lower insertion losses are in the sub-micrometer range, which means at minimum a hundred times

increase in bias voltage, 10,000 times Q increase, or a combination of the two to maintain a similar insertion loss between a 2 μm and 20 μm gap size. This requirement only increases as the gap decreases into to sub-micrometer ranges, which is a necessity to meet a comparable motional impedance of piezoelectric actuation (~400 Ω for the devices in this work). A bias voltage this large is difficult to achieve in robust, miniaturized devices and would require extra space, circuitry, and complexity. A smaller gap size also leads to earlier capacitive pull in, reducing power handling of the final timing reference. To avoid the additional complexity and power limitations while also attempting to avoid the complexity of fabrication for patterned conductive sidewalls and small gaps, piezoelectric actuation was selected for these devices.

Temperature Compensation of Resonators

With all materials, changes in temperature cause a shift in physical material properties. This in turn causes a drift in resonant frequency of the resonator as its properties shift, which needs to be corrected in order to maintain frequency stability. This sensitivity typically stems from two major changes in material parameters, Young's modulus and coefficient of thermal expansion (CTE). These two factors combine to affect the temperature coefficient of frequency (TCF), or the sensitivity of the resonance frequency to temperature, with a first order linear estimate of:

$$TCF = \frac{1}{2}(TCE + 2 \cdot CTE) \quad \text{(Equation 1.8)}$$

For most materials used in MEMS, the temperature coefficient of elasticity (TCE) is much larger than the CTE and is typically has the dominant effect on TCF. For example, silicon's TCE for nominal doping is typically around -64 ppm/K [53] as compared to its CTE of 2.6 ppm/K. There are also second- and third-order sensitivities to these materials, which come into effect for fine tuning temperature sensitivities [53, 54].

There are a number of methods used to compensate this unwanted frequency drift in resonators, both passive and active. Passive compensation can involve the use of additional materials with opposite TCEs in conjunction with the original resonant material to effectively cancel out drift [55, 56]. Alternatively, geometric compensation can be used to compensate for specific mode shapes [57] while material doping concentration, specifically in silicon, has been shown to significantly modify the temperature sensitivity of the material's elastic parameters [58, 59]. Active compensation uses power-consuming methods to address temperature drift, such as through electrostatic tuning for material softening [60], electronic calibration and correction [61], or material ovenization that minimizes any temperature perturbations from the environment [62, 63]. If ultra-stable timing references are required, it is possible to combine multiple forms of passive or active compensation in order to minimize temperature-based drift.

Dual-Mode Resonators

An example of a method that combines both active and passive methods to address temperature instability is dual-mode resonator operation. This technique, first used in quartz crystals, utilizes two simultaneously actuated modes on the same device volume. By designing each mode to demonstrate a different temperature response, a beat frequency can be generated that effectively tracks any change in temperature. Any perturbation in the beat frequency can then be compensated through electronic or ovenized methods. This method has been used to compensate for temperature changes, reducing drift to just tens of ppb over a wide temperature range [64, 65]. Recently, a similar approach was adapted to MEMS piezoelectric and electrostatic resonators, showing 226 ppm of drift over a 120 ℃ temperature range for an otherwise uncompensated AlN-on-silicon resonator [66] and a 500 ppb drift over a 120 ℃ temperature range for an electrostatically actuated hermetically sealed ovenized resonator [67]. If this dual-mode method

can be extended to create a low-power timing reference with similar stability, it becomes possible to compete with ovenized quartz resonators with just a fraction of the size, power, and cost of commercially available alternatives.

Research Objectives and Contribution

The main objective of this work is to investigate the use of piezoelectrically actuated fused-silica resonators as timing references. Fused silica as a material shows the potential for extremely large Qs and robust packaging, but has not been extensively explored as a micromachinable material for use in resonators. To explore this space, a prototype AlN-on-silica resonator was designed and fabricated, successfully demonstrating the first piezoelectrically actuated fused silica resonator reported in literature [68]. In order to improve device performance, especially in regards to Q, loss mechanisms in fused silica are investigated in-depth. A number of loss mechanisms, including anchor loss, TED, and surface losses, are investigated using analytical models, simulation, and experimental results in order to determine and mitigate the dominant loss factor. From this, a novel loss mechanism is introduced and investigated as a potential loss mechanism in piezoelectric resonators [69].

In tandem with the efforts to maximize device Q, an investigation into the temperature stability of fused silica as a resonator material is presented. Both active and passive compensation methods are developed for AlN-on-silica platforms in order to improve the device stability. An ovenized platform with feedback system is developed and presented to implement active compensation [70] and nickel-refilled trenches are embedded into the resonator body to achieve efficient passive temperature compensation [71]. From the analysis of these results, dual-mode fused silica resonators are proposed to combine the strengths of both methods for further stability improvements

A dual-mode resonator system is developed on a prototype AlN-on-silicon platform to demonstrate acoustic engineering for mode shape confinement and designable temperature sensitivity. A design methodology is outlined and fabricated resonators presented with measured results for performance and temperature stability. This prototype device forms the core of a temperature compensation system with little to no temperature error and exceptional stability.

In summary, this work contributes:

- The first reported piezoelectric-on-silica resonator reported in literature, showing a Q of 19,671 at 4.96 MHz with an insertion loss of 16.9 dB.
- An in-depth investigation of loss mechanisms on the piezoelectric-on-silica platform, demonstrating that anchor losses, TED, and surface losses are not the dominant loss mechanisms for AlN-on-silica resonators.
- A new proposed method of loss in piezoelectric resonators known as charge redistribution loss, which is caused by the resolution of charge gradients across piezoelectric films. This loss is simulated, suggesting that it may be the dominant mechanism in AlN-on-silica resonators.
- Demonstrating both active and passive loss mechanisms for fused silica devices, including a method of passive compensation for fused silica using nickel-refilled trenches that reduces temperature sensitivity from 90 ppm/K to 50 ppm/K.
- The design and fabrication of a dual-mode resonator prototype on an AlN-on-silicon platform that demonstrates a 14 ppm/K TCF gap between modes on the same device volume.

Organization

This thesis is organized into six separate chapters, each with a specific focus. Chapter one is focused on the motivation and introduction into the basics of MEMS resonators, and a general overview of the current state-of-the-art in timing references.

Chapter two focuses on the design, fabrication, and characterization of the fused silica AlN-on-silica resonator. Specifically, the mode shape and rationalization thereof is discussed, as well as simulation results that support a specific mode shape. The fabrication process for AlN-on-silica resonators is also outlined, with measured results presented and discussed. Multiple modes present on the proposed discussion are discussed, and specific temperature and power handling data is presented.

Chapter three introduces major loss mechanisms present in the AlN-on-silica resonators, and offers potential mitigation methods to avoid performance bottlenecks. TED is analytically modeled and experimentally tested and surface loss is experimentally investigated. Interfaces losses are then discussed, and a new loss mechanism is introduced and verified using analytical modeling and experimental testing.

Chapter four introduces temperature stability and discusses its sources and potential mitigation methods. Ovenized fused silica resonators are introduced and fabricated devices are demonstrated, showing an increase in overall temperature stability by a factor of 1000. Passive temperature compensation of fused silica is also introduced, with a prototype resonator demonstrated using nickel for material compensation. From the analysis of these results, a dual-mode resonator is suggested that provides increased temperature stability over the presented results.

Chapter five gives an overview of dual-mode resonator operation, and introduces phonon trapping as a method for dual-mode resonator design. A design methodology is introduced, and prototype dual-mode resonators are fabricated and characterized. The temperature sensitivity of these devices is characterized and discussed, successfully demonstrating dual mode operation with a large TCF differential.

Chapter six presents suggested paths for future work, including additional work on charge redistribution and interface loss for piezoelectric-on-silica resonators, a design for a dual-mode oscillator, and architectures for dual-mode ovenized oscillators to provide the maximum possible stability for MEMS resonators.

References

[1] M. E. Frerking, "Fifty years of progress in quartz crystal frequency standards," in *Proceedings of the 50th IEEE International Frequency Control Symposium, 1996,* Honolulu, HI, USA, 1996, pp. 33-46.

[2] H. Rapp and K. Hjort, "Cut-independent quartz resonator micromachining by ion track lithography," in *Proceedings of the the IEEE International Frequency Control Symposium, Frequency and Time Forum,* Besancon, France, 1999, pp. 485-488.

[3] (July 6, 2016). *SiTime, Silicon MEMS Oscillators and Clock Generators*. Available: http://www.sitime.com.

[4] R. Nugent, R. Munakata, A. Chin, R. Coelho and J. Puig-Suari, "The cubesat: the picosatellite standard for research and education," *Aerospace Engineering,* vol. 805, pp. 756-5087, Sept., 2008.

[5] Corning, "HPFS Product Brochure All Grades," *Corning HPFS 7979, 7980, 8655 Fused Silica Datasheet,* July, 2015.

[6] V. B. Braginsky, V. P. Mitrofanov and V. I. Panov, *Systems with Small Dissipation.* Chicago, IL: The University of Chicago Press, 1985.

[7] R. Tabrizian, M. Rais-Zadeh and F. Ayazi, "Effect of phonon interactions on limiting the f.Q product of micromechanical resonators," in *Proceedings of the International Solid-State Sensors, Actuators and Microsystems Conference;* Anchorage, AK, USA, 2009, pp. 2131-2134.

[8] National Materials Advisory Board and National Research Council, *Quartz for the National Defense Stockpile: Report of the Committee on Cultured Quartz for the National Defense Stockpile.* National Academy Press, 1985.

[9] J. R. Vig, "Quartz crystal resonators and oscillators," *US Army Communications-Electronics Command,* Jan., 2001.

[10] Z. Cao, Y. Yuan, G. He, R. L. Peterson and K. Najafi, "Fabrication of multi-layer vertically stacked fused silica microsystems," in *Proceeds of the 17th International Conference on Solid-State Sensors, Actuators and Microsystems (TRANSDUCERS & EUROSENSORS),* 2013, pp. 810-813.

[11] S. Kennedy and J. Rossi, "Performance of a deeply coupled commercial grade GPS/INS system from KVH and NovAtel inc." in *Proceedings of the IEEE/ION Position, Location and Navigation Symposium,* Monterey, CA, USA, 2008, pp. 17-24.

[12] A. Kersey, A. Dandridge and W. Burns, "Fiber optic gyroscope technology," *Optic News,* vol. 15, pp. 12-19, 1989.

[13] M. Rais-Zadeh, V. A. Thakar, Z. Wu and A. Peczalski, "Temperature compensated silicon resonators for space applications," in *Proceedings of the SPIE 8614 Reliability, Packaging, Testing, and Characterization of MOEMS/MEMS and Nanodevices XII,* San Francisco, California, USA, 2013, pp. 86140E-1.

[14] H. Lee, A. Partridge and F. Assaderaghi, "Low jitter and temperature stable MEMS oscillators," in *Proceedings of the IEEE International Frequency Control Symposium Proceedings (IFCS),* 2012, pp. 1-5.

[15] H. Bhugra, Y. Wang, W. Pan, D. Lei and S. Lee, "High performance pMEMS™ oscillators - the next generation frequency references," in *Proceedings of the International Electron Devices Meeting (IEDM),* Washington, DC, USA, 2011, pp. 20.1.1-20.1.4.

[16] S. D. Penn, G. M. Harry, A. M. Gretarsson, S. E. Kittelberger, P. R. Saulson, J. J. Schiller, J. R. Smith and S. O. Swords, "High quality factor measured in fused silica," *Rev. Sci. Instrum.,* vol. 72, pp. 3670, 2001.

[17] S. D. Penn, P. H. Sneddon, H. Armandula, J. C. Betzwieser, G. Cagnoli, J. Camp, D. R. M. Crooks, M. M. Fejer, A. M. Gretarsson, G. M. Harry, J. Hough, S. E. Kittelberger, M. J. Mortonson, R. Route, S. Rowan and C. C. Vassilious, "Mechanical loss in tantala/silica dielectric mirror coatings," *Classical and Quantum Gravity,* vol. 20, pp. 2917, June, 2003.

[18] D. M. Rozelle, "The hemispherical resonator gyro: From wineglass to the planets," in *Proc. 19th AAS/AIAA Space Flight Mech. Meeting,* Savannah, GA, USA, 2009, pp. 1157-1178.

[19] J. Y. Cho, J. Woo, J. Yan, R. L. Peterson and K. Najafi, "Fused-silica micro birdbath resonator gyroscope (μ-BRG)," *J. Microelectromech Syst.,* vol. 23, pp. 66-77, Feb., 2014.

[20] T. Nagourney, J. Cho, A. Darvishian, B. Shiari and K. Najafi, "130 second ring-down time and 3.98 million quality factor in 10 kHz fused silica micro birdbath shell resonator," in *Proceedings of Solid-State Sensors, Actuators and Microsystems Workshop,* Hilton Head Island, SC, USA, 2016, pp. 408-411.

[21] Y. Hwang, H. Jung, E. Song, I. Hyeon, Y. Kim and C. Baek, "Fabrication of electrostatically-actuated, in-plane fused quartz resonators using silicon-on-quartz (SOQ) bonding and quartz drie," in *Proceedings of the 22nd IEEE International Conference on Micro Electro Mechanical Systems (MEMS),* Sorrento, Italy, 2009, pp. 729-732.

[22] Zhili Hao and F. Ayazi, "Support loss in micromechanical disk resonators," in *Proceedings of the 18th IEEE International Conference on Micro Electro Mechanical Systems, (MEMS),* Miami Beach, FL, USA, 2005, pp. 137-141.

[23] C. Zener, "Internal friction in solids. I: theory of internal friction in reeds," *Physical Review,* vol. 52, pp. 230-235, 1937.

[24] M. Bao and H. Yang, "Squeeze film air damping in MEMS," *Sensors and Actuators A: Physical,* vol. 136, pp. 3-27, 2007.

[25] B. Shiari and K. Najafi, "Surface effect influence on the quality factor of microresonators," in *Proceedings of the 17th International Conference on Solid-State Sensors, Actuators and Microsystems (TRANSDUCERS & EUROSENSORS),* 2013, pp. 1715-1718.

[26] A. Frangi, M. Cremonesi, A. Jaakkola and T. Pensala, "Analysis of anchor and interface losses in piezoelectric MEMS resonators," *Sensors and Actuators A: Physical,* vol. 190, pp. 127-135, Feb., 2013.

[27] A. Akheiser, *J. Phys. (USSR),* vol. 1, pp. 1277, 1939.

[28] S. Ghaffari, S. A. Chandorkar, S. Wang, E. J. Ng, C. H. Ahn, V. Hong, Y. Yang and T. W. Kenny, "Quantum limit of quality factor in silicon micro and nano mechanical resonators," *Sci. Rep.,* vol. 3, pp. 3244, Nov., 2013.

[29] L. Landau and G. Rumer, *Phys. Z. Sowjetunion,* vol. 11, 1937.

[30] Y. Xie, S. S. Li, Y. W. Lin, Z. Ren and C. T. Nguyen, "1.52-GHz micromechanical extensional wine-glass mode ring resonators," *IEEE Trans. Ultrason. Ferroelectr. Freq. Control,* vol. 55, pp. 890-907, Apr., 2008.

[31] K. Wang, A. Wong and C. T. Nguyen, "VHF free-free beam high-Q micromechanical resonators," *J. Microelectromech Syst.,* vol. 9, pp. 347-360, Sept., 2000.

[32] B. Harrington and R. Abdolvand, "In-plane acoustic reflectors for reducing effective anchor loss in lateral-extensional MEMS resonators," *J. Micromech. Microengineering,* vol. 21, pp. 085021, July, 2011.

[33] J. E. Lee, J. Yan and A. A. Seshia, "Study of lateral mode SOI-MEMS resonators for reduced anchor loss," *J. Micromech. Microengineering,* vol. 21, pp. 045010, Mar., 2011.

[34] R. Tabrizian and F. Ayazi, "Thermo-acoustic engineering of silicon microresonators via evanescent waves," *Appl. Phys. Lett.,* vol. 106, pp. 263504, June, 2015.

[35] R. Tabrizian and F. Ayazi, "Acoustically-engineered multi-port AlN-on-silicon resonators for accurate temperature sensing," in *Proceedings of the IEEE International Electron Devices Meeting (IEDM),* Washington D.C., USA, 2013, pp. 18.1.1-18.1.4.

[36] D. S. Bindel and S. Govindjee, "Elastic PMLs for resonator anchor loss simulation," *Int. J. Numer. Methods Eng.,* vol. 64, pp. 789-818, Feb., 2005.

[37] V. Thakar and M. Rais-Zadeh, "Optimization of tether geometry to achieve low anchor loss in lamé-mode resonators," in *Proceedings of the Joint European Frequency and Time Forum and*

International Frequency Control Symposium (EFTF/IFC), Prague, Czech Republic, 2013, pp. 129-132.

[38] D. B. Leeson, "A simple model of feedback oscillator noise spectrum," *Proc. IEEE,* vol. 54, pp. 329-330, Dec., 1966.

[39] S. Pourkamali, A. Hashimura, R. Abdolvand, G. K. Ho, A. Erbil and F. Ayazi, "High-Q single crystal silicon HARPSS capacitive beam resonators with self-aligned sub-100-nm transduction gaps," *J. Microelectromech. Syst.,* vol. 12, pp. 487-496, Aug., 2003.

[40] T. Nan, Y. Hui, M. Rinaldi and N. X. Sun, "Self-biased 215MHz magnetoelectric NEMS resonator for ultra-sensitive DC magnetic field detection," *Scientific Reports,* vol. 3, pp. 1985, June, 2013.

[41] P. Zhao, Z. Zhao, D. Hunter, R. Suchoski, C. Gao, S. Mathews, M. Wuttig and I. Takeuchi, "Fabrication and characterization of all-thin-film magnetoelectric sensors," *Appl. Phys. Lett.,* vol. 94, pp. 243507, June, 2009.

[42] A. Rahafrooz, A. Hajjam, B. Tousifar and S. Pourkamali, "Thermal actuation, a suitable mechanism for high frequency electromechanical resonators," in *Proceedings of the IEEE 23rd International Conference on Micro Electro Mechanical Systems (MEMS),* Wanchai, Hong Kong, 2010, pp. 200-203.

[43] G. Piazza, P. J. Stephanou and A. P. Pisano, "Single-chip multiple-frequency ALN MEMS filters based on contour-mode piezoelectric resonators," *J. Microelectromech. Syst.,* vol. 16, pp. 319-328, Apr., 2007.

[44] R. Ruby, "Positioning FBAR technology in the frequency and timing domain," in *Proceedings of the Joint Conference of the IEEE International Frequency Control and the European Frequency and Time Forum (FCS),* San Fransisco, CA, USA, 2011, pp. 1-10.

[45] R. C. Ruby, P. Bradley, Y. Oshmyansky, A. Chien and J. Larson, "Thin film bulk wave acoustic resonators (FBAR) for wireless applications," in *Proceedings of the IEE Ultrasonics Symposium,* Atlanta, GA, USA, 2001, pp. 813-821.

[46] P. Muralt and J. Baborowski, "Micromachined ultrasonic transducers and acoustic sensors based on piezoelectric thin films," *Journal of Electroceramics,* vol. 12, pp. 101-108, Jan., 2004.

[47] G. Gautschi, *Piezoelectric Sensorics.* Springer-Verlag Berlin Heidelberg, 2002.

[48] J. Yang, *An Introduction to the Theory of Piezoelectricity.* Springer US, 2005.

[49] G. Piazza, R. Abdolvand, G. K. Ho and F. Ayazi, "Voltage-tunable piezoelectrically-transduced single-crystal silicon micromechanical resonators," *Sensors and Actuators A: Physical,* vol. 111, pp. 71-78, March, 2004.

[50] G. Ferblantier, F. Mailly, R. Al Asmar, A. Foucaran and F. Pascal-Delannoy, "Deposition of zinc oxide thin films for application in bulk acoustic wave resonator," *Sensors and Actuators A: Physical,* vol. 122, pp. 184-188, Aug., 2005.

[51] G. L. Smith, J. S. Pulskamp, L. M. Sanchez, D. M. Potrepka, R. M. Proie, T. G. Ivanov, R. Q. Rudy, W. D. Nothwang, S. S. Bedair, C. D. Meyer, R. G. Polcawich and D. J. Green, "PZT-based piezoelectric MEMS technology," *J. Am. Ceram. Soc.,* vol. 95, pp. 1777-1792, Apr., 2012.

[52] M. Rais-Zadeh, V. J. Gokhale, A. Ansari, M. Faucher, D. Théron, Y. Cordier and L. Buchaillot, "Gallium nitride as an electromechanical material," *J. Microelectromech. Syst.,* vol. 23, pp. 1252-1271, Dec., 2014.

[53] M. A. Hopcroft, W. D. Nix and T. W. Kenny, "What is the Young's modulus of silicon?" *J. Microelectromech. Syst.,* vol. 19, pp. 229-238, Apr., 2010.

[54] V. A. Thakar, Z. Wu, C. Figueroa and M. Rais-Zadeh, "A temperature-stable clock using multiple temperature-compensated micro-resonators," in *Proceedings of the IEEE International Frequency Control Symposium (FCS),* Taipei, Taiwan, 2014, pp. 1-4.

[55] V. A. Thakar, Z. Wu, A. Peczalski and M. Rais-Zadeh, "Piezoelectrically transduced temperature-compensated flexural-mode silicon resonators," *J. Microelectromech. Syst.,* vol. 22, pp. 815-823, May, 2013.

[56] R. Tabrizian, M. Pardo and F. Ayazi, "A 27 MHz temperature compensated MEMS oscillator with sub-ppm instability," in *Proceedings of the 25th IEEE International Conference on Micro Electro Mechanical Systems (MEMS),* Paris, France, 2012, pp. 23-26.

[57] W. Hsu and C. Nguyen, "Geometric stress compensation for enhanced thermal stability in micromechanical resonators," in *Proceedings of the IEEE Ultrasonics Symposium,* Sendai, Japan, 1998, pp. 945-948.

[58] A. K. Samarao and F. Ayazi, "Temperature compensation of silicon resonators via degenerate doping," *IEEE Trans. Electron Devices,* vol. 59, pp. 87-93, Jan., 2012.

[59] E. J. Ng, V. A. Hong, Y. Yang, C. H. Ahn, C. L. M. Everhart and T. W. Kenny, "Temperature dependence of the elastic constants of doped silicon," *Journal of Microelectromechanical Systems,* vol. 24, pp. 730-741, June, 2015.

[60] K. B. Lee and Y. Cho, "A triangular electrostatic comb array for micromechanical resonant frequency tuning," *Sensors and Actuators A: Physical,* vol. 70, pp. 112-117, 1998.

[61] M. H. Perrott, J. C. Salvia, F. S. Lee, A. Partridge, S. Mukherjee, C. Arft, J. Kim, N. Arumugam, P. Gupta, S. Tabatabaei, S. Pamarti, H. Lee and F. Assaderaghi, "A temperature-to-digital converter for a MEMS-based programmable oscillator with +/-0.5 ppm frequency stability and less than 1 ps integrated jitter," *IEEE J. Solid State Circuits,* vol. 48, pp. 276-291, Jan., 2013.

[62] C. M. Jha, M. A. Hopcroft, S. A. Chandorkar, J. C. Salvia, M. Agarwal, R. N. Candler, R. Melamud, Bongsang Kim and T. W. Kenny, "Thermal isolation of encapsulated MEMS resonators," *J Microelectromech. Syst.,* vol. 17, pp. 175-184, Feb., 2008.

[63] B. Kim, R. H. Olsson and K. E. Wojciechowski, "Ovenized and thermally tunable aluminum nitride microresonators," in *Proceedings of the IEEE International Ultrasonics Symposium,* San Diego, CA, USA, 2010, pp. 974-978.

[64] J. A. Kusters, M. C. Fischer and J. G. Leach, "Dual mode operation of temperature and stress compensated crystals," in *Proceedings of the 32nd Annual Symposium on Frequency Control,* Atlantic City, NJ, USA, 1978, pp. 389-397.

[65] J. R. Vig, "Dual-mode oscillators for clocks and sensors," in *Proceedings of the IEEE Ultrasonics Symposium,* Caesars Tahoe, NV, USA, 1999, pp. 859-868.

[66] J. L. Fu, R. Tabrizian and F. Ayazi, "Dual-mode AlN-on-silicon micromechanical resonators for temperature sensing," *IEEE Trans. Electron Devices,* vol. 61, pp. 591-597, Jan., 2014.

[67] Y. Chen, E. J. Ng, D. D. Shin, C. H. Ahn, Y. Yang, I. B. Flader, V. A. Hong and T. W. Kenny, "Ovenized dual-mode clock (ODMC) based on highly doped single crystal silicon resonators," in *Proceedings of the 29th IEEE International Conference on Micro Electro Mechanical Systems (MEMS),* Shanghai, China, 2016, pp. 91-94.

[68] Z. Wu, A. Peczalski, V. A. Thakar, Z. Cao, Y. Yuan, G. He, R. L. Peterson, K. Najafi and M. Rais-Zadeh, "Piezoelectrically transduced high-Q silica micro resonators," in *Proceedings of the 26th IEEE International Conference on Micro Electro Mechanical Systems (MEMS),* San Francisco, CA, USA, 2013, pp. 122-125.

[69] A. Peczalski, Z. Wu, R. Tabrizian and M. Rais-Zadeh, "Investigation into the quality factor of piezoelectric-on-silica micromachined resonators," *J. Microelectromech. Syst.,* vol. 24, pp. 1695-1702, Dec., 2015.

[70] Z. Wu, A. Peczalski and M. Rais-Zadeh, "Device-layer ovenization of fused silica micromechanical resonators for temperature-stable operation," in *Proceedings of the Solid-State Sensors, Actuators and Microsystems Workshop (Hilton Head),* Hilton Head Island, SC, USA, 2014, pp. 87-90.

[71] A. Peczalski and M. Rais-Zadeh, "Temperature compensated fused silica resonators using embedded nickel-refilled trenches," in *Proceedings of the 18th International Conference on Solid-State Sensors, Actuators and Microsystems (TRANSDUCERS & EUROSENSORS),* Anchorage, AK, USA, 2015, pp. 157-160.

Chapter 2: Piezoelectric Fused Silica Resonators

Recent advances in MEMS resonator technology have allowed their performance to match that of the current standard in miniaturized timing references, quartz crystal. The extremely small form factor, batch fabrication ability, and integration opportunities of MEMs have tangible benefits for the current consumer drive for wearable technology and ever-shrinking mobile devices. To date, most MEMS timing references have been fabricated from silicon [1, 2] or from thin piezoelectric films [3, 4], with a number of successfully commercialized products [1-3]. However, very little research has been done to date on microresonators fabricated from fused silica. As noted in Chapter 1, fused silica is composed of high-purity flame annealed amorphous silicon dioxide and has a variety of physical attributes that lend itself favorably towards use as a resonant material. Fused silica has very low internal losses, which has prompted its use in supports for ultra-sensitive gravitational wave detectors [5], and as high-quality macro-scale resonators with quality factors (*Q*s) over 4 million [6]. In addition to the low internal friction, fused silica has a very low thermal conductivity [7]. This greatly reduces damping caused by thermal gradients, known as thermoelastic damping (TED), and has potential for low-power ovenization. Fused silica also has one of the smallest thermal coefficients of expansion (TCE) of any known material, which makes it an excellent choice for packaging. The combined physical properties of fused silica make it a unique and promising material for use in MEMS timing references and offer potential performance benefits not found in similar microsystems.

Fused Silica Resonator Considerations

In order to have a robust and practical resonator design, it is important to pick a mode that is insensitive to fabrication non-idealities. This is essential to produce a repeatable, predictable resonator for high-stability performance. Among the various resonance modes, bulk acoustic wave (BAW) resonators are good choices to fulfill this need. These modes actuate the entire volume of the resonator, ensuring high energy density and exhibiting good power handling [8]. More specifically, in-plane BAW resonance modes which rely on laterally defined dimensions to set the center frequency are very useful. These modes allow for a range of resonant frequencies on one wafer and are relatively tolerant to thickness variations, allowing for a higher fabrication yield.

Another critical question is in regard to the actuation method. As noted in Chapter 1, the two main actuation methods for MEMS timing references are capacitive and piezoelectric. In terms of device fabrication, silicon MEMS processing is mature and well understood. There have been large amounts of work in the realm of silicon semiconductors which enables a large swath of tools and techniques to modify and process a silicon wafer. In comparison, fused silica processing is relatively unexplored, especially in the area of deep anisotropic etching. The creation of high aspect ratio trenches is essential to defining thick resonator bodies, which provide high energy density and take advantage of high-quality substrate materials. Thin gaps, and therefore high aspect ratios, are also necessary for efficient capacitive actuation, but are prohibitively difficult to achieve using current fused silica etching technology. On top of this, capacitive device actuation requires a conductive path to the sidewalls, which adds fabrication complexity for electrically isolating fused silica. Besides these difficulties in fabrication, there are issues with high power handling and low motional impedance that cannot be easily addressed using capacitive actuation [9]. As these

factors are critical for achieving higher performance oscillators, piezoelectric actuation ends up being the superior choice for fused silica applications.

There is a noticeable downside in using piezoelectric films as a resonant material, which is the difficulty in achieving lower-frequency resonance in a small, robust piezoelectric film. Thick piezoelectric films are difficult to deposit and tend towards large losses due to material quality and crystalline boundaries, and therefore are mostly used in very high frequency applications [3, 10]. As the timing references being targeted are low- to mid-frequency, a piezoelectric-only route has its own set of challenges to control stress and maximize Q.

A compromise in between these two options is to use a thin-piezoelectric-on-substrate (TPoS) approach which combines the benefits of piezoelectric actuation with a low loss substrate [11]. The piezoelectric layer is actuated on top of a thick substrate, allowing the majority of the volume to be a high quality material while still maintaining a relatively low motional impedance and the higher power handling provided by piezoelectric actuation. This method also reduces the need for ultra-high aspect ratio actuation gaps, increasing fabrication tolerances and allowing for thicker device structures. By utilizing this method with a laterally defined BAW mode, the majority of downsides for each actuation method can be fully or partially mitigated.

Fabrication of Fused Silica Resonators

As previously noted, the anisotropic etching of fused silica and other glass-like materials is a major issue towards batch-fabricated devices. Most micromachining of glass-type materials, such as Pyrex glass, fused silica, and quartz, have relied on wet etching [12], [13] or serial machining processes [14-16]. Recent reported works alternatively use glass-blowing techniques [17], [18] to fabricate devices without resorting to etching processes. However, these machining techniques can only be applied to capacitively transduced devices, have limited resolution, and

low throughput. These combined factors can make large-volume silica-based MEMS fabrication difficult and costly. Instead, a batch fabrication method was designed that utilizes a specialized deep reactive ion etch (DRIE) of fused silica [19] to fabricate MEMS devices on a wafer scale. The demonstrated silica DRIE allows machining of high-aspect-ratio mechanical structures which enables co-fabrication of MEMS while allowing for high-aspect-ratio structures in a reasonable device footprint. For actuation, a piezoelectric layer is added on top of bulk fused silica to enable strong electromechanical coupling for actuation and readout.

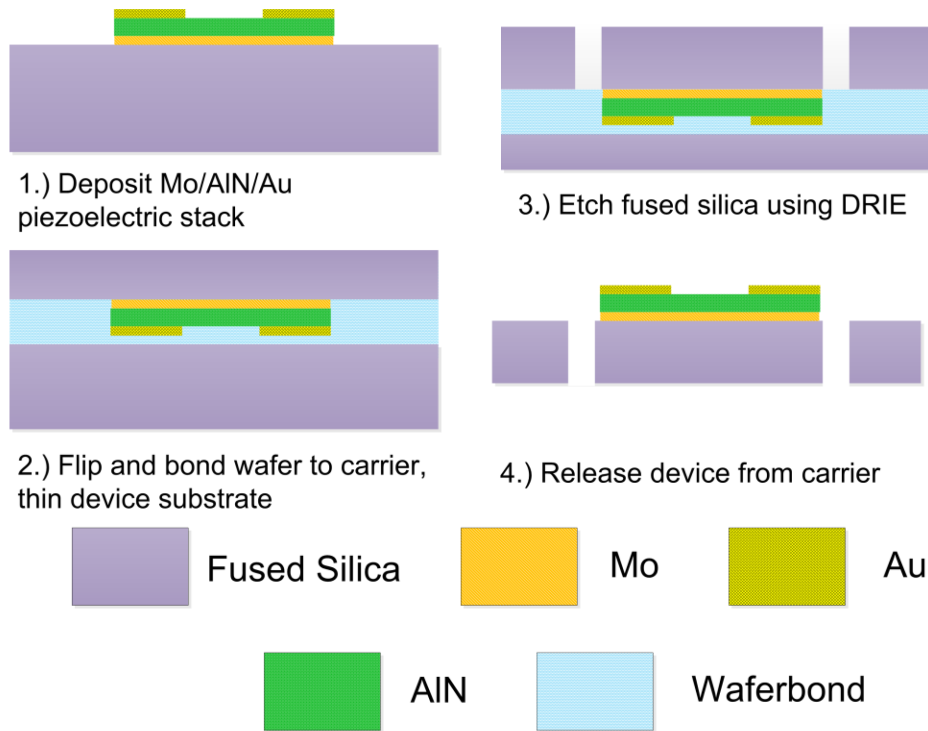

Fig. 2.1: Fabrication flow of the piezoelectric-on-silica resonators.

The fabrication process flow of the piezoelectric-on-silica resonator is outlined in Fig. 2.1. The process starts with a 525 µm thick 100 mm Corning 7980 high-purity fused silica wafer. The wafer total thickness variation (TTV) is less than 10 µm and polished surface roughness is ~5 Å. The process begins with a 1000 Å thick Molybdenum (Mo) layer sputter deposited and patterned as the bottom electrode. This bottom electrode serves as the ground plane as well as a seed layer suitable for high-quality crystalline aluminum nitride (AlN) film growth. Then, a 1 µm thick

crystalline AlN layer is sputtered as the piezoelectric material. The AlN is then patterned for bottom metal contact using a BCl-based reactive ion etch (RIE) process. The top electrode is formed by lift-off evaporation of a Chrome/Gold (Cr/Au: 100 Å/1000 Å) layer. With the piezoelectric stack defined and patterned, the wafer is thinned to the desired final device thickness. To ensure mechanical stability during processing, the fused silica wafer is flipped and polymer bonded to a carrier wafer using WaferBOND© CR-200 from Brewer Science. Wafer thinning is achieved using mechanical lapping and chemical-mechanical polishing, thinning the process wafer to 50 μm. Next, fused silica DRIE is performed on the process wafers to define the resonator contours. The process parameters and further discussion of the fused silica DRIE process can be found in [19, 20]. The devices are then detached from the carrier by dissolving the polymer bond in WaferBOND© Remover in a final release step. Finally, the dies are cleaned in xylenes, acetone, IPA, and water to remove any remaining residue. A scanning electron microscope image (SEM) of a fabricated fused silica is shown in Fig. 3.2.

With the current fused silica DRIE process, limitations in the trench aspect ratio impose notable design constraints. The achievable aspect ratio of the current fused silica DRIE process is about 3:1. This necessitates a design tradeoff between device thickness, minimum feature size, and device handling and robustness. To best address these concerns, the device layer was set at 50 μm, setting the minimum trench width at 20 μm with a 15 μm minimum feature size. A cross-section image of a fabricated fused silica resonator using this DRIE etch is seen in Fig. 2.3. It can be observed that the DRIE trenches have a slight trapezoidal shape and experience a widening near the bottom of the etched trench, which is the top of the final device, by 1 to 2 μm. Additionally, the DRIE trenches exhibit significant sidewall roughness and striations across the depth of the trench. These striations are caused by the masking photoresist used for the DRIE step and can

reach up to 1 µm in size. The consequences of the current fused silica DRIE process are notable and significantly affect device design and performance. Future improvements in this etch process and technology would enable new device designs and process enhancement, with a preliminary mitigation technique introduced in Chapter 3.

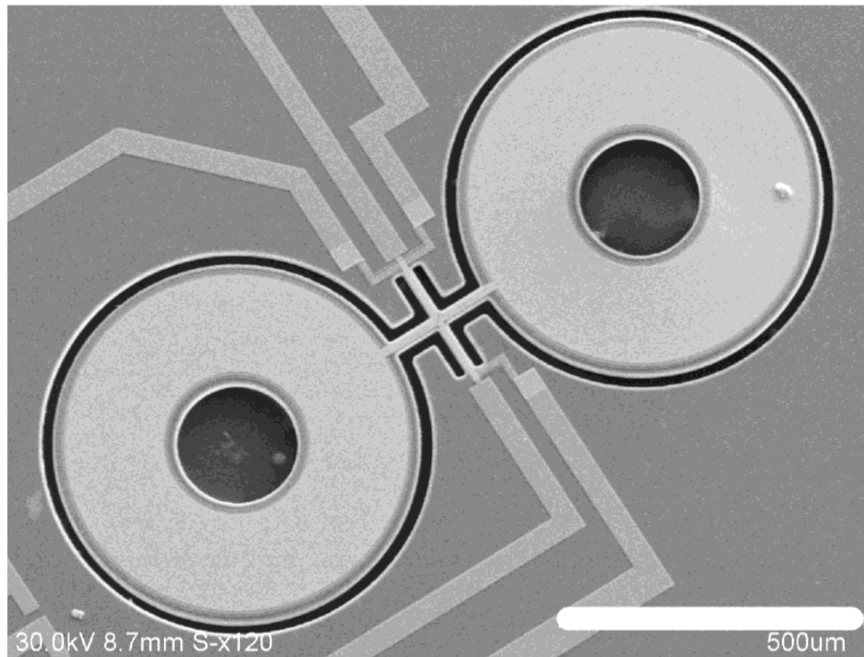

Fig. 2.2: SEM image of a fabricated AlN-on-silica dogbone resonator. The white scale bar is 500 µm in length.

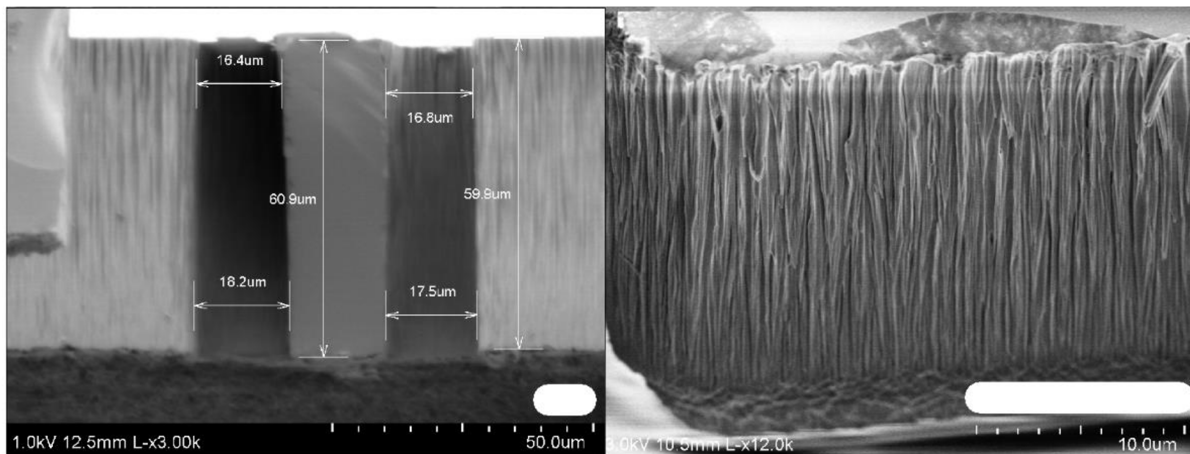

Fig. 2.3: (Left) A cross-section view of the fused silica DRIE trench profile. Note the trapezoidal shape of the center tether beam. Image adapted from [20]. (Right) A cross-section view of a DRIE trench showing the roughness introduced to the trench sidewall during the etch process. The white scale bars are 10 µm in length.

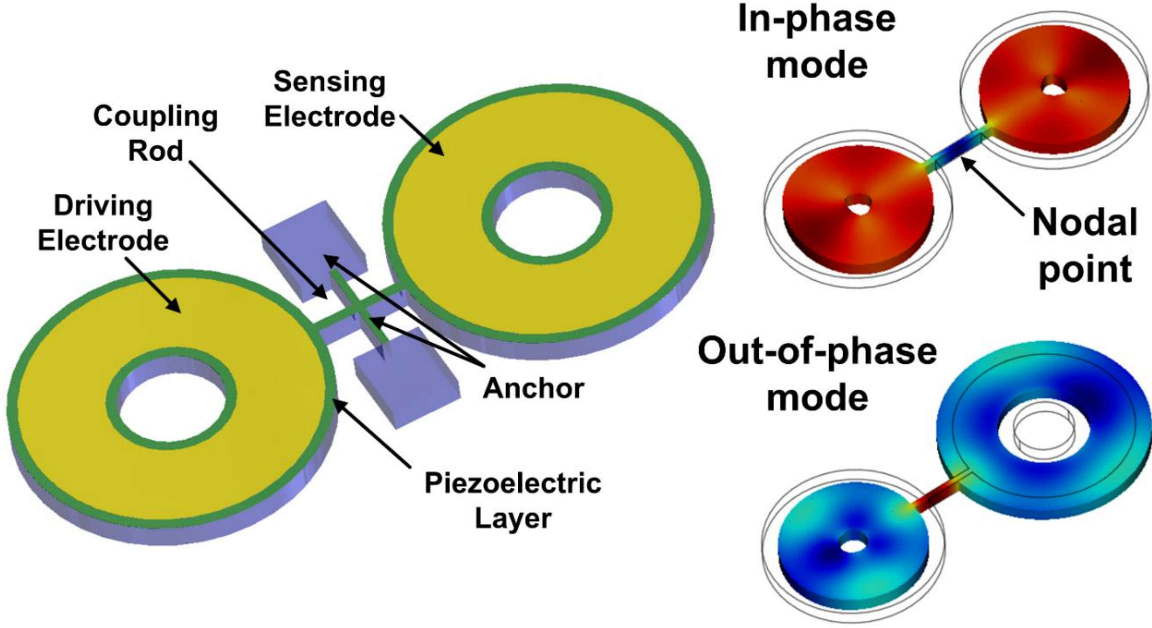

Fig. 2.4: 3-D model of the piezoelectric-on-silica MEMS resonator design and mode shapes of in-phase and out-of-plane coupled radial extensional mode.

Fused Silica Dogbone Resonator Design

With a piezoelectrically actuated piezoelectric-on-silica resonator fabrication process developed, the targeted mode shape needs to be selected. The chosen mode for this timing application is an in-plane radial extensional vibration of a pair of rings. The in-plane nature of the mode creates large strain values at the surface of the resonator body, which increases the electromechanical coupling of the thin piezoelectric film at the substrate surface. As sketched in Fig. 2.4, the resonator, coined a “dogbone” resonator, is comprised of two vibrating rings that are connected through a center coupling beam. The natural frequency of the radial extensional ring resonator can be estimated using [21]:

$$f_0 \approx \frac{1}{2\pi\sqrt{R_{out}R_{in}}}\sqrt{\frac{E_{silica}}{\rho_{silica}}}, \quad for\ R_{out} - R_{in} \ll R_{in}\ , \qquad \text{(Equation 2.1)}$$

where R_{in} and R_{out} are the inner and outer radii of the ring, respectively, E_{silica} is the Young’s modulus and ρ_{silica} is the volumetric mass density of fused silica. The material parameters used throughout this work, both for fused silica and AlN, are included Table 2.1. As R_{out}–R_{in} approaches

R_{in}, significant circumferential stresses add to the stiffness and therefore shift the resonance frequency of the radial extensional mode upwards, past the frequency outlined in Eq. 2.1 [22].

Table 2.1
COMSOL Simulation Parameters for Fused Silica Resonators

	Fused Silica	**AlN**
Young's Modulus (GPa)	72.7	309
Poisson's Ratio	0.16	0.287
Mass density (kg·m^{-3})	2201	3260
Thermal expansion coefficient (K^{-1})	0.57×10^{-6}	4.2×10^{-6}
Thermal conductivity (W·m^{-1}·K^{-1})	1.3	60
Specific heat capacity (J·kg^{-1}·K^{-1})	703	600

The coupling rod acoustically couples each ring into two configurations, an in-phase mode where each ring will expand and contact together, and an out-of-phase mode where one ring contracts while the other expands. A COMSOL simulated mode shape of these two modes is included in Fig. 2.4. The coupling rod modulates the effective modal stiffness of both the in-phase and out-of-phase modes and pushes their resonant frequency apart. The measured split for these two modes is 78 kHz, which is many times larger than the 3 dB bandwidth, 243 Hz, of the resonant peaks. Due to this large frequency split, each mode is sufficiently separated so the out-of-phase mode does not affect the in-phase mode and vice versa.

This fundamental radial extensional mode consists of a large, near-uniform displacement in the in-plane direction. This corresponds to a near-uniform strain density on the resonator surface, which is a near-ideal distribution for efficient, low motional impedance actuation of the thin piezoelectric film. The geometry of the chosen design is outlined in Fig. 2.5, along with a

cross-sectional view of the material stack used for these devices. With these dimensions, the devices resonance frequency for the radial extensional mode is found at around 5 MHz.

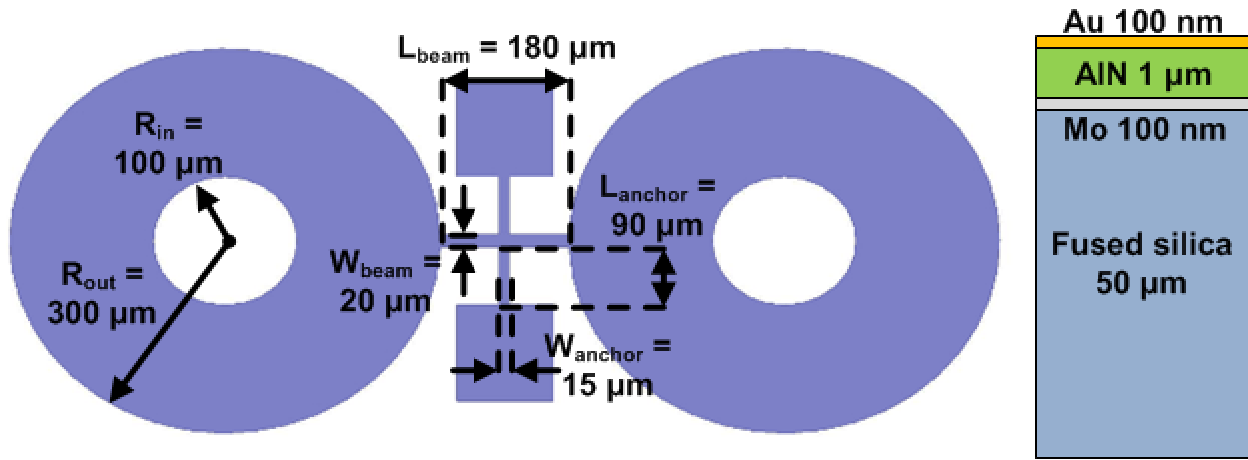

Fig. 2.5: Dimensions of the fused silica dogbone design. The piezoelectric stack dimensions are shown on the right.

Simulation and Optimization of Dogbone Devices

When designing a resonator, it is important to consider and address energy loss mechanisms to achieve a high-performance device. The most straight-forward energy loss mechanism to address is energy loss through resonator supports. This loss, known as anchor loss, stems from acoustic energy lost through device anchors. All resonators need to be supported at some point on their structure, and so some amount of loss through these points is expected. This effect can be minimized by designing supporting tethers at nodal points for the desired mode [23], [24], acoustic reflectors [25], acoustic engineering [26], or by using soft tethers [27]. These nodal points for the dogbone coupling rod are highlighted in Fig. 2.4, which defines the location of the anchor tethers for the in-phase mode. For the presented dogbone design, the fabrication limitations, specifically the fused silica DRIE minimum feature width (15μm), makes addressing anchor loss challenging. The energy lost, even while minimized by placing tethers at nodal points, is increased as the width of the tether expands. At this size, these anchors are invariably wider than the nodal point and additional acoustic energy will leak into the substrate. To adjust for this, a larger overall

resonator size is required in order to widen the nodal point size and achieve acceptable anchor losses.

For the dogbone coupled ring design, the coupling beam is attached to either end of the two rings. This point is a high velocity point for the fundamental radial extensional mode, which creates a strong acoustic coupling between the rings. From this coupling beam, two further anchoring beams are centered on the coupling beam. These anchoring beams connect the device geometry to the substrate and serve as the sole connection point to the wafer. For the in-phase mode, the center of the coupling beam contains a *pseudo*-nodal point where no displacement is found. Placing the anchor tethers at this point minimizes the energy loss into the substrate and is critical to achieving a low-loss resonator. For the out-of-phase mode, no such nodal point exists on the coupling rod. Due to this, anchor loss will be a clear limitation in achieving high-Q performance for these devices and is therefore not considered as a viable mode shape.

For the in-phase mode, the anchor loss of this structure can be simulated using COMSOL FEM software through the use of perfectly matched layers (PMLs) [28]. This approaches uses a PML to approximate a semi-infinite substrate and considers all acoustic energy lost through the anchors as unrecoverable loss, a reasonable worst-case assumption for these devices. Thanks to the nodal point present in the in-phase radial extensional mode, the simulated $Q_{a\mathrm{nchor}}$ of these devices is 1.2×10^6. The PML-based simulation method has been investigated in depth and has been shown to provide good matches to experimental results [29, 30]. Due to these two factors, we can safely anticipate that the Q_{anchor} of the fabricated resonator will be much higher than the actual performance, ensuring the device is not limited by anchor losses.

While anchor loss can be addressed through careful tether design, there are other critical energy loss mechanisms in these resonators that need to be considered. One of these loss

mechanisms is known as TED. TED is caused by heat flow along temperature gradients created during vibration of the resonator [31]. For the specific case of radial mode resonators, it was found that rings have near-uniform volumetric strain across their body, leading to a near zero gradient of strain density, and therefore temperature gradient, across both the thickness and radius of the ring. This minimized gradient is directly related to low TED for single material radial mode designs, such as the chosen dogbone structure [32]. Additional benefit is seen when fused silica is used as the substrate material, as its low thermal conductivity further minimizes the heat flow across thermal gradients. The TED, or Q_{TED}, of these modes can be modeled using COMSOL FEM simulations that calculate heat flow caused from resonant vibration [33]. As seen in Table 2.2, a radial extensional mode device made from pure fused silica shows an extremely high Q_{TED} of 6.83×10^{10}. This confirms that the combination of mode and material choice is an excellent way to minimize the effect of TED. However, when the simulations are refined to include an AlN film on top of the silica resonator, the simulated Q_{TED} drops to 7.5×10^{4}. From this, it is implied that the addition of the AlN layer is inducing a large temperature gradient and therefore additional TED related loss. This appears to be a dominant loss mechanism in this device, and so further investigation into this loss mechanism is discussed and addressed in the next chapter.

Table 2.2
COMSOL Simulated Performance for Various Piezoelectric Layers (Radial Extensional Mode)

	Fused Silica Only	**Fused Silica w/AlN**
Simulated Frequency (MHz)	4.89	5.03
Simulated Q_{Anchor}	1.4×10^{6}	1.2×10^{6}
Simulated Q_{TED}	6.83×10^{10}	7.49×10^{4}

Measured AlN-on-Silica Results

The S-parameter response of fabricated resonators as measured using an Agilent E5061b

vector network analyzer in a Lakeshore TTPX cryogenic probe station at room temperature in a vacuum less than 10 mTorr. The response of the radial extensional in-phase and out-of-phase mode response is shown in Fig. 2.6. In order to avoid any *Q* loading effects from different input or output terminations between network analyzers or circuit implementations, the unloaded *Q* (Q_u) is extracted through a simple equation [34]:

$$Q_u = \frac{Q_L}{1-10^{-\frac{IL}{20}}}, \qquad \text{(Equation 2.2)}$$

where Q_L is the loaded *Q* of the resonator and IL is the measured insertion loss of the resonator. This estimation of unloaded *Q* becomes more accurate as insertion loss increases, showing minimal error over 10 dB. To aid in comparison between devices, all measured *Q*s shown in this work have been transformed to unloaded *Q*s. The in-phase peak is seen at 4.96 MHz with an insertion loss of 16.9 dB and a *Q* of 19,671, while the out-of-phase peak is at 4.88 MHz with an insertion loss of 12.8 dB and a *Q* of 26,645. While both in-phase and out-of-phase modes show similar results, the in-phase mode is simulated and designed to have lower anchor loss due to the nodal point on the coupling rod. The out-of-phase mode does not have this nodal point, and will be limited by anchor loss as resonator performance improves. Therefore, the primary mode for these resonators will be the in-phase mode and the out-of-phase mode will not be considered further. It is important to note that the simulated Q_{TED} of 75,000 of the AlN-on-silica devices and the measured *Q*s of 19,671 and 26,645 are within an order of magnitude from each other, which suggests that TED-based losses may be limiting device performance. From this, a further investigation of TED is a good place to begin for improving the measured *Q*. The optimized anchor performance on the fused silica resonators allows for very low loss through the anchors, eliminating this loss source as a potential dominant factor in the measured results, whereas

pressure-based losses are removed due to the use of a vacuum chamber. In addition to the designed in-phase radial extensional dogbone mode, there are two other modes of note that were measured from these resonators. These two modes, shown in Fig. 2.7, are an in-plane shear mode (left) and the third-order radial extensional mode (right). The in-plane shear mode shows a very high *Q* of 46,203 at 2.9 MHz, but has a much higher insertion loss of 47.3 dB due to poor shear actuation and pick-up through the d_{31} coefficient of AlN. The third order radial extensional mode shows a lower *Q* than its fundamental mode shown above, but at a higher frequency of 16.4 MHz. Neither of these measured modes provides a better combination of high-*Q* and low insertion loss, and therefore is not investigated for further improvement.

There are a few additional considerations when determining the viability of a measured resonator for use as a timing reference. As previously discussed in Chapter 1, one important measurement is the power handling of the resonator, which has an inversely proportional effect on the phase noise of an electrical oscillator [35]. Power handling is a metric that piezoelectric resonators tend to excel in as compared to other actuation methods, as non-linear responses due to actuation gap instability are not an issue. The power handling capability of the fabricated dogbone devices in its radial extensional mode can be seen in Fig. 2.8. When the applied source power to the resonator is higher than -5 dBm, nonlinear material effects become apparent, shifting the resonant frequency of the peak upwards and distorting the peak of the response. Very obvious response degradation can be seen at source powers of +2 dBm, where the non-linear material effects begin to dominate the response. The power handling is limited by non-linear material effects and the delivered power to the resonator, which is controlled by the insertion loss. A resonator with a lower insertion loss, such as the dogbone resonator, will have lower power handling to a similar resonator with a higher insertion loss as more input power is reflected back.

A more in depth discussion of this effect in dogbone resonators can be found in [36].

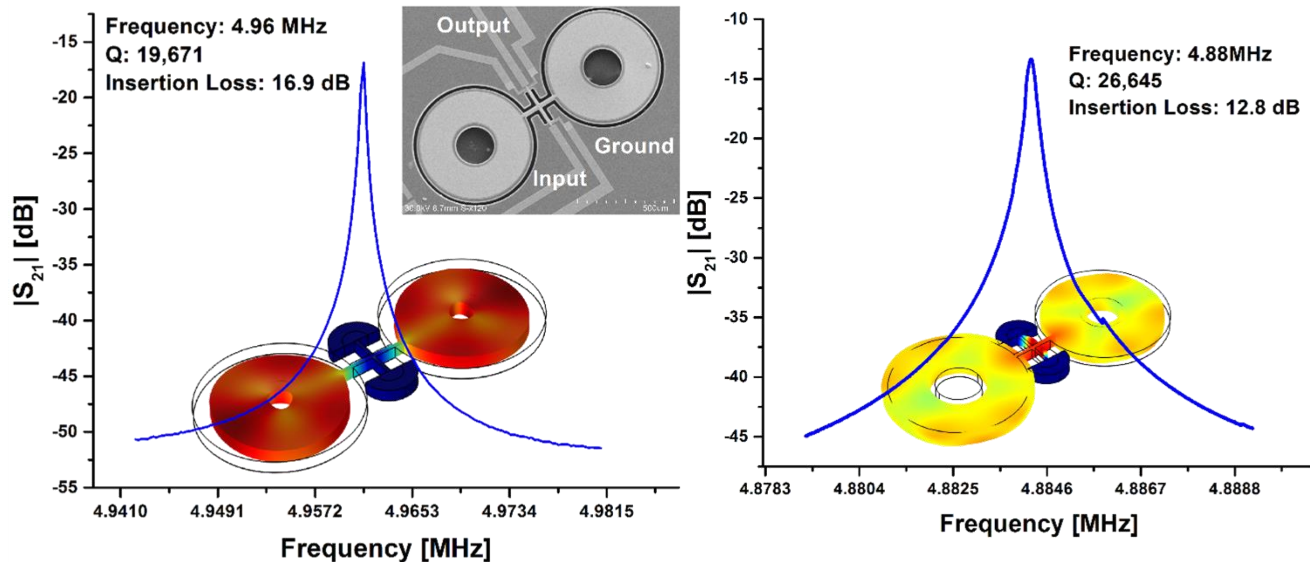

Fig. 2.6: Measured S_{21} response and mode shape of an in-phase (right) and out-of-phase (left) fused silica dogbone resonator. Inset shows a SEM of a fabricated resonator with labeled inputs. Background shows simulated mode shape for each mode.

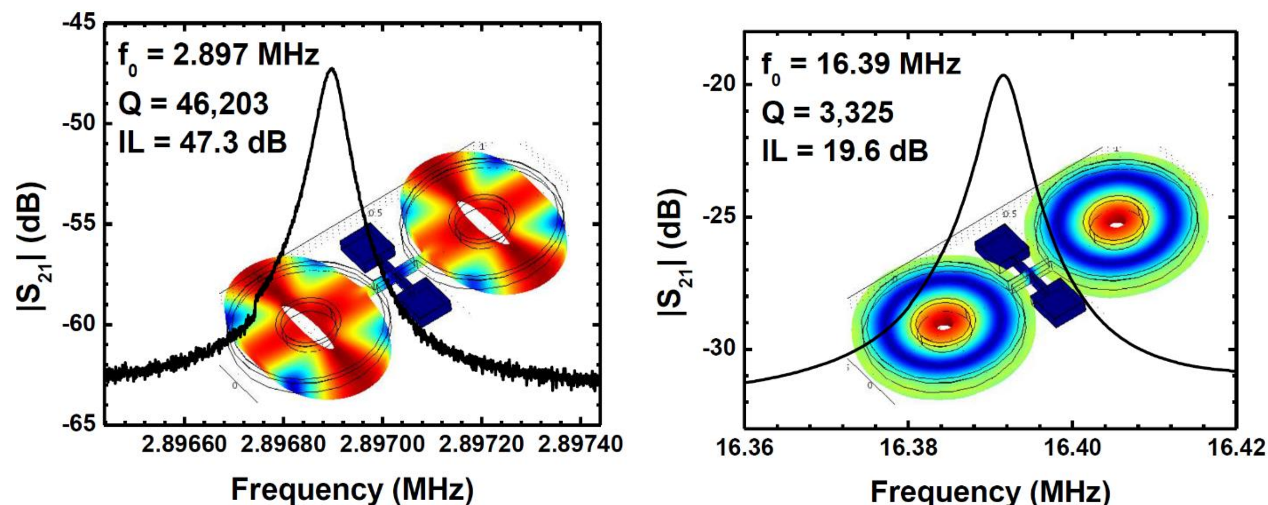

Fig. 2.7: Measured S_{21} responses for an in-phase shear mode and mode shape at 2.9 MHz (left) and a third-order radial extensional response and mode shape at 16.39 MHz (right). Images adapted from [20].

A second important resonator metric for device stability is its TCF. The temperature stability of a resonator defines its frequency accuracy over temperature shifts and needs to be addressed in order to achieve ultra-stable references. The TCF data for a number of measured dogbone modes in the temperature range between -40 ºC to 80 ºC can be seen in Fig. 2.9. It is immediately apparent that the sensitivity of fused silica to temperature regardless of resonant mode

is much higher than that found in uncompensated silicon. In order to produce ultra-stable references, mitigation methods for this large TCF will need to be considered. This TCF mitigation effort will be the focus of Chapter 4.

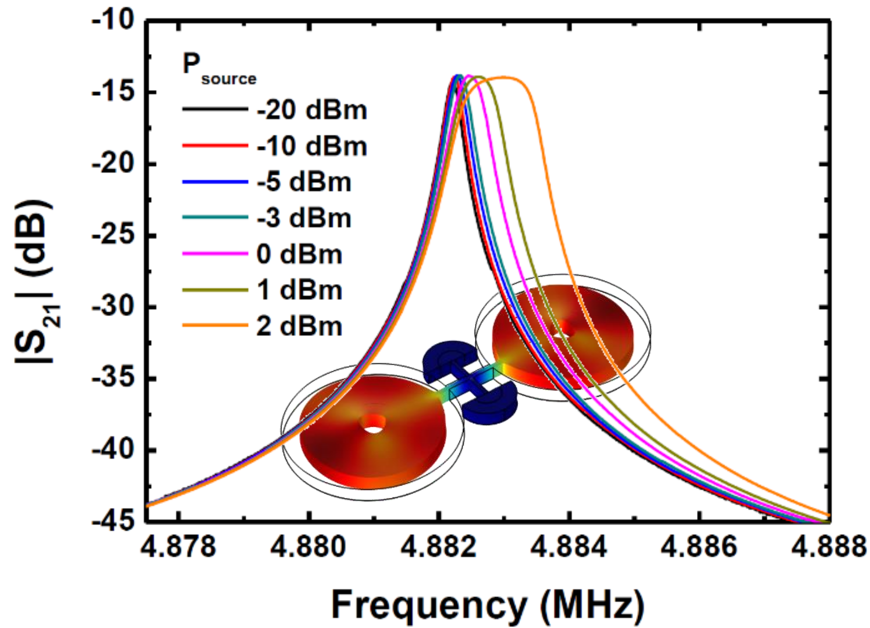

Fig. 2.8: Measured power handling of a radial extensional fused silica resonator showing a power-handling higher than -5 dBm. Background shows simulated mode shape. Image adapted from [20].

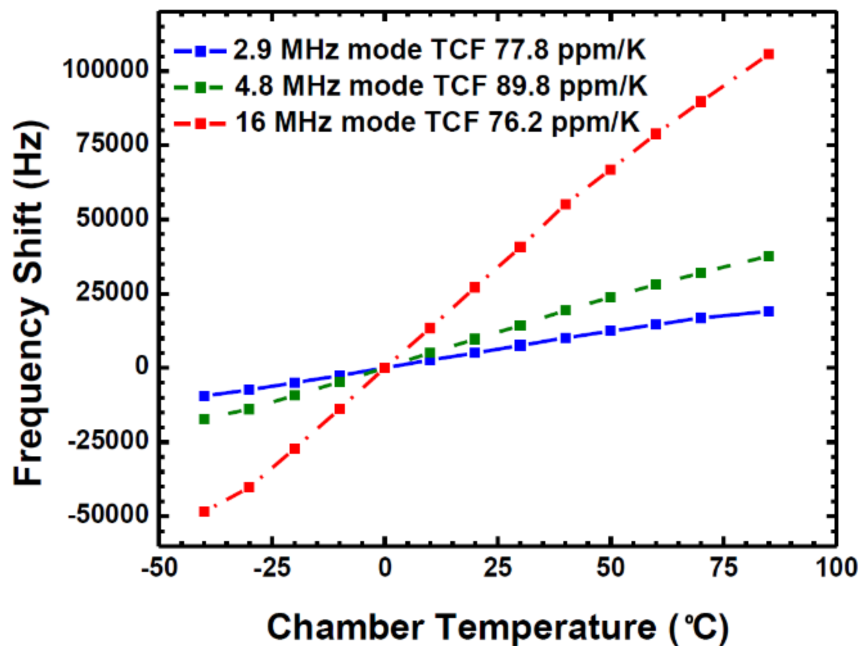

Fig. 2.9: Measured frequency shift via temperature for three different modes on a fabricated fused silica resonator. Note that the temperature sensitivity in uncompensated silica is substantially higher than that found in silicon. Image adapted from [20].

The end goal of resonator development is integration into an oscillator for use as a timing reference. To this end, it is critical that the long-term stability of the AlN-on-silica resonators is understood and addressed. In this case, long-term stability is considered to be in the hour range onwards, extending to days and/or years. The aging characteristics of the devices measured in Fig. 2.6 and Fig. 2.7 is shown in Fig. 2.10. This measurement was done over a 100-hour period, with the first two hours used as a burn-in period and not included in the data. These measurements were done in vacuum at an uncontrolled room temperature to simulate typical operating conditions, which adds temperature and therefore frequency fluctuations due to the large natural TCF of fused silica. In the 98-hour measurement period there was a total of 536 Hz of drift, which is equivalent to 109 ppm total shift. If the initial large peak is ignored and only the last 60 hours examined, the total shift is 257 Hz (52 ppm total). In either case, this shift is larger than our desired accuracy for the timing reference, and highlights the requirement for extreme temperature stability and robust packaging in order to keep device drift within specifications. The temperature stability aspect can be addressed through ovenization and temperature compensation, explored in more depth in Chapter 4, while packaging is outside the scope of this work and is not considered. It should be noted that packaging and hermetic sealing for the timing reference is a critical aspect in maintaining stability and is of the utmost importance in order to achieve the requirements for the desired timing reference applications.

From the measured results, it can be noted that the fused silica dogbone resonators demonstrate a Q that is lower than was simulated using the previously introduced COMSOL models for anchor and TED losses. Additional investigation into these and other loss mechanisms is necessary to determine the performance limitations of the fused silica resonators and is the focus

of the following chapter.

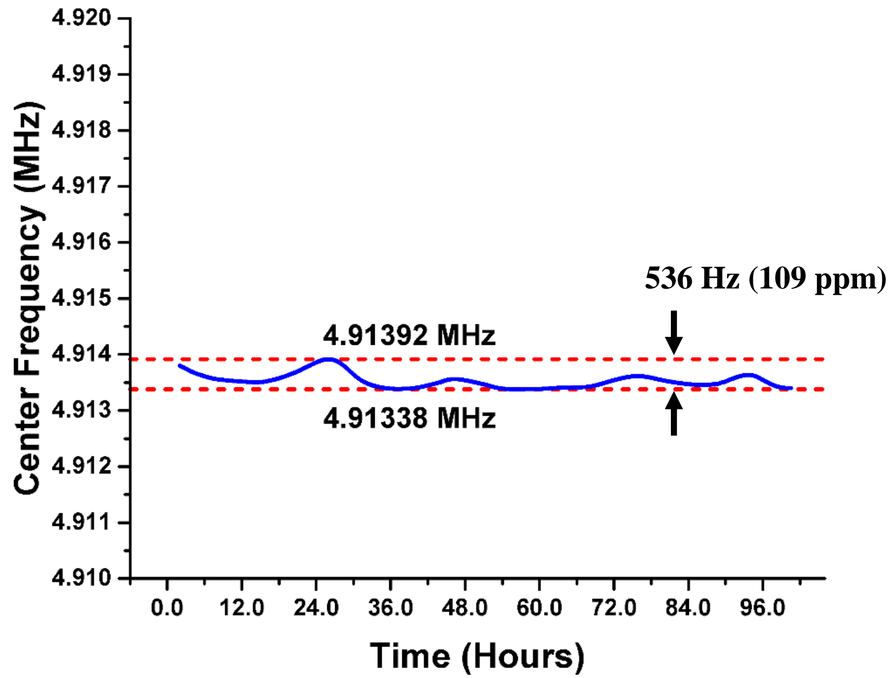

Fig. 2.10: Measured frequency stability (aging) for the radial extensional mode of an AlN-on-silica resonator over a 98-hour period. The first two hours from the 100-hour measurement period were excluded for device burn-in. The total frequency drift over the measurement period was 536 Hz (109 ppm), or if only the last 60 hours are considered a total drift of 257 Hz (52 ppm) is measured.

References

[1] H. Lee, A. Partridge and F. Assaderaghi, "Low jitter and temperature stable MEMS oscillators," in *Proceedings of the IEEE International Frequency Control Symposium Proceedings (IFCS),* 2012, pp. 1-5.

[2] H. Bhugra, Y. Wang, W. Pan, D. Lei and S. Lee, "High performance pMEMS™ oscillators - the next generation frequency references," in *Proceedings of the International Electron Devices Meeting (IEDM),* Washington, DC, USA, 2011, pp. 20.1.1-20.1.4.

[3] R. Ruby, "Positioning FBAR technology in the frequency and timing domain," in *Proceedings of the Joint Conference of the IEEE International Frequency Control and the European Frequency and Time Forum (FCS),* San Fransisco, CA, USA, 2011, pp. 1-10.

[4] Yu-Wei Lin, Sheng-Shian Li, Zeying Ren and C. T. -. Nguyen, "Low phase noise array-composite micromechanical wine-glass disk oscillator," in *Proceedings of the IEEE International Electron Devices Meeting (IEDM),* Washington, DC, USA, 2005, pp. 278-281.

[5] P. Amico, L. Bosi, L. Carbone, L. Gammaitoni, F. Marchesoni, M. Punturo, F. Travasso and H. Vocca, "Monolithic fused silica suspension for the Virgo gravitational waves detector," *Rev. Sci. Instrum.,* vol. 73, pp. 3318, Aug., 2002.

[6] T. Nagourney, J. Cho, A. Darvishian, B. Shiari and K. Najafi, "130 second ring-down time and 3.98 million quality factor in 10 kHz fused silica micro birdbath shell resonator," in *Proceedings of Solid-State Sensors, Actuators and Microsystems Workshop,* Hilton Head Island, SC, USA, 2016, pp. 408-411.

[7] Corning, "HPFS Product Brochure All Grades," *Corning HPFS 7979, 7980, 8655 Fused Silica Datasheet,* July, 2015.

[8] V. Kaajakari, T. Mattila, A. Oja and H. Seppa, "Nonlinear limits for single-crystal silicon microresonators," *J. Microelectromech. Syst.,* vol. 13, pp. 715-724, Oct., 2004.

[9] G. K. Ho, R. Abdolvand, A. Sivapurapu, S. Humad and F. Ayazi, "Piezoelectric-on-silicon lateral bulk acoustic wave micromechanical resonators," *J. Microelectromech. Syst.,* vol. 17, pp. 512-520, Apr., 2008.

[10] R. C. Ruby, P. Bradley, Y. Oshmyansky, A. Chien and J. Larson, "Thin film bulk wave acoustic resonators (FBAR) for wireless applications," in *Proceedings of the IEE Ultrasonics Symposium,* Atlanta, GA, USA, 2001, pp. 813-821.

[11] R. Abdolvand, H. M. Lavasani, G. K. Ho and F. Ayazi, "Thin-film piezoelectric-on-silicon resonators for high-frequency reference oscillator applications," *IEEE Trans. Ultrason. Ferroelectr. Freq. Control,* vol. 55, pp. 2596-2606, Dec., 2008.

[12] Y. Hwang, H. Jung, E. Song, I. Hyeon, Y. Kim and C. Baek, "Fabrication of electrostatically-actuated, in-plane fused quartz resonators using silicon-on-quartz (SOQ) bonding and quartz drie," in *Proceedings of the 22nd IEEE International Conference on Micro Electro Mechanical Systems (MEMS),* Sorrento, Italy, 2009, pp. 729-732.

[13] A. Grosse, M. Grewe and H. Fouckhardt, "Deep wet etching of fused silica glass for hollow capillary optical leaky waveguides in microfluidic devices," *J. Micromech. Microengineering,* vol. 11, pp. 257-262, 2001.

[14] Junseok Chae, J. M. Giachino and K. Najafi, "Fabrication and characterization of a wafer-level MEMS vacuum package with vertical feedthroughs," *J. Microelectromech. Syst.,* vol. 17, pp. 193-200, Feb., 2008.

[15] E. Belloy, S. Thurre, E. Walckiers, A. Sayah and M. A. M. Gijs, "The introduction of powder blasting for sensor and microsystem applications," *Sensors and Actuators A: Physical,* vol. 84, pp. 330-337, Jan., 2000.

[16] J. A. Plaza, M. J. Lopez, A. Moreno, M. Duch and C. Cané, "Definition of high aspect ratio glass columns," *Sensors and Actuators A: Physical,* vol. 105, pp. 305-310, Aug., 2003.

[17] J. Y. Cho, J. Woo, J. Yan, R. L. Peterson and K. Najafi, "Fused-silica micro birdbath resonator gyroscope (μ-BRG)," *J. Microelectromech Syst.,* vol. 23, pp. 66-77, Feb., 2014.

[18] M. J. Ahamed, D. Senkal and A. M. Shkel, "Effect of annealing on mechanical quality factor of fused quartz hemispherical resonator," in *Proceedings of the International Symposium on Inertial Sensors and Systems (ISISS),* Laguna Beach, CA, USA, 2014, pp. 1-4.

[19] Z. Cao, B. VanDerElzen, K. J. Owen, J. Yan, G. He, R. L. Peterson, D. Grimard and K. Najafi, "DRIE of fused silica," in *Proceedings of the 26th IEEE International Conference on Micro Electro Mechanical Systems (MEMS),* Taipei, Taiwan, 2013, pp. 361-364.

[20] Z. Wu, A. Peczalski, V. A. Thakar, Z. Cao, Y. Yuan, G. He, R. L. Peterson, K. Najafi and M. Rais-Zadeh, "Piezoelectrically transduced high-Q silica micro resonators," in *Proceedings of the 26th IEEE International Conference on Micro Electro Mechanical Systems (MEMS),* San Francisco, CA, USA, 2013, pp. 122-125.

[21] Y. Yang, E. J. Ng, C. H. Ahn, V. A. Hong, E. Ahadi and T. W. Kenny, "Mechanical coupling of dual breathe-mode ring resonator," in *Proceedings of the 17th International Conference on Solid-State Sensors, Actuators and Microsystems (TRANSDUCERS & EUROSENSORS),* Barcelona, Spain, 2013, pp. 502-505.

[22] B. Bircumshaw, G. Liu, H. Takeuchi, Tsu-Jae King, R. Howe, O. O'Reilly and A. Pisano, "The radial bulk annular resonator: Towards a 50Ω RF MEMS filter," in *Proceedings of the 12th International Conference on Solid-State Sensors, Actuators and Microsystems (TRANSDUCERS & EUROSENSORS),* Boston, MA, USA, 2003, pp. 875-878.

[23] Y. Xie, S. S. Li, Y. W. Lin, Z. Ren and C. T. Nguyen, "1.52-GHz micromechanical extensional wine-glass mode ring resonators," *IEEE Trans. Ultrason. Ferroelectr. Freq. Control,* vol. 55, pp. 890-907, Apr., 2008.

[24] K. Wang, A. Wong and C. T. Nguyen, "VHF free-free beam high-Q micromechanical resonators," *J. Microelectromech Syst.,* vol. 9, pp. 347-360, Sept., 2000.

[25] B. Harrington and R. Abdolvand, "In-plane acoustic reflectors for reducing effective anchor loss in lateral-extensional MEMS resonators," *J. Micromech. Microengineering,* vol. 21, pp. 085021, July, 2011.

[26] R. Tabrizian and F. Ayazi, "Acoustically-engineered multi-port AlN-on-silicon resonators for accurate temperature sensing," in *Proceedings of the IEEE International Electron Devices Meeting (IEDM),* Washington D.C., USA, 2013, pp. 18.1.1-18.1.4.

[27] J. E. Lee, J. Yan and A. A. Seshia, "Study of lateral mode SOI-MEMS resonators for reduced anchor loss," *J. Micromech. Microengineering,* vol. 21, pp. 045010, Mar., 2011.

[28] D. S. Bindel and S. Govindjee, "Elastic PMLs for resonator anchor loss simulation," *Int. J. Numer. Methods Eng.,* vol. 64, pp. 789-818, Feb., 2005.

[29] Z. Hao, A. Erbil and F. Ayazi, "An analytical model for support loss in micromachined beam resonators with in-plane flexural vibrations," *Sensors and Actuators A: Physical,* vol. 109, pp. 156-164, Dec., 2003.

[30] V. Thakar and M. Rais-Zadeh, "Optimization of tether geometry to achieve low anchor loss in lamé-mode resonators," in *Proceedings of the Joint European Frequency and Time Forum and International Frequency Control Symposium (EFTF/IFC),* Prague, Czech Republic, 2013, pp. 129-132.

[31] C. Zener, "Internal friction in solids. I: theory of internal friction in reeds," *Physical Review,* vol. 52, pp. 230-235, 1937.

[32] S. A. Chandorkar, M. Agarwal, R. Melamud, R. N. Candler, K. E. Goodson and T. W. Kenny, "Limits of quality factor in bulk-mode micromechanical resonators," in *Proceedings of the 21st IEEE International Conference on Micro Electro Mechanical Systems,* Tuscon, AZ, USA, 2008, pp. 74-77.

[33] A. Duwel, R. N. Candler, T. W. Kenny and M. Varghese, "Engineering MEMS resonators with low thermoelastic damping," *J. Microelectromech. Syst.,* vol. 15, pp. 1437-1445, Dec., 2006.

[34] H. Zhu and J. E. Lee. AlN piezoelectric on silicon MEMS resonator with boosted Q using planar patterned phononic crystals on anchors. Presented at Proceedings of the 28th IEEE International Conference on Micro Electro Mechanical Systems (MEMS). 2015.

[35] D. B. Leeson, "A simple model of feedback oscillator noise spectrum," *Proc. IEEE,* vol. 54, pp. 329-330, Dec., 1966.

[36] Z. Wu, "Microelectromechanical systems for wireless radio front-ends and integrated frequency references," *University of Michigan, Ph. D. Thesis,* 2014.

Chapter 3: Loss Effects in Fused Silica Resonators

With demonstrated fabricated aluminum nitride (AlN)-on-silica resonators, the next task is to maximize the performance of these resonators, most importantly the quality factor (*Q*). As previously discussed in Chapter 1, the *Q* is directly related to the resultant phase noise and therefore accuracy and stability of the fabricated oscillator and is a critical metric towards achieving ultra-stable timing references [1]. The measured results show a *Q* of 19,671 for the in-phase radial extensional mode and 26,645 for the out-of-phase radial extensional mode, while the COMSOL simulated results shown in Table 2.1 suggest a higher *Q* of 75,000. These numbers are on the same order of magnitude, and differences in material properties could account for this performance difference. In order to understand the difference between experimental and simulated results, address the dominant loss mechanisms, and increase performance it is necessary to determine which loss factor is currently limiting resonator *Q*. As the most likely performance bottleneck is thermoelastic damping (TED), it is necessary to investigate the cause of TED, especially in multi-layer resonator structures such as the AlN-on-silica platform.

TED in Single Material Resonators

The first step in understanding TED is to examine the source of the loss in a simple system. Zener's original formulation of TED, first proposed in the 1960's, focused on the creation of stress gradients in a long, slender flexing beam undergoing harmonic vibration. These stress gradients result in heat gradients across the resonator body due to lattice compression or expansion. These heat gradients attempt to resolve themselves, which in turn causes periodic heat conduction that

can lag behind the stress gradient, causing irreversible energy loss [2]. Zener's governing equation for this loss mechanism can be written for a long, slender beam as [3]:

$$Q_{TED}^{-1} = \frac{E\alpha^2 T_0}{C}\left(\frac{\omega\tau}{1+(\omega\tau)^2}\right), \quad \tau = \frac{Ct^2}{\pi^2 k} \qquad \text{(Equation 3.1)}$$

where E is the Young's modulus of the beam, α is the coefficient of thermal expansion (CTE), C is the volumetric heat capacity, ω is the resonant frequency of the beam in radians, τ is the relaxation time and t is the thickness of the beam. It is important to note that frequency has a large effect on TED in this equation, as higher resonance frequencies show lower TED due to insufficient time for thermal gradients to resolve before the next harmonic cycle. Similarly, for very low frequencies the thermal gradients can more easily follow the stress gradients, reducing heat conduction and therefore loss. Most timing references manufactured today need to consider TED, as they operate in frequency regions between these two frequency regions and typically use relatively large thermal conductivity materials.

TED in Multi-Layer Resonators

Zener's equation, shown in Eq. 3.1, only holds for single material flexing beams and needs to be modified when additional layers are introduced into the material stack. Such an equation has been previously derived for multi-layer beams [3] and the resultant equation can be used to predict how the presence of an AlN film on a silica substrate affects TED. The equation of the analytical model can be seen in Equation 3.2 and Equation 3.3a-g [3].

$$Q_{TED}^{-1} = \frac{E_S\alpha_S T_0}{C_S}\left(\frac{\sum_{n=1}^{\infty}\frac{\omega\tau_S\gamma_n^2}{(\omega\tau_S)^2+\gamma_n^4}\Lambda_n}{\frac{1}{3}\left\{\left[\left(\frac{z_1-z_0}{z_2}\right)^3+\left(\frac{z_0}{z_2}\right)^3\right]+\frac{E_f}{E_S}\left[\left(\frac{z_2-z_0}{z_2}\right)^3-\left(\frac{z_1-z_0}{z_2}\right)^3\right]\right\}}\right), \qquad \text{(Equation 3.2)}$$

where:

$$\Lambda_n = \frac{\left[\left(\frac{z_1}{z_2}\right)^2 J_I + \frac{E_f \alpha_f}{E_s \alpha_s} J_{II}\right]^2}{\frac{z_1}{z_2} J_{III} + \frac{C_f}{C_s} J_{IV}} \qquad \text{(Equation 3.3a)}$$

$$J_I = \frac{1}{\gamma_n^2} \cos(\gamma_n - 1) + \frac{1}{\gamma_n}\left(1 - \frac{z_0}{z_1}\right) \sin \gamma_n \qquad \text{(Equation 3.3b)}$$

$$J_{II} = \frac{1}{\eta_n}\left\{A_n \left[\frac{1}{\eta_n}\left(\cos \eta_n - \cos \frac{\eta_n z_1}{z_2}\right) + \sin \eta_n - \frac{z_1}{z_2} \sin \frac{\eta_n z_1}{z_2}\right] + B_n \left[\frac{1}{\eta_n}\left(\sin \eta_n - \sin \frac{\eta_n z_1}{z_2}\right) - \cos \eta_n + \frac{z_1}{z_2} \cos \frac{\eta_n z_1}{z_2}\right] + \frac{z_0}{z_2}\left[A_n\left(\sin \frac{\eta_n z_1}{z_2} - \sin \eta_n\right) + B_2 \left(\cos \eta_n - \cos \frac{\eta_1 z_1}{z_2}\right)\right]\right\} \qquad \text{(Equation 3.3c)}$$

$$J_{III} = \frac{1}{2} + \frac{1}{4\gamma} \sin 2\gamma_n \qquad \text{(Equation 3.3d)}$$

$$J_{IV} = \left\{\frac{1}{2}\left(1 - \frac{z_1}{z_2}\right)(A_n^2 + B_n^2) + \frac{1}{4\eta_n}(A_n^2 - B_n^2)\left(\sin 2\eta_n - \sin \frac{2\eta_n z_1}{z_2}\right) - \frac{1}{2\eta_n} A_n B_n \left(\cos 2\eta_n - \cos \frac{2\eta_n z_1}{z_2}\right)\right\} \qquad \text{(Equation 3.3e)}$$

$$A_n = \frac{K \sin \gamma_n \cos \gamma_n}{\left(\sin \eta_n \left(\frac{z_1}{z_2} - 1\right)\right)}, \quad B_n = \frac{K \sin \gamma_n \sin \gamma_n}{\sin\left(\eta_n \left(\frac{z_1}{z_2} - 1\right)\right)}, \quad \gamma_n = \beta_n \sqrt{\tau_s}\ , \quad \eta_n = \beta_n \frac{z_2}{z_2 - z_1} \sqrt{\tau_f} \qquad \text{(Equation 3.3f)}$$

$$\tau_f = \frac{C_f}{k_f}(z_2 - z_1)^2 = \frac{C_f}{k_f} h_f^2\ , \quad \tau_s = \frac{C_s}{k_s} z_1^2 = \frac{C_s}{k_s} h_s^2, \quad K = \sqrt{\frac{k_s C_s}{k_f C_f}} \qquad \text{(Equation 3.3g)}$$

In these equations:

C_s and C_f correspond to the thermal capacity of the substrate and the film respectively.

k_s and k_f correspond to the thermal conductivity of the substrate and the film respectively.

h_s and h_f correspond to the thickness of the substrate and the film respectively.

E_s and E_f correspond to the Young's Modulus of the substrate and the film respectively.

α_s and α_f correspond to the CTE of the substrate and the film respectively.

z_0, z_1 and z_2 correspond to the midpoint z-coordinate of the stack (z_0), the z-coordinate of the substrate/film interface (z_1), and the z-coordinate of the top of the stack (z_2).

β_n corresponds to the eigenvalues of the transcendental equation: $\cot \beta_n \sqrt{\tau_s} \tan \beta_n \sqrt{\tau_f} = -K$.

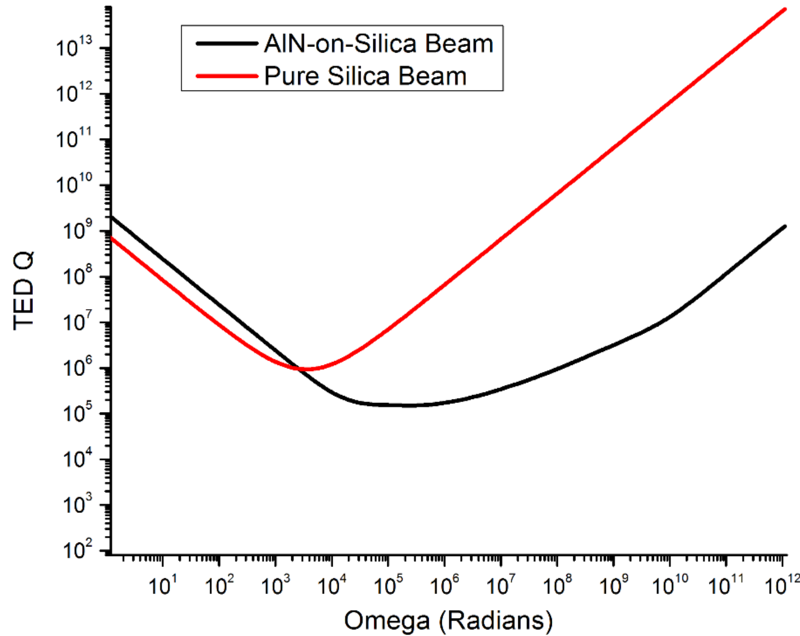

Fig. 3.1: Comparison of the Q_{TED} for a pure silica beam versus a silica beam with a 1 µm AlN film. Note the frequency decrease in the Q minima for the pure beam and the order of magnitude increase in Q_{TED}.

This equation assumes a two material stack consisting of a substrate material and a film material, such as that seen in AlN-on-silica devices. This equation is used to create an analytical model for a 50 µm fused silica beam with a 1 µm thin film of AlN, giving an approximation of the conditions found in the fabricated fused silica resonators. While the radial extensional mode is not directly modeled in this equation, the flexural slender rod assumption made here allows the examination of trends in TED losses and helps investigate causes of the loss introduced through multiple layers. An analytically calculated comparison between this multi-layer analytical estimation and Zener's equation for a single material beam is shown in Fig. 3.1. The Q_{TED} minima is at a lower frequency for a pure silica beam and the entire curve is shifted, a full order of magnitude lower, with an AlN film present. It is clear that a significant decrease in Q_{TED} is seen

when an AlN film is added to the fused silica substrate, which matches what was seen in the COMSOL simulation results presented in the previous chapter.

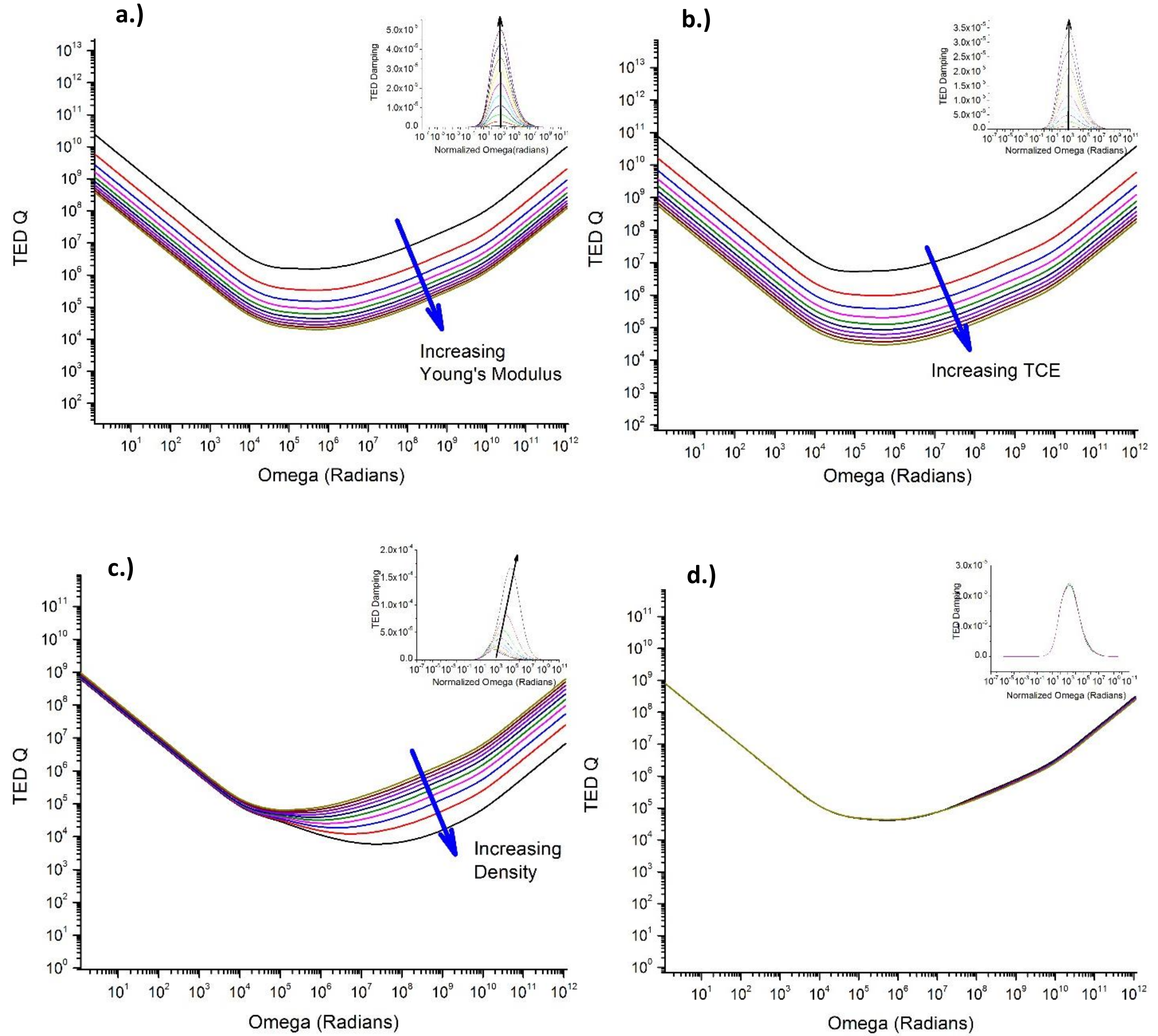

Fig. 3.2: Parameter sweep plots of Q_{TED} versus angular frequency. A 1 μm AlN film on a 50 μm silica beam has one material parameter of the AlN film swept from low to high. Inset shows the TED damping for the same beam over a normalized frequency. a.) Sweep of Young's Modulus from 50 GPa to 500 GPa.in 50 GPa increments b.) Sweep of thermal coefficient of expansion (CTE) from $0.5{\times}10^{-6}$ to $5{\times}10^{-6}$ in $0.5{\times}10^{-6}$ increments. c.) Sweep of density from 500 kg/m^3 to 5,000 kg/m^3 in 500 kg/m^3 increments. d.) Sweep of thermal conductivity from 10 W/mK to 100 W/mK in 10 W/mK increments.

To better understand the origin of this additional loss caused by an additional layer, each material parameter of the thin film layer was investigated in regard to its impact on the overall

Q_{TED} of the beam. The analysis shows that the material parameter match between the fused silica substrate and AlN film has a large impact on the Q_{TED} of the system, with Young's modulus and CTE having the largest effects. The results of this analysis are shown in Fig. 3.2 a-d, where all material parameters of the AlN film are isolated and then individually swept from the value of fused silica upwards, increasing the mismatch between parameters. For example, in Fig. 3.2a the AlN-on-silica beam has normal material parameters for both the fused silica beam and the AlN film, except for the Young's modulus of the AlN film. The Young's modulus starts at 50 GPa and is swept upwards in 50 GPa increments to a final value of 500 GPa. The analytically calculated Q_{TED} results for each step are then plotted in order to examine the trends. The calculated Q_{TED} is plotted versus the resonance frequency in radians, ω, with the inset plotting the calculated damping ($1/Q_{TED}$) versus a normalized frequency, $\omega\tau_s = \omega C_s h_s^2/k_s$, which removes the material parameter dependence of the beam. Young's modulus, CTE, density, and thermal conductivity were each swept for the AlN film, with Young's modulus and CTE showing the largest effect on Q_{TED}. Density showed notable effects only at frequencies above the Q_{TED} minima, which are too large to affect the dogbone resonators at their radial extensional frequency. With all parameters, the best performance was seen when the material parameters between the fused silica and the AlN were closely matched. This can be at least partly attributed to stress gradients created at material interfaces due to instantaneous jumps in Young's modulus and CTE, which would cause additional heat generation and dissipation [4]. From these results, we can hypothesize that the Q_{TED} of the AlN-on-silica resonators can be improved by selecting piezoelectric materials that closely match the parameters of the substrate material. This can be further investigated by analytically comparing two similar beams, one with a lead zirconate titanate (PZT) piezoelectric film and one with an AlN film, shown in Fig. 3.3. As hypothesized, a marked improvement in performance is seen with the

PZT film versus the AlN film. It is important to note that these analytical calculations are done for long, slender flexing beams, while the measured AlN-on-silica resonators are actuated in a radial extensional mode. Due to this, the exact solutions found here are not expected to hold for dogbone resonators actuated in their radial extensional mode. With this said, both types of resonance modes undergo a volumetric change during their resonance cycle, so a similar qualitative trend can be expected from the dogbone devices. With an analytical trend in hand, it can be extended towards COMSOL simulations and experimental results to determine the films effect on dogbone devices.

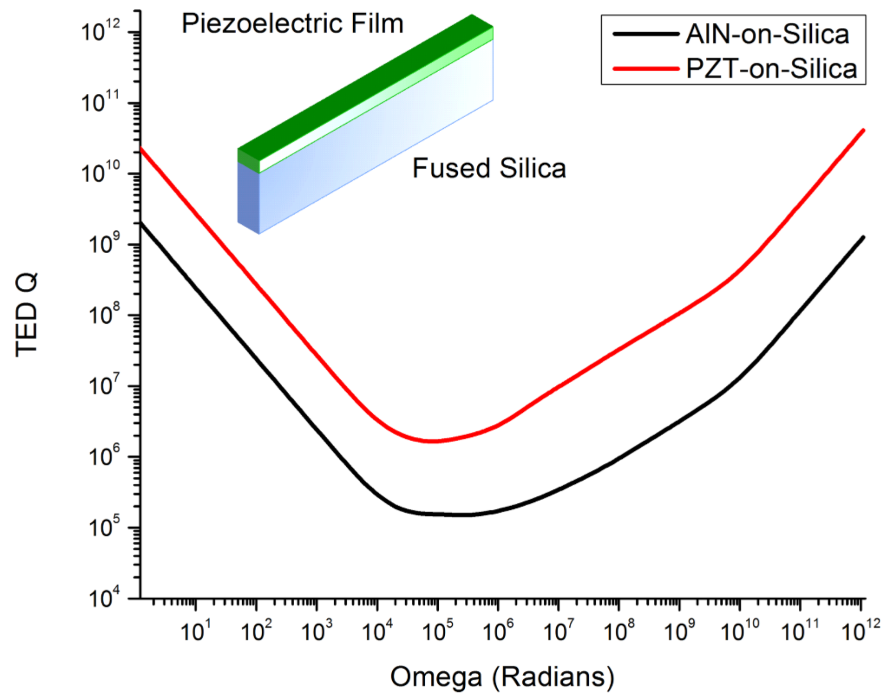

Fig. 3.3: Analytical Q_{TED} comparison for a 1 µm AlN film or a 1 µm PZT film on a 50 µm silica beam. Inset shows a schematic of the AlN-on-silica beam. Note that as predicted the PZT-on-silica beam predicts a substantially better Q_{TED} than the AlN-on-silica beam.

PZT-on-Silica Resonators

In order to determine if TED is the limiting loss mechanism in piezoelectric fused silica resonators, a piezoelectric material with a close material parameter match to fused silica is required. A material that fulfills this criterion is PZT. Table 3.1 shows the material properties for fused silica, AlN, and PZT used for simulations and analytical calculations [5, 6]. It can be noted

that the match between Young's modulus and CTE for fused silica and PZT is closer than that found in fused silicon and AlN, which should increase the expected Q_{TED} of the fabricated devices. COMSOL simulations for TED loss [7] were done for all variations of piezoelectric material and fused silica to confirm the analytical model, with the results shown in Table 3.2. The results agree with the expected TED loss trends, with PZT-on-silica resonators showing substantially higher performance than the simulated AlN-on-silica devices. If TED is the limiting loss mechanism, it is expected that the measured Q of fabricated PZT-on-silica devices should be substantially higher than the Q achieved using AlN-on-silica.

Table 3.1
Material Constants Used in COMSOL Simulations

	Fused Silica	***AlN***	***PZT [5, 6]***
Young's Modulus (GPa)	72.7	309	77
Poisson's Ratio	0.16	0.287	0.31
Mass density (kg·m^{-3})	2201	3260	7800
Thermal expansion coefficient (K^{-1})	0.57×10^{-6}	4.2×10^{-6}	3.5×10^{-6}
Thermal conductivity (W·m^{-1}·K^{-1})	1.3	60	1.2
Specific heat capacity (J·kg^{-1}·K^{-1})	703	600	450

Table 3.2
COMSOL Simulation Results for Q_{TED} of Fused Silica Resonators in Radial Extensional Mode

	Fused Silica Only	**AlN-on-Silica**	**PZT-on-Silica**
Simulated Frequency (MHz)	4.89	5.03	4.78
Simulated Q_{TED}	**6.83×10^{10}**	**7.49×10^{4}**	**1.11×10^{7}**

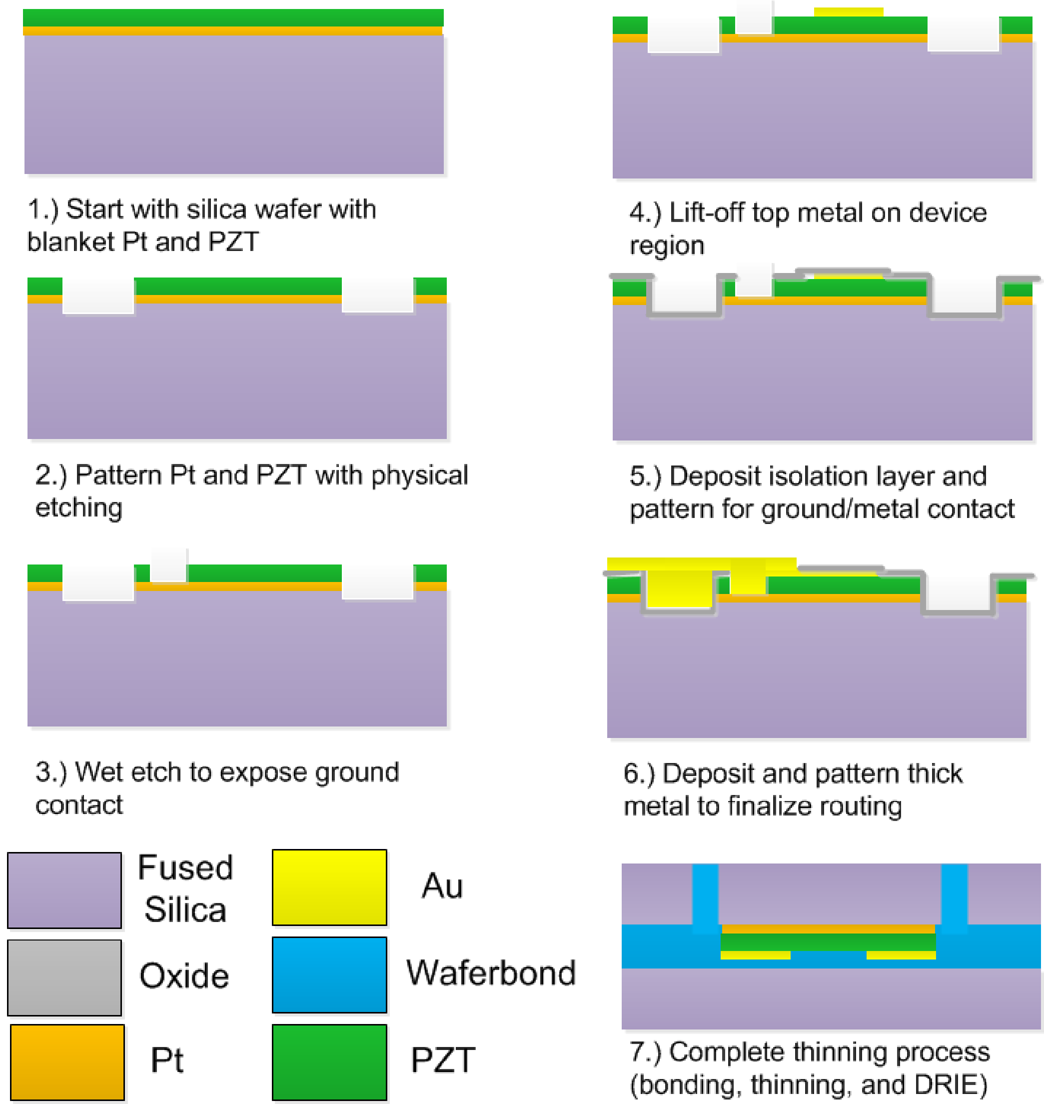

Fig. 3.4: Fabrication flow for the PZT-on-silica process. The piezoelectric stack is blanket deposited and then patterned to create ground contact and routing as necessary.

In order to test this hypothesis, PZT-on-silica devices were fabricated using a modified fabrication process to that shown in Chapter 2. The fabrication flow for these resonators is outlined in Fig. 3.4. The general fabrication process is similar to the process for AlN-on-silica fabrication outlined in Fig. 2.1, except for small differences in piezoelectric stack formation. The stack is composed of a TiO_2/Pt (500 Å) blanket bottom electrode layer, deposited at 500 °C. Next, 500 nm of chemical solution deposition (CSD) PZT is deposited, and finally a 500 Å top metal platinum layer on top. This stack was deposited upon a 525 µm fused silica wafer at the Specialty Electron

Materials and Sensors Cleanroom Facility, U.S. Army Research Laboratory (ARL) in Adelphi, MD using their published CSD process [8]. Once the wafer with the piezoelectric stack is deposited, a physical argon plasma etch is used to pattern the PZT to isolate device regions, followed by a selective PZT wet etch to open contact to the bottom platinum layer. A top metal lift-off process with a 100 Å Cr/1000 Å Pt metal layer is performed for electrode patterning. Next, a 100 nm conformal PECVD oxide layer is deposited at 250 °C to isolate any exposed metal and protect against shorting. One final top metal deposition of 300 Å Cr/5000 Å Au is performed and patterned for line routing and to ensure electrical conductivity across step heights. The remainder of the process follows the process outlined in Fig. 2.1, with wafer bonding, thinning, and DRIE for resonator body definition and release.

A measured S-parameter response for a PZT-on-silica resonator is shown in Fig. 3.5, demonstrating an in-phase Q of 18,000. The measurement setup is identical to that described for AlN-on-silica resonators, with the devices measured in vacuum under 10 mTorr. An approximately 20 Ω short to ground was found in the measured resonators, necessitating a de-embedding process to remove the short and provide a more accurate resonator response. This short is present despite steps taken during fabrication to isolate routing lines and vias, and prevents any additional PZT voltage poling from taking place. The exact cause of this short is unknown, but thought to be caused during the PZT etch step through sidewall re-sputtering leading to metal shorts across the sidewall. This low-resistance short prevents large electric fields from building across the piezoelectric stack without excessive heat generation leading to device failure. This inability to create a large electric field prevents additional PZT polling prior to measurement. While the PZT is poled after CSD deposition prior to the initial stack processing, the lack of pre-measurement poling reduces the piezoelectric coupling and may partially cause the high insertion loss in the

measurement. The measured Q of these resonators is not expected to be highly affected by poor piezoelectric coupling, as the insertion loss shows most of the effect of the short and poor coupling. With this said, it is important to note that the Q of these devices does not show an improvement over that of the AlN-on-silica devices as was expected from the multi-layer TED model and simulations. From this, it can be concluded that TED is not the performance-limiting loss factor for these fused silica resonators and it is necessary to investigate other loss mechanisms to further improve the device performance.

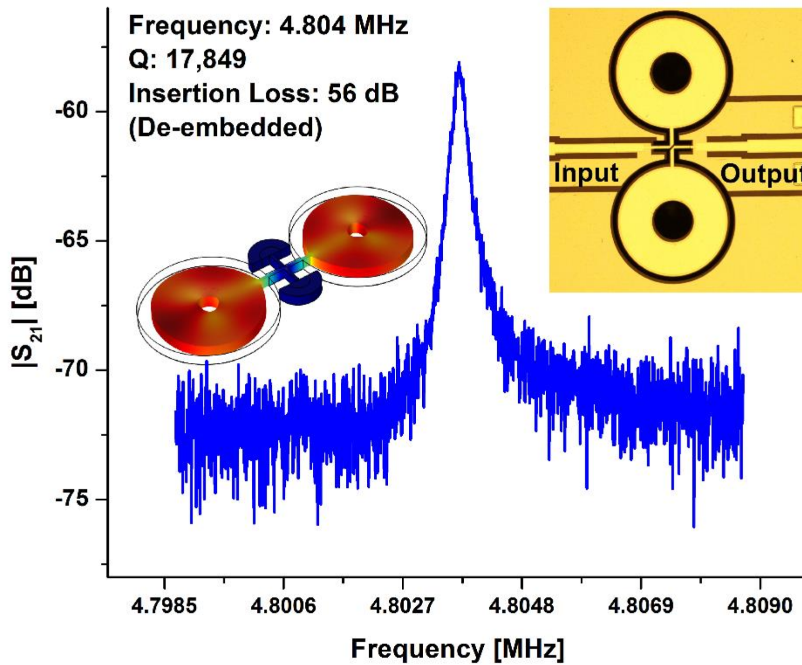

Fig. 3.5: Measured S-parameter response for an in-phase PZT-on-silica resonator with inserts demonstrating simulated mode shape and optical micrograph image. The center frequency is 4.8 MHz, with a Q of 17,849 and a post-processing insertion loss of 56 dB.

AlN-on-Silica Sidewall-Smoothed Resonators

As TED does not appear to be a limiting loss factor, other loss mechanisms need to be considered in order to further improve device performance. One possible loss mechanism is caused by non-idealities in the fabrication of fused silica devices, specifically on the surface of DRIE trenches. Normally, loss due to surface roughness on resonators operating under vacuum is minimal. However, the fused silica DRIE process creates large striations along the sidewall of the

resonator and this roughness may cause a significant amount of energy to be dissipated [9]. As shown in Fig. 2.3, the striations created by the fused silica DRIE process can reach up to 1 μm in height and stretch across the entire depth of the trench. To test if these sidewalls were affecting the resonator performance, a novel sidewall smoothing process was devised to smooth the DRIE trenches post-etch.

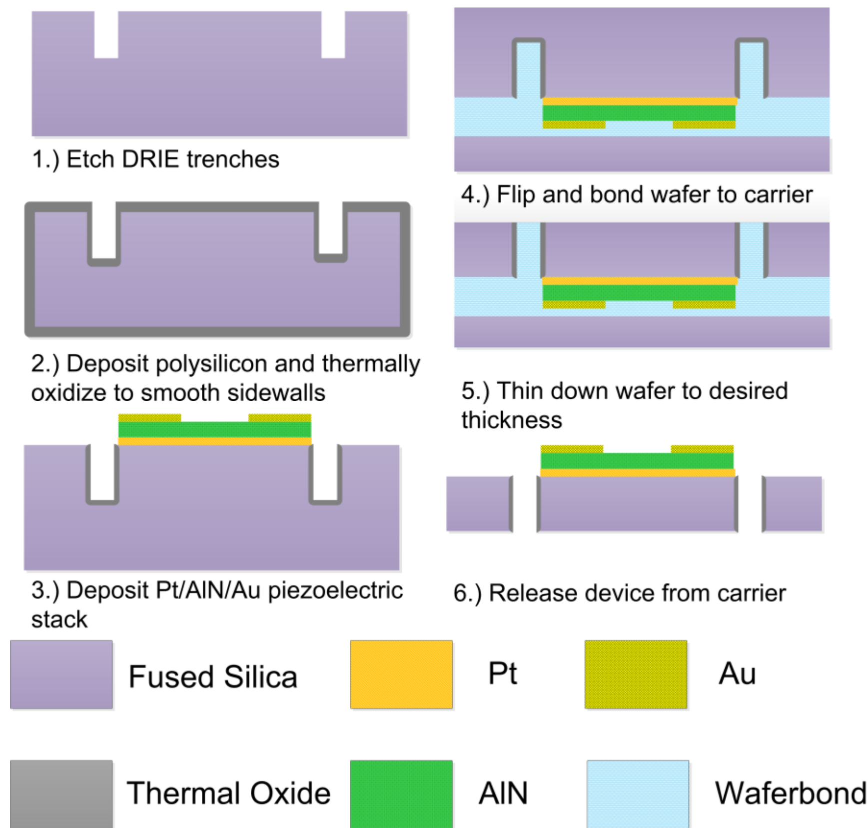

Fig. 3.6: Fabrication flow for the sidewall-smoothed AlN-on-silica resonators. This flow utilizes a fused silica DRIE-first approach to smooth sidewalls through thermal oxidation and etching of LPCVD polysilicon.

The fabrication flow for the sidewall-smoothed resonators has one major difference from the previous two processes in that the fused silica DRIE to define the resonator body is performed first. By performing the DRIE process first, furnace processing to assist with sidewall smoothing is a possibility. With the previously discussed fabrication flows, the piezoelectric stack added prior to the fused silica DRIE prevented high temperature processing necessary for furnace-based smoothing. The fabrication process for sidewall smoothing is outlined in Fig. 3.6. After the device

geometry is defined through a front-side fused silica DRIE, the wafer undergoes 5 minutes of buffered hydrofluoric acid (BHF) etching to etch back the largest of the striations caused by the DRIE. Next, 1 μm of conformal LPCVD polysilicon is deposited on the wafer to uniformly coat the sidewalls of the trench. Wet thermal oxidation is then performed at 1100 °C to oxidize 500 nm of the polysilicon into silicon dioxide, with the volumetric increase from oxidation partially planarizing the sidewall. A second BHF etch is performed to etch back the grown silicon dioxide to the remaining polysilicon and further smooth out the sidewall. This oxidation/etch process is repeated a second time for further smoothing and to remove a large portion of the deposited silicon dioxide. This oxidation/etch process is done in two parts to allow for two planarizing oxidation steps as well as to reduce stress buildup from thick oxidative growth and prevent mechanical damage to unsupported structures. Once the sidewall smoothing process is completed, the process flow continues as normal with piezoelectric stack deposition and patterning over the etched trenches. Extra care is required during the fabrication process to ensure that the etched trenches do not interfere with lithography steps, with many liftoff and etch steps requiring that the fused silica trenches be filled with photoresist to create a planarized surface. After the piezoelectric stack is deposited, the wafer is flipped, bonded, and thinned as normal. Due to the trenches being etched first, no DRIE step for final release is required post-thinning.

The effect of the sidewall smoothing process is shown in Fig. 3.7. The left SEM image shows an example sidewall of a test structure prior to the smoothing process, and the right SEM image shows the sidewall post-smoothing. There is a notable decrease in striations across the resonator, especially near the bottom of the trenches where the striations are the largest. Surface roughness measurements done on this sidewall using white light interferometry with a Zygo NewView 500 show a reduction in average surface roughness from 350 nm for the unsmoothed

sidewall to 165 nm for a sidewall post-smoothing. This is an almost two times reduction in surface roughness on these trenches versus unsmoothed sidewalls.

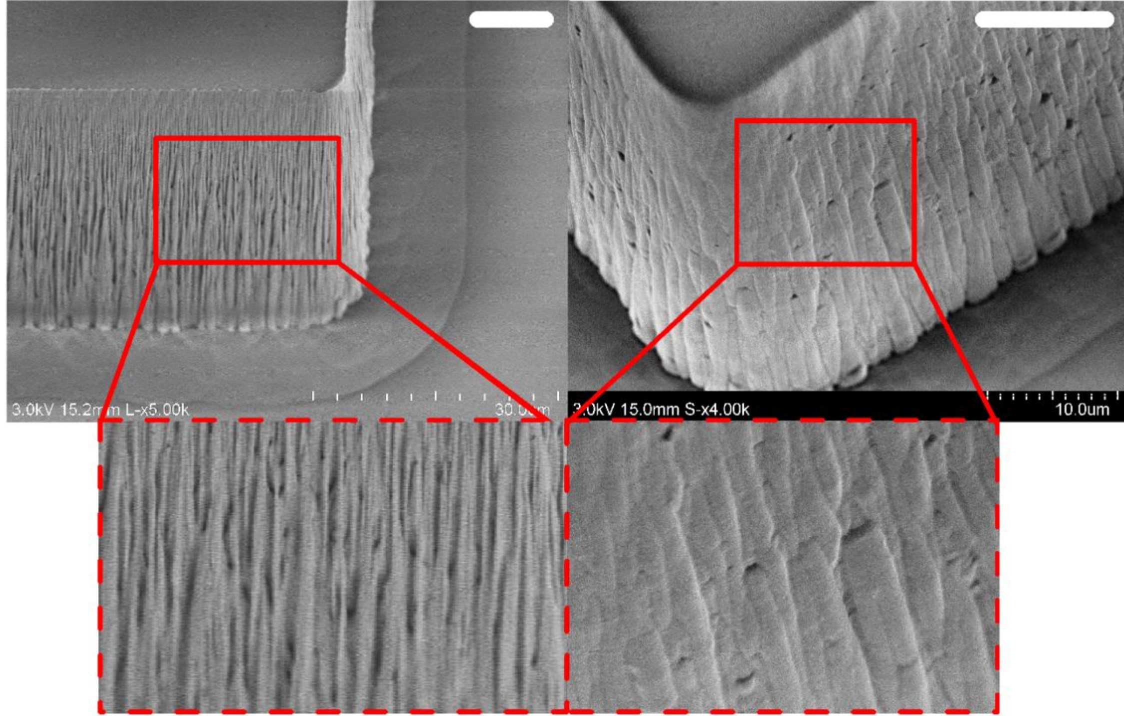

Fig. 3.7: SEM images of silica DRIE sidewalls pre (left) and post (right) sidewall smoothing with insets highlighting zoomed view of striations. Scale bars are 10 µm in length. Average sidewall roughness is measured to be reduced to 165 nm from 350 nm using this smoothing process.

The measured S-parameters of the sidewall smoothed AlN-on-silica resonators are shown in Fig. 3.8. The in-phase Q of the smoothed resonators is measured at around 17,500 with an insertion loss of 17.2 dB, which is very similar to that seen in normal AlN-on-silica resonators. The center frequency of the resonator is slightly higher than that seen in normal AlN-on-silica resonators due to the shrinking ring dimensions from the additional BHF etching. Critically, the measured performance of these devices does not show a notable improvement over previously measured results, eliminating surface losses from the resonator sidewall as the dominant loss mechanisms in these resonators.

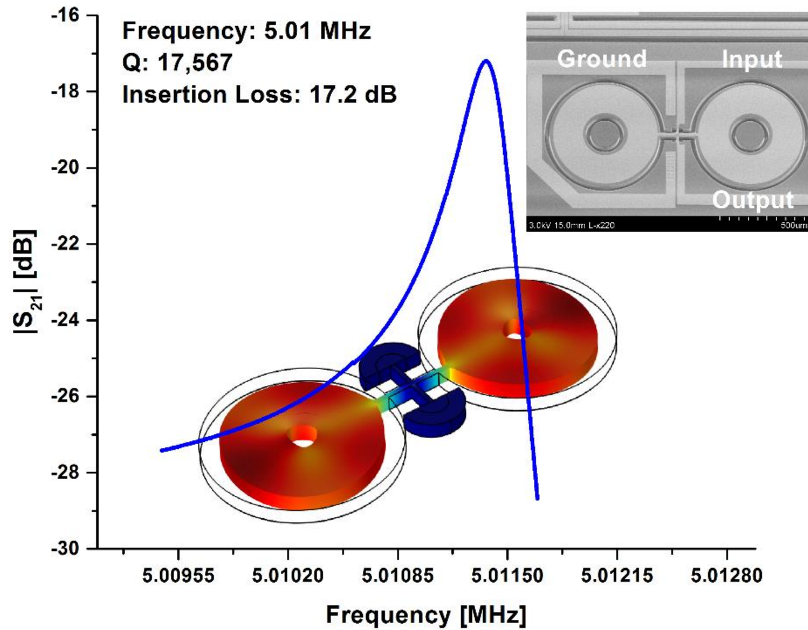

Fig. 3.8: Measured S-parameter response for an in-phase AlN-on-silica sidewall-smoothed resonator. Center frequency is measured at 5.01 MHz with a Q of 17,567 and an insertion loss of 17.2 dB. Inset shows a labeled SEM image of a fabricated resonator, while simulated mode shape is displayed in the background.

Alternate Loss Mechanisms in Fused Silica Resonators

A combination of simulations, analytical equations, and measured results has eliminated anchor losses, TED, and surface losses as dominant mechanisms in fused silica resonators. A summary of the experimental results is shown in Table 3.3. With these main sources of loss shown to not limit device performance, it is necessary to investigate alternative sources of loss in these resonators. Thin piezoelectric on substrate (TPoS) devices are designed to maximize the effect of the high-quality substrate while still maintaining the benefits of piezoelectric actuation. Despite this, the highest performance examples of piezoelectrically actuated resonators [10, 11] are still far behind the achieved performance of capacitively-actuated resonators [12-14]. Interface losses, caused by the interface between metal and piezoelectric layers, have been proposed to explain this difference [4, 15]. It has been proposed that this loss is caused by a stress jump between material layers caused by a difference in Young’s modulus. This creates an instantaneous stress jump,

which then creates a heat gradient that is dissipated as loss [4]. This loss can be partially mitigated by using techniques such as piezoelectric layer patterning [10] or by choosing piezoelectric materials that reduce the Young's modulus mismatch [15]. Interface loss can also be minimized by reducing the amount of layers in the piezoelectric stack, specifically the ground electrode [10]. Eliminating layers is not practical in fused silica, however, as the non-conductive nature of oxide require the use of a ground electrode to maintain an electric field across the piezoelectric layer. Further investigation is required to identify the effect of interface losses on these devices, potentially through optical interrogation methods to identify the effect of individual layers on device performance. With this noted, interface losses are expected to change as materials and Young's moduli change in the piezoelectric stack. If interface losses were dominant, PZT-on-silica devices would be expected to perform better than AlN-on-silica devices due to the smaller Young's modulus mismatch between PZT and fused silica, which does not hold. Despite this, interfaces losses are complex and the cause of this loss is not well understood. It is not possible to dismiss this loss mechanism outright, and future work will focus on investigating this loss mechanism as well as investigating new mechanisms.

Table 3.3

Summary of Measured Performance for Fabrication Piezoelectric-on-Silica Resonators

Device Type	Center Frequency	Measured Q
AlN-on-Silica	4.96 MHz	19,671
PZT-on-Silica	4.80 MHz	17,849
Sidewall-Smoothed AlN-on-Silica	5.01 MHz	17,567

A second source of loss that has not been investigated so far in piezoelectric devices is dielectric loss. This loss is caused by a non-ideal dielectric material which will dissipate some of the energy stored across the material as heat. The amount of this loss, typically characterized by

the loss tangent (δ), is frequency and material dependent and can be represented mathematically as the imaginary portion of the dielectric constant over the real portion of the dielectric constant. As the loss tangent of a material is sensitive to its crystalline grain size, purity, and deposition conditions it is necessary to measure the properties of the deposited film to get an accurate reading of the loss tangent. However, published parameters for similarly deposited common piezoelectric materials can be found and used as a rough estimate. From literature, it can be found that polycrystalline piezoelectric AlN at 5 MHz has a loss tangent around $8 \cdot 10^{-4}$ [16], whereas for sintered PZT a loss tangent of $9.1 \cdot 10^{-3}$ was reported at 5 MHz [17]. It is important to note, especially for the sintered PZT versus the sol-gel PZT used in the PZT-on-silica devices, that these are estimates and the exact values need to be extracted for the specific films to get accurate loss tangents. With the loss tangent values from literature, it is possible to simulate the dielectric loss for these resonators in COMSOL, giving an estimate of dielectric *Q*. For AlN-on-silica devices, the simulated dielectric *Q* is 470,341, and for the PZT-on-silica devices the dielectric *Q* was simulated at 41,180. Both of these simulated numbers put the total performance of these resonators above the measured results, but the PZT-on-silica devices do show a closer match between simulated and experimental *Q*s (38,298 simulated versus 17,849 measured). These results suggest that the PZT-on-silica devices may be limited or partially limited by dielectric loss, but additional measurements of the film are needed to confirm this hypothesis. Regardless, there is still a need to determine the dominating loss mechanism in AlN-on-silica devices, and therefore further investigation into other loss mechanisms is required.

Charge Redistribution Loss in Piezoelectric Resonators

One new loss mechanism is related to non-uniform strain profiles across piezoelectric films and is known as charge redistribution loss. Charge redistribution loss, which was first introduced

by Dr. Roozbeh Tabrizian in [18], is caused by the electrical resolution of a non-uniform charge profile across a metal-coated piezoelectric film, which is in turn caused by a non-uniform strain profile. The non-uniform charge works to resolve the charge gradient through redistribution through the metal electrodes on the piezoelectric film, with energy lost from the redistribution. The redistribution of charge in the metal-on-piezoelectric layer is an analogue to the distribution theory in a set of ideal charged capacitors. For the simplest case, assume two ideal capacitors separated by an ideal switch. Both capacitors have a capacitance C, but one capacitor has a charge Q stored across it while the other has zero charge. The total energy in the system can be written as [18]:

$$E_{capacitors} = \frac{Q^2}{C} + \frac{0^2}{C} = \frac{Q^2}{C} \qquad \text{(Equation 3.4)}$$

When this ideal switch is closed, the charge between the two capacitors will redistribute and equalize, with both caps holding a charge of ½ Q. Now the total energy in the system is:

$$E_{capacitors} = \frac{\left(\frac{1}{2}Q\right)^2}{C} + \frac{\left(\frac{1}{2}Q\right)^2}{C} = \frac{Q^2}{2C} \qquad \text{(Equation 3.5)}$$

It can be seen that the energy after distribution is only ½ of the initial energy in the system, despite the presence of ideal components. This energy loss is proposed to be caused by electron to photon conversion, directly radiating this energy off as electromagnetic radiation in the THz range [19]. This example belies a similar behavior in piezoelectric resonators, where the strain profile will oscillate from a maximum strain point through a zero strain “rest point” to an opposite negative maximum strain point. This cycle contains two separate redistribution cycles as the charge in the top metal layer follows the strain profile from maximum to minimum and back again. A graphical example of this process is shown in Fig. 3.9, where a width extensional resonator is brought

through a single harmonic cycle. The cycle begins at t=0 at its maximum strain point where the resonator in contracted inwards. The motional charge is maximum in the center of the resonator, and as the device expands it reaches a zero point of charge at $t = \frac{T}{4}$, where T is the period of oscillation. Over this time period the charge on the metal electrodes has redistributed as the motional charge forcing their distribution is removed and completing one loss cycle. The cycle then continues with maximum resonator expansion, and again cycles back through the zero point at t=$\frac{3T}{4}$. Overall, the loss from these two cycles can be analytically modeled for a generic piezoelectric resonator as [18]:

$$Q_{Redistribution} = 2\pi \frac{Maximum\ energy\ stored\ in\ the\ system}{Energy\ dissipated\ per\ cycle} = 2\pi \frac{(E_{Strain}+E_{Charge})}{E_{Diss}} \quad \text{(Equation 3.6)}$$

where:

$$E_{Diss} = 2 \times \left\{ A \oiint_A \frac{(q_{motional}(x,y,0))^2}{2C_0} dA - \frac{\left(\oiint_A q_{motional}(x,y,0) dA\right)^2}{2C_0} \right\} \quad \text{(Equation 3.7a)}$$

$$E_{Strain} = \oiiint_{Resonator\ Body} S(x,y,0) \cdot \sigma(x,y,z,0)\, \partial V \quad \text{(Equation 3.7b)}$$

$$E_{Charge} = \oiint_A \frac{(q_{motional}(x,y,0))^2}{2C_0} \partial A \quad \text{(Equation 3.7c)}$$

For these equations, E_{Diss} is the dissipated energy per cycle, E_{Strain} is the total strain energy in the system, E_{Charge} is the total charge energy stored in the piezoelectric layer, $q_{motional}$ is the motional charge across the piezoelectric layer, C_0 is the capacitance of the film in the electrode area, A is the area of the electrode region, S is the strain field, and σ is the stress field. A full derivation of this equation and a more in-depth discussion of this theory can be found in [18].

Modeling of Charge Redistribution Loss

In Eq. 3.6 and 3.7, an analytical model of charge redistribution in a resonator is presented. This method can be extended to predict the loss in any arbitrary piezoelectric resonator, such as the AlN- or PZT-on-silica resonators. A number of assumptions are made to simplify the

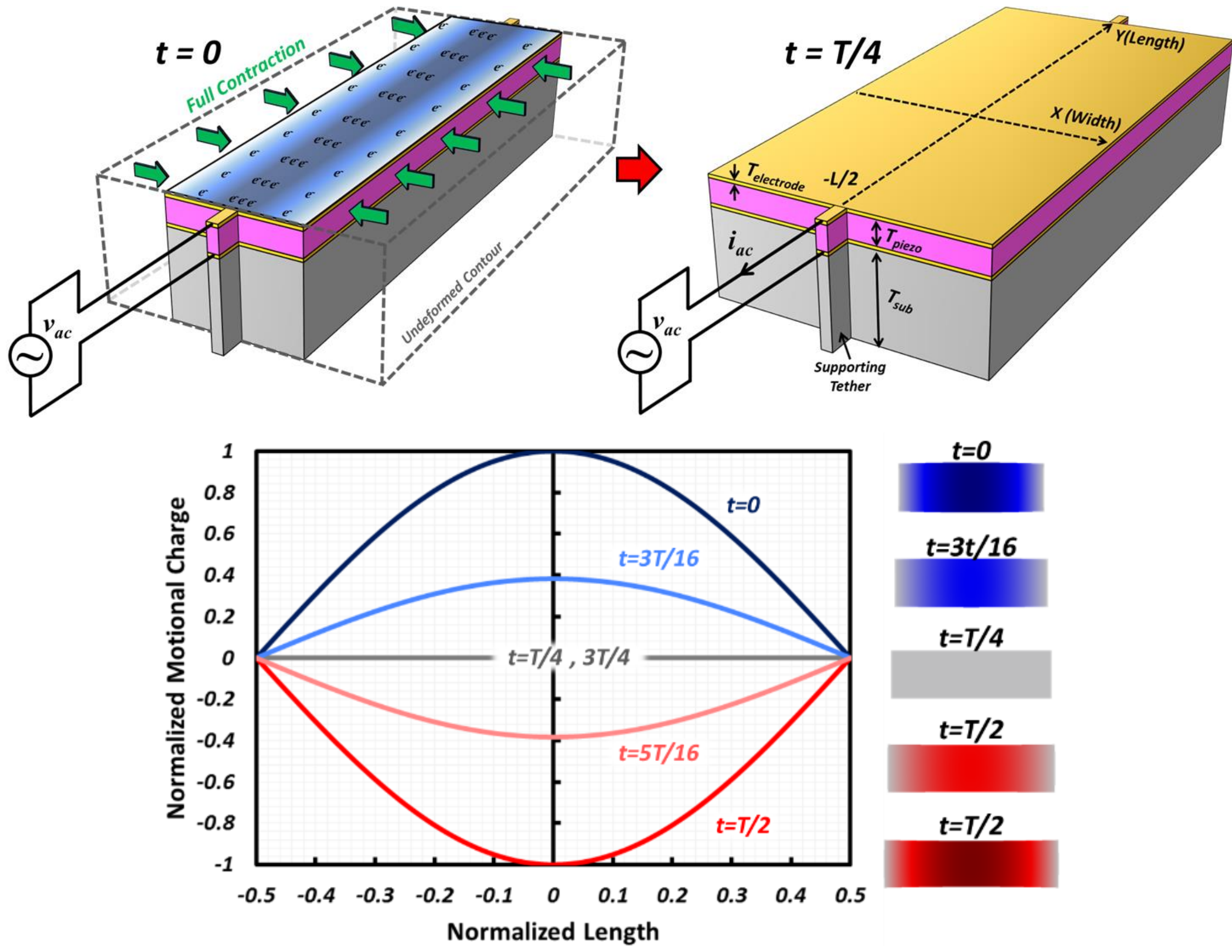

Fig. 3.9: (Top) A schematic outlining the charge redistribution concept for a one-port piezoelectric resonator. The width extensional mode of a resonator is actuated through a piezoelectric stack on a TPoS structure. Time t=0 is chosen to be the point of full device contraction. (Bottom) A graphical representation of the motional charge created by the piezoelectric layer during a harmonic cycle. A cross-sectional cut of the resonator width is shown, with cross-sectional mode shapes shown at each time point. Figures adapted from [19].

modeling process for the dogbone resonators. The first assumption is that the z-directional strain of the dogbone resonators are zero, as the radial extensional mode is strictly in-plane. A second assumption is that each ring has uniform strain across all azimuthal angles. Combining these two assumptions allows for a one-dimensional line to accurately represent the radial strain gradient of

a dogbone ring. Extracting the COMSOL-simulated strain profile from a 1D line and applying Eq. 3.6 and 3.7 allow an estimate of the expected loss due to charge redistribution. The results of these simulations can be seen in Fig. 3.10, where the directional strain had been plotted for both AlN- and PZT-on-silica resonators. The analytical charge redistribution Q (Q_{CR}) for both piezoelectric materials are included as well, with the AlN devices showing a Q_{CR} of 37,714 and the PZT devices showing a Q_{CR} of 20,686. The PZT-on-silica devices have a lower Q_{CR} due to its higher electromechanical coupling, which leads to a higher motional charge and therefore larger redistribution losses. When these results are combined with the simulated Q_{anchor} and Q_{TED} results, the total simulated Q for each piezoelectric film can be predicted, as shown in Table 3.4.

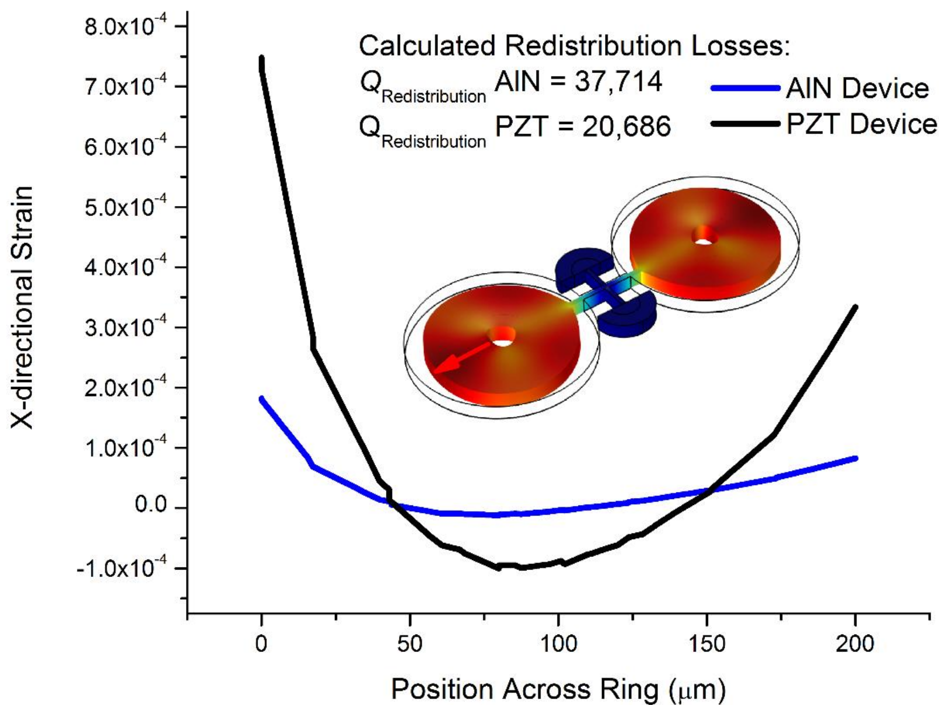

Fig. 3.10: Simulated X-directional strain profile for an AlN- and PZT-on-silica dogbone resonator. The non-uniform strain gradient causes a non-uniform charge gradient which redistributes during the harmonic cycle, causing loss. Differences in loss between the AlN- and PZT-on-silica are due to the larger electromechanical coupling coefficient of PZT over AlN, causing larger motional charge gradients. Insert shows simulated mode shape with labeled direction of plotted X-directional strain.

The results of Table 3.4 show that the total simulated Q differs from the measured results by 20%, which relates favorably to the multiple order of magnitude difference shown for the other

losses outlined above. These results suggest that charge redistribution may be partially or fully limiting the device performance of these fused silica resonator. From this analytical study, potential mitigation methods can begin to be gleaned. One of the best ways to mitigate this loss would be through shrinking the top electrode area. By designing electrodes to minimize motional charge gradients under them, the redistribution loss can be minimized, although at the cost of insertion loss due to lower motional charge pickup. Given the simulation results including the proposed charge redistribution loss, experimental verification of this loss is required to verify theory and confirm that charge redistribution is limiting the device performance of these AlN-on-silica resonators.

Table 3.4

Combined Simulation Results of Multiple Loss Mechanisms for Piezoelectric-on-Silica Resonators

	AlN-on-Silica	***PZT-on-Silica***
Simulated Frequency (MHz)	**5.03**	**4.78**
Simulated Q_{TED}	**7.49×10^4**	**1.11×10^7**
Simulated Q_{anchor}	**1.2×10^6**	**1.2×10^6**
Simulated Q_{CR}	**3.77×10^4**	**2.07×10^4**
Total Simulated Q	**2.51×10^4**	**2.02×10^4**

Experimental Verification of Charge Redistribution Loss

With a theory of charge redistribution proposed, experimental verification of this loss mechanism is necessary to confirm the trends outlined above. Verification of this theory can be done through the use of thin piezoelectric-on-substrate (TPoS) devices with different electrode layers, covering a range of mode shapes and frequencies. To this end, a simple AlN-on-silicon prototype was designed with three different mode types: length extensional, dogbone radial extensional, and flexural. All of these modes have different strain profiles across their geometry, testing a variety of charge gradients against expected theory. Similarly, as charge redistribution

theory is frequency-independent, utilizing a range of different frequencies will allow for further verification. The flexural mode is designed to operate at 1 MHz, and the length extensional and radial extensional modes are designed to operate at 10 MHz. A schematic of these three designs is shown in Fig. 3.11, with each device having the same material stack.

Experimental determination of charge redistribution loss needs to separate the expected loss from other common mechanisms, such as interface losses, metal loading, and TED. In order to best separate these, three different electrode variations are designed. To address TED, device measurements will be done at room temperature (300 K) and at low temperatures (100 K). As TED is proportional to temperature, lower temperature will provide higher expected Q_{TED} and therefore allow for shifts in Q_{CR} to be measured.

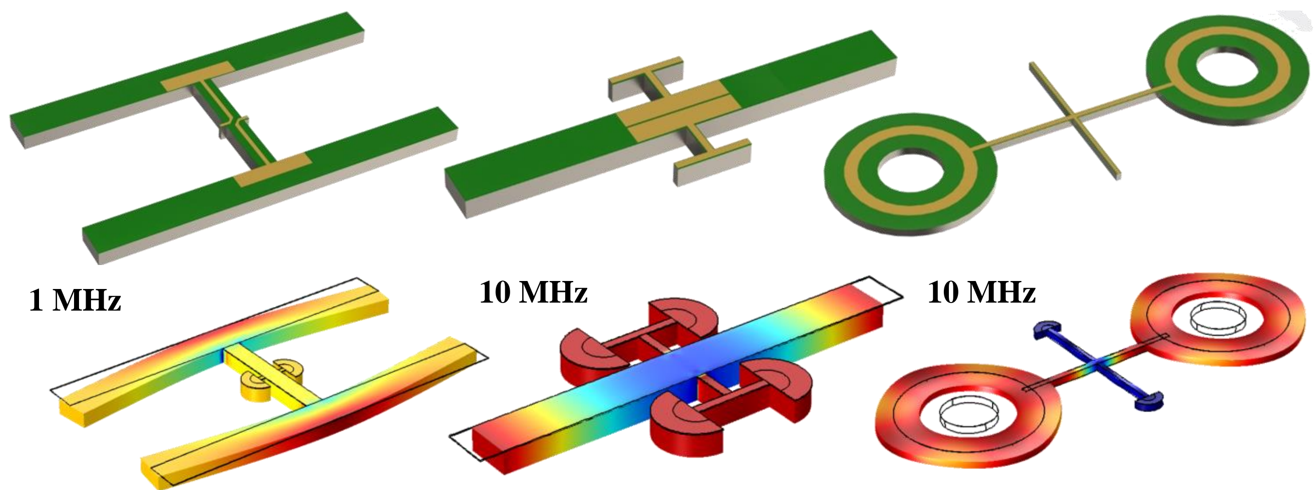

Fig. 3.11: Schematic and simulated strain profile for each of the three charge redistribution designs. (Left) A dual-tined flexural mode creates a strain gradient near the center coupling beam. The designed mode has a resonance frequency of 1 MHz (Middle) A length extensional mode with a resonance frequency of 10 MHz. The strain profile of these resonators is maximum at the center and tapers off toward the edge. (Right) A dogbone resonator in the fundamental radial-extensional mode at 10 MHz. The strain profile of these devices is relatively uniform across its length, but slowly decreases from inner to outer radius.

The first electrode variation is simple, involving the charge gradient contained under the metal electrode. As noted in the previous section the larger gradient covered by the electrode, the more charge redistribution is expected to occur. This can be tested with three variations, a base variation with a small electrode area, a variation with moderate coverage, and a variation with

maximum metal coverage. As the coverage increases, the measured Q_{CR} should decrease. The base variation is identical to that shown in Fig 3.11, while the medium and large coverage variations are shown for each device in Fig 3.12.

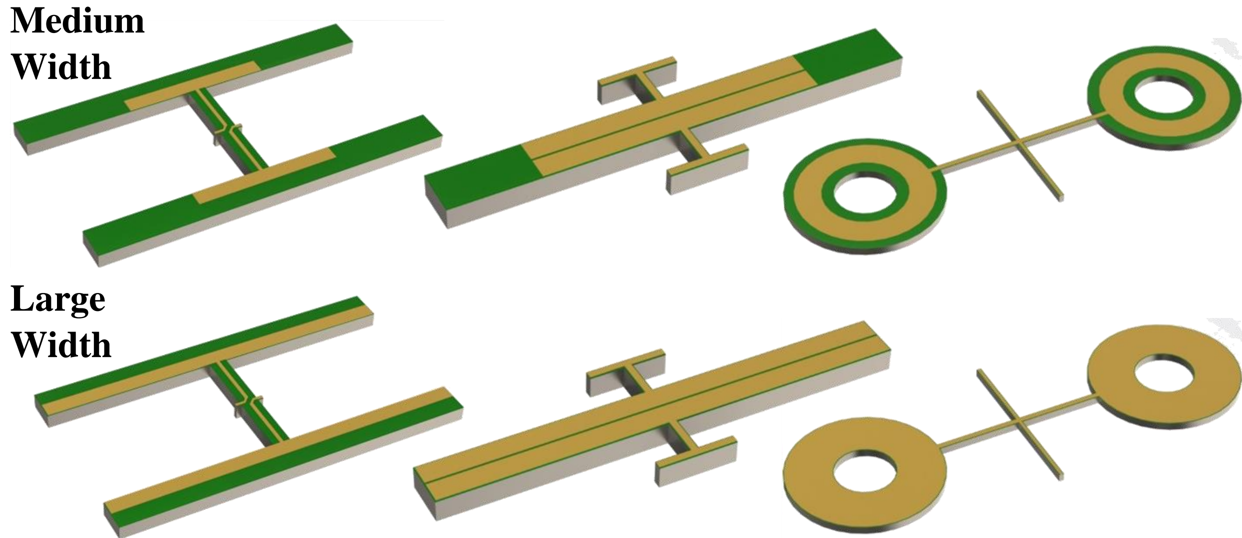

Fig. 3.12: Schematic of designs for total coverage variations. The base design, shown in Fig. 3.11, has the least electrode coverage with these two variations showing more top metal coverage. It is expected that these devices show lower Q_{CR} as compared to the base designs.

The designs shown in Fig 3.12 would also change the metal loading of the device due to differences in metal coverage. To address this, a second electrode variation that has identical metal area but a larger charge gradient is designed, known as an equivalent area design. This design should show lower Q due to the increased charge redistribution loss while maintaining identical metal area, and therefore loading, to a reference device. In general, these devices have thinner electrodes covering a wider gradient as opposed to the base variation. A schematic showing these variations are shown in Fig 3.13, with the variations expected to provide lower Q_{CR} as compared to the base design.

As in the equivalent area designs, a difference in coupled charge across the piezoelectric layer could skew the effects of charge redistribution, as the k_t^2 of the resonator depends directly on total coupled charge. To address this concern, a variation is designed that captures an identical

amount of charge as the base variation but across a larger charge gradient. As in the equivalent area design, the increased charge gradient of the equivalent k_t^2 designs, shown in Fig. 3.14, should lower Q as compared to a reference design. The dogbone designs, due to their relatively low change in charge gradient, cannot be designed to compare against the base designs shown in Fig. 3.11. Instead, two designs were made to compare against each other, with the top electrode design that covers less area expected to perform better.

All three of these variations can address various alternate loss mechanisms that would act in a similar manner to charge redistribution loss. By fabricating these variations, the effect of charge redistribution theory can be determined outside of other potential loss mechanisms.

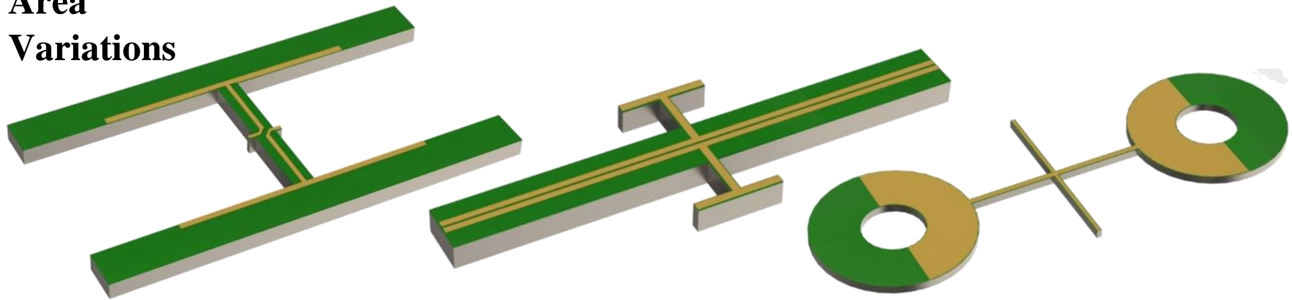

Fig. 3.13: Schematic of designs for equivalent area variations. Each design has equivalent area to the base design in Fig. 3.11 but covers a wider strain gradient on the device. It is expected that these devices show lower Q_{CR} as compared to the base designs.

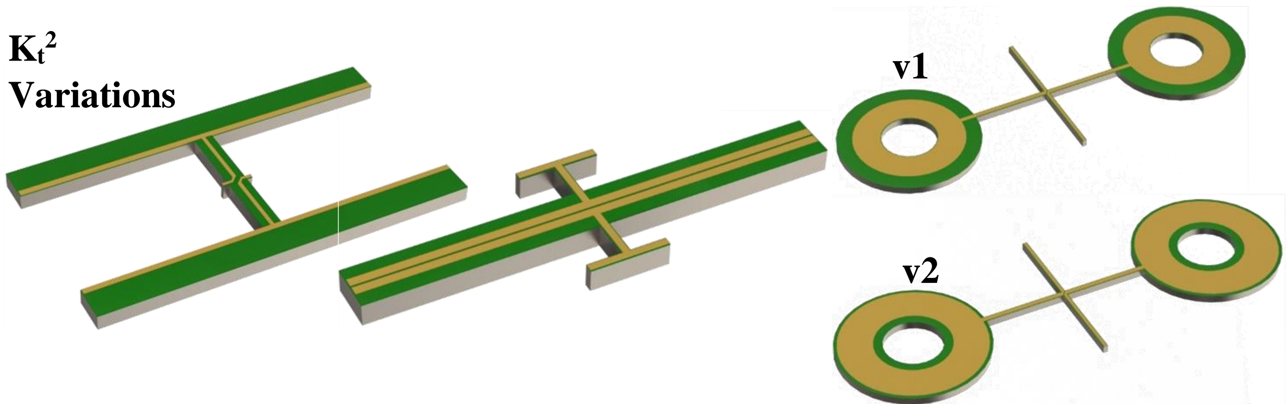

Fig. 3.14: Schematic of designs for equivalent k_t^2 variations. Each design has the same amount of motional charge under the electrodes as the base design shown in Fig. 3.11, but covers a much wider gradient. It is expected that these devices show lower Q_{CR} as compared to the base designs. Due to the relatively low gradient seen in the dogbone devices on the right, it was not possible to compare the equivalent K_t^2 design to the base. Instead, the two designs compare directly against each other.

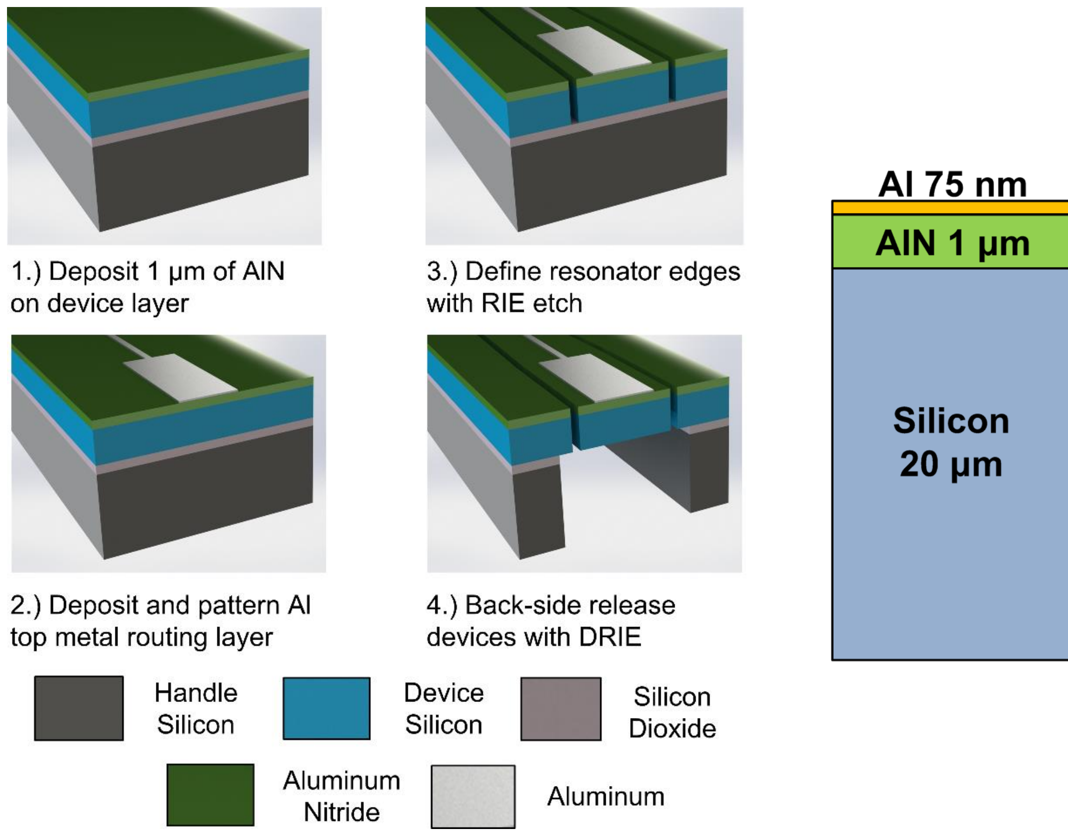

Fig. 3.15: Fabrication flow of the charge redistribution devices with schematic showing cross-section details. The devices have a highly doped 20 μm substrate layer with 1 μm of AlN and 75 nm of Al for metal routing. No ground layer is required due to the low resistivity of the silicon substrate, reducing potential interface losses.

Measurement of Charge Redistribution Variations

The fabrication of these devices follows a traditional fabrication flow for piezoelectric-on-silicon devices, except for the use of a highly doped silicon layer which negates the need for a bottom electrode layer. A more detailed discussion of this process is discussed in detail in Chapter 5, but the fabrication flow with cross section dimensions can be seen in Fig. 3.15. In this design, the silicon layer is 20 μm thick, the AlN layer is 1 μm thick, and the top metal Al layer is 75 nm.

The charge redistribution devices are measured in vacuum at two temperature points, 300 K and 100 K. The S-parameters of the designed mode at each variation are then measured and the total Q is extracted. This extracted Q is the total Q of the system, including all losses from the sources discussed earlier in this chapter. In order to predict the effect of charge redistribution, the

Q is also simulated for each variation, taking into account TED, anchor, and charge redistribution losses. Because the charge redistribution is designed to be the dominant loss mechanism in these variations, any measured change in Q is expected to be caused by the predicted trends.

The simulated charge redistribution of the designed devices shown in Fig. 3.11-3.14 were simulated using the same method outlined for the dogbone resonators in the previous section. Each design assumes a constant z-direction strain and a uniform y-directional strain, allowing for a 1D strain line to represent the strain field across the resonator. This assumption holds well for the dogbone and length extensional resonators, but requires some small tweaks for the flexural devices. The flexural device charge redistribution is instead calculated using three separate 1D lines of equal widths, averaging the strain across its gradient in order to provide a more accurate picture of the strain profile. These results are tabulated and compared against measured results, with the results presented in Tables 3.5-3.7 for each mode.

These results do not immediately confirm the expected charge redistribution trends, but do contain interesting point worthy of further discussion. First, it is important to note that these results can not properly control for interface loss. There are two different interfaces affecting this device stack, the Si/AlN interface and the AlN/Al interface. These are two points where additional energy loss can occur and interfere with the charge redistribution experiment. In order to properly control for this, optical measurements on a dummy device with each individual layer deposited should be measured to identify the effects of each layer on the stack. It is expected that the addition of another interface will decrease the loss in these devices, but it is unknown to what amount. Even in these cases, the conductive silicon layer could serve as an electrode for charge redistribution loss when optically excited and measured, introducing some loss on top of the expected interface loss. This further confuses the measured results, but could be addressed through the use of an AlN-on-silica

structure. The electrically isolating nature of fused silica would prevent charge redistribution loss for AlN-on-silica stacks and allow for a more accurate interface loss reading. Similarly, a thin oxide layer can be added between the silicon and AlN layers on the presented devices to buffer this effect and give cleaner results.

Table 3.5

Measured and Simulated Performance Results for Flexural Charge Redistribution Resonators

Variation	300 K Measured Q	100 K Measured Q	Simulated Q_{CR}	Simulated Q_{Total} (100 K)	Simulated Q_{Total} (300 K)
Flexural Base	24,742	38,119	456,870	104,086	43,761
Flexural Medium	23,573	31,150	115,250	62,138	34,086
Flexural Large	21,557	28,355	13,158	11,988	10,345
Flexural Equivalent Area	20,470	36,161	137,840	68,150	35,820
Flexural Equivalent K_t^2	22,380	26,194	7,906	7,468	6,796

Table 3.6

Measured and Simulated Performance Results for Dogbone Charge Redistribution Resonators

Variation	300 K Measured Q	100 K Measured Q	Simulated Q_{CR}	Simulated Q_{Total} (100 K)	Simulated Q_{Total} (300 K)
Dogbone Small	15,503	44,206	770,010	143,730	90,940
Dogbone Base	9,312	18,970	83,135	56,537	46,028
Dogbone Large	7,229	12,055	12,816	11,949	11,399
Dogbone Equivalent Area	12,413	23,860	25,625	22,380	20,525
Dogbone Equivalent K_t^2 V1	8,729	16,598	25,217	22,068	20,262
Dogbone Equivalent K_t^2 V2	8,239	12,634	62,724	46,303	39,001

Table 3.7

Measured and Simulated Performance Results for Length Extensional Charge Redistribution Resonators

Variation	300 K Measured Q	100 K Measured Q	Simulated Q_{CR}	Simulated Q_{Total} (100 K)	Simulated Q_{Total} (300 K)
LE Base	23,534	72,830	9,479,731	199,264	73,080
LE Medium	22,109	58,056	64,937	49,231	34,509
LE Large	20,215	54,254	6,320	6,130	5,821
LE Equivalent Area	25,192	73,012	24,639	21,979	18,462
LE Equivalent K_t^2	24,528	57,946	15,401	14,318	12,737

While interface losses cannot be completed removed from these measurements, it is still worthwhile to notice some trends in the data. Firstly, the 300 K measurements appear to all be at least partially limited by TED. The variation and overall Q of these devices are substantially lowered, which follows expected trends with multilayer devices as noted earlier in this chapter. Lower temperature results begin to show stronger effects from electrode variations, suggesting that Q_{TED} is no longer as significant a factor. Next, for all device types the total coverage variations follow the expected charge redistribution loss trends. Decreasing Q is seen between the small, medium, and large electrodes, although not at the levels simulated using the 1D method. Interestingly, the equivalent area and equivalent K_t^2 designs show opposite results to the simulations, roughly following the trends based on electrode coverage as opposed to gradients. For example, the equivalent area designs show similar results to the base designs at low temperatures, suggesting that interface loss may be affecting these variations more than any charge redistribution losses.

Another potential explanation for the apparently small effect of charge redistribution in these devices may have to do with the layout of the charge gradient. For all of the devices presented here, the highest charge density lies near the tether points of the device's significant area. In an electrical measurement, there is tendency for any motional charge created the electrodes to follow the path of least resistance towards the input and output ports, now a source or ground due to the electrical actuation and readout. This would prevent a large amount of charge redistribution, especially in one directional gradients like the length extensional modes. Therefore, it would be expected to see more losses in higher order modes, where gradient resolution and the path of least resistance can exist simultaneously.

Both of these theories can be further explored through a more in-depth investigation of interface losses on these devices. This can be achieved through optical excitation and interrogation of these and a number of dummy devices in order to better understand the effect of each layer. As mentioned above, utilizing AlN-on-silica structures or isolating the ground electrode from the substrate would also help decouple interfaces losses from charge redistribution. Because of this difficultly in decoupling these two losses, it is still too early to verify charge redistribution loss in piezoelectric resonators, and more work is required.

References

[1] D. B. Leeson, "A simple model of feedback oscillator noise spectrum," *Proc. IEEE,* vol. 54, pp. 329-330, Dec., 1966.

[2] C. Zener, "Internal friction in solids. I: theory of internal friction in reeds," *Physical Review,* vol. 52, pp. 230-235, 1937.

[3] Z. Nourmohammadi, S. Prabhakar and S. Vengallatore, "Thermoelastic damping in layered microresonators: critical frequencies, peak values, and rule of mixture," *J. Microelectromech. Syst.,* vol. 22, pp. 747-754, June, 2013.

[4] A. Frangi, M. Cremonesi, A. Jaakkola and T. Pensala, "Analysis of anchor and interface losses in piezoelectric MEMS resonators," *Sensors and Actuators A: Physical,* vol. 190, pp. 127-135, Feb., 2013.

[5] H. Nazeer, M. D. Nguyen, L. A. Woldering, L. Abelmann, G. Rijnders and M. C. Elwenspoek, "Determination of the Young's modulus of pulsed laser deposited epitaxial PZT thin films," *J. Micromech. Microengineering,* vol. 21, pp. 074008, June, 2011.

[6] (October 19, 2014). *PZT5A & 5H Materials Technical Data*. Available: http://www.ctscorp.com/components/pzt/downloads/PZT_5Aand5H.pdf.

[7] A. Duwel, R. N. Candler, T. W. Kenny and M. Varghese, "Engineering MEMS resonators with low thermoelastic damping," *J. Microelectromech. Syst.,* vol. 15, pp. 1437-1445, Dec., 2006.

[8] G. L. Smith, J. S. Pulskamp, L. M. Sanchez, D. M. Potrepka, R. M. Proie, T. G. Ivanov, R. Q. Rudy, W. D. Nothwang, S. S. Bedair, C. D. Meyer, R. G. Polcawich and D. J. Green, "PZT-based piezoelectric MEMS technology," *J. Am. Ceram. Soc.,* vol. 95, pp. 1777-1792, Apr., 2012.

[9] B. Shiari and K. Najafi, "Surface effect influence on the quality factor of microresonators," in *Proceedings of the 17th International Conference on Solid-State Sensors, Actuators and Microsystems (TRANSDUCERS & EUROSENSORS),* 2013, pp. 1715-1718.

[10] W. Pan and F. Ayazi, "Thin-film piezoelectric-on-substrate resonators with Q enhancement and TCF reduction," in *Proceedings of the 23rd IEEE International Conference on Micro Electro Mechanical Systems (MEMS),* Wanchai, Hong Kong, 2010, pp. 727-730.

[11] V. Thakar and M. Rais-Zadeh, "Temperature-compensated piezoelectrically actuated lamé-mode resonators," in *Proceedings of the 27th IEEE International Conference on Micro Electro Mechanical Systems (MEMS),* San Francisco, CA, USA, 2014, pp. 214-217.

[12] L. Khine, M. Palaniapan and W. Wong, "6MHz bulk-mode resonator with Q values exceeding one million," in *Proceedings of the International Solid-State Sensors, Actuators and Microsystems Conference (TRANSDUCERS & EUROSENSORS),* Lyon, France, 2007, pp. 2445-2448.

[13] Yu-Wei Lin, Seungbae Lee, Sheng-Shian Li, Yuan Xie, Zeying Ren and C. T. -. Nguyen, "Series-resonant VHF micromechanical resonator reference oscillators," *IEEE J. Solid State Circuits,* vol. 39, pp. 2477-2491, Dec., 2004.

[14] V. Kaajakari, T. Mattila, A. Oja, J. Kiihamaki and H. Seppa, "Square-extensional mode single-crystal silicon micromechanical resonator for low-phase-noise oscillator applications," *IEEE Electron Device Lett.,* vol. 25, pp. 173-175, Apr., 2004.

[15] J. Segovia-Fernandez and G. Piazza, "Damping in 1 GHz laterally-vibrating composite piezoelectric resonators," in *Proceedings of the 28th IEEE International Conference on Micro Electro Mechanical Systems (MEMS),* Estoril, Portugal, 2015, pp. 1000-1003.

[16] M. González and A. Ibarra, "The dielectric behaviour of commercial polycrystalline aluminium nitride," *Diamond and Related Materials,* vol. 9, pp. 467-471, May, 2000.

[17] L. Jin, "Broadband dielectric response in hard and soft PZT: Understanding softening and hardening mechanisms," 2011.

[18] R. Tabrizian and M. Rais-Zadeh, "The effect of charge redistribution on limiting the kt2.Q product of piezoelectrically transduced resonators," in *Proceedings of the 18th International Conference on Solid-State Sensors, Actuators and Microsystems (TRANSDUCERS & EUROSENSORS),* Anchorage, AK, USA, 2015, pp. 981-984.

[19] T. B. Boykin, D. Hite and N. Singh. The two-capacitor problem with radiation. *American Journal of Physics 70(4),* pp. 415-420. 2002.

Chapter 4: Temperature Compensation of Fused Silica

As noted in Chapter 1, the natural TCF of fused silica is measured to be as high as 90 ppm/K [1], which is almost three times larger than the TCF of uncompensated silicon at -32 ppm/K [2]. This large temperature instability needs to be addressed in order to maximize stability of the final timing reference, as any shift in the resonator frequency will lead to a drift in the final output frequency of the timing system. Traditionally there are a number of methods of addressing temperature instability in resonators, and a number of published works addressing this for silicon resonators [3-5]. The most popular solutions for silicon include passive compensation through material compensation [4] and doping [5] and active methods of compensation such as circuit level compensation [6] or ovenization [7, 8]. Both methods have advantages for resonator stability, and both will be utilized in fused silica to achieve temperature compensation.

Active Temperature Compensation

Of the active temperature compensation methods, ovenization is one of the most common ways to achieve maximum stability. Oven-controlled timing references provide extremely stable performance by maintaining a constant temperature for resonator operation, effectively buffering any environmental effects from the body of the resonator. This has been implemented in commercial quart crystal oscillators, achieving some of the best performance and stability for miniaturized timing references at a cost of higher space and power [9]. A typical ovenized resonator is composed of three separate parts, a temperature sensor, a resonator used as the timing reference, and a heating element, typically a metal strip heated through joule heating. The

temperature sensor can take many different forms, such as an off-chip thermistor, a separate temperature sensitive resonator [10], or resistance temperature detectors (RTDs) that uses shifts in resistance to detect temperature changes [7, 11]. These RTDs can be placed directly on chip or potentially on the resonator to sense temperature changes in the metal [12]. Most applications use a RTD of some sort to minimize device size and keep the detector as close to the device as possible.

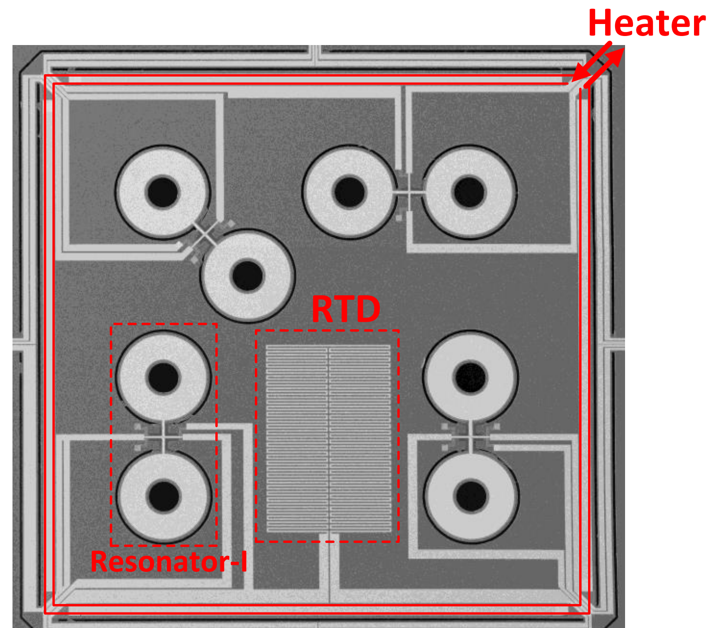

Fig. 4.1: SEM image of a fabricated fused silica ovenized platform. The platform is isolated from the substrate with long, thin isolation beams and heated through the use of a thin metal heating strip along the outside edge of the platform. An RTD in the center of the platform acts as the temperature sensor, while the reference resonator provides the timing signal. Image adapted from [13].

For fused silica, ovenization is particularly attractive due the large TCE of the material. Rather than needing to fully address the temperature-based frequency drift through electrical or passive methods, the overall temperature change in the device can instead be minimized. To implement this on fused silica, a generic platform structure was designed and implemented [13]. This platform uses the large thermal resistance of fused silica to keep heat confined, a thin platinum heating element around the edges, and a platinum RTD to measure platform temperature. This RTD is set in a feedback loop to maintain the platform temperature at a set value, providing a stable environment for resonator operation. A SEM image of the fabricated platform, using the

AlN-on-silica fabrication process, is shown in Fig. 4.1. Using this platform with a resistance-based feedback system, temperature stability was decreased from over 12,000 ppm over a -40 °C to 65 °C temperature range to just 10 ppm across the same range. An in-depth discussion of the design, results, and implementation of this thermal platform can be found in the works of Dr. Zhengzheng Wu [13-15].

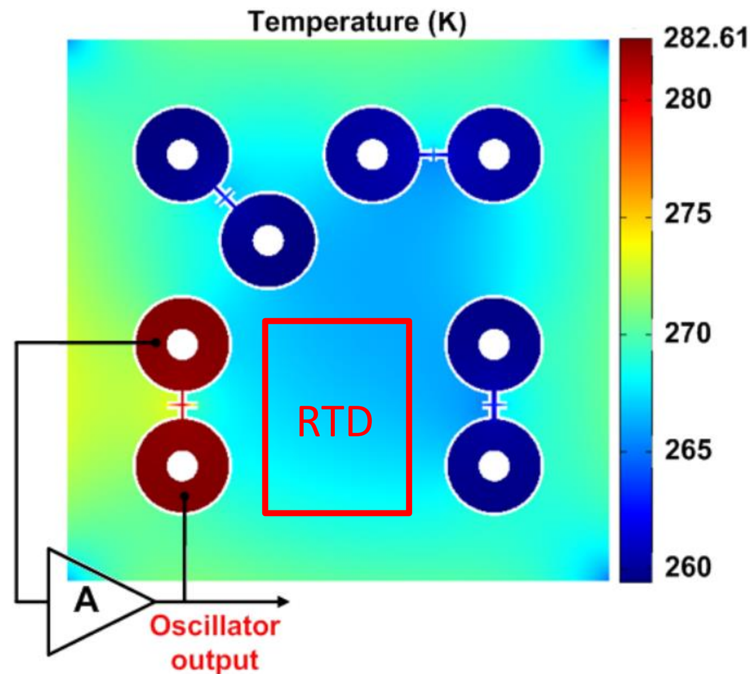

Fig. 4.2: Simulated COMSOL temperature distribution of a fused silicon ovenized platform. The outside temperature is set at 233K, the platform is heated with 4.3 mW of driving power through the heating strip, and the resonator is driven under 40 µW of oscillation power. The large temperature difference between the RTD and the resonator body is caused by the driving power and large thermal resistance of the dogbone tethers. Image is adapted from [13].

The major downside of this ovenization method was residual temperature error between the RTD temperature sensor and resonator itself [14]. The large thermal resistance in the small dogbone tethers as well as the power necessary to drive the timing reference makes for a large temperature differential between the resonator and what the RTD is sensing. This effect can be seen in the COMSOL temperature simulation in Fig. 4.2, where an ovenized platform with 4.3 mW of heating power is simulated with a resonator under 400 µW of driving power for oscillation at an outside temperature of 233 K [13]. This simulation shows the almost 20 K temperature differential present between the resonator and RTD, creating a temperature error in the feedback

loop. There are multiple methods of addressing this error, from calibration [13], to RTD placement [7], to a separate resonant temperature sensor with a similar geometry [8]. In all these solutions, some residual error, on the order of ppm over a typical temperature range, remains due to this thermal gradient between the sensor and device. In order to fully mitigate this error and work towards part-per-billion frequency stability, alternate methods need to be considered.

Due to this residual temperature gradients, ovenization alone is not sufficient to achieve the desired levels of stability. It is necessary to combine multiple methods of temperature compensation to mitigate the large TCE of fused silica. An additional mitigation method involves reducing the TCE of fused silica through passive temperature compensation, therefore making the entire device less sensitive to any error introduced during the ovenization process.

Passive Temperature Compensation in Fused Silica

In order to passively correct for temperature sensitivity, it is required to address the fundamental shift in material properties with temperature. All materials exhibit a shift in Young's modulus over temperature, which is measured by a material's TCE. As materials can have widely varying TCEs, one method of compensation is to combine two materials with opposite TCEs together in specific ratios to cancel out the overall shift. For example, silicon has a negative TCE of approximately -64 ppm/K [2], while SiO_2 has a TCE around +180 ppm/K [1]. By combining these two materials together in appropriate ratios it is possible to cancel out shifts in elasticity, effectively eliminating the first-order effects of TCF [16]. This has been achieved in silicon resonators through blanket deposition or growth of SiO_2 [16], as well as resonators with a regular field of "pillars" through the resonator body, providing compensation through a silicon-silicon dioxide composite structure [17]. As both of these methods involve the addition of an alternate material into the resonator body, a decrease in device Q can be observed [3]. In order to minimize

this performance loss, an alternate method was developed that involves placing compensation material in regions of maximum strain. This method utilizes the fact that regions of high strain are more sensitive to shifts in material parameters, causing maximum temperature compensation in a minimal volume [3]. By utilizing this selective volume compensation method, the amount of compensation material required is substantially reduced, minimizing the Q degradation of the devices while achieving full first-order compensation.

This method can be extended to a fused silica-based resonator by picking a passive compensation material with an opposite TCE value. However, due to the large TCF value of fused silica, it is critical to find a material with an extremely large negative TCE to avoid a prohibitively large volume of material to achieve complete compensation. As an example, compensation of fused silica was attempted for glass-blown fused silica resonator using blanket titanium metal deposition [18]. It was shown that as much as 2.5 micrometers of titanium is required to fully compensate a glass-blown structure, which is a substantial fraction of device volume and has a large negative effect on the Q [18, 19]. To avoid as much of these losses as possible, as well as to avoid fabrication and robustness concerns, it is necessary to combine a large negative TCE material with selective compensation placement to maximize the efficiency of the added material. For fused silica, nickel is a promising material for this application. By examining the major electroplating capable metals, it was found that that nickel has an extremely large reported TCE value between -450 ppm/K [20] and -1600 ppm/K [21], depending on deposition method and quality. Nickel also has a low internal loss as compared to other metals [22, 23], as well as the capability to be electroplated in large volumes with controllable stress [20].

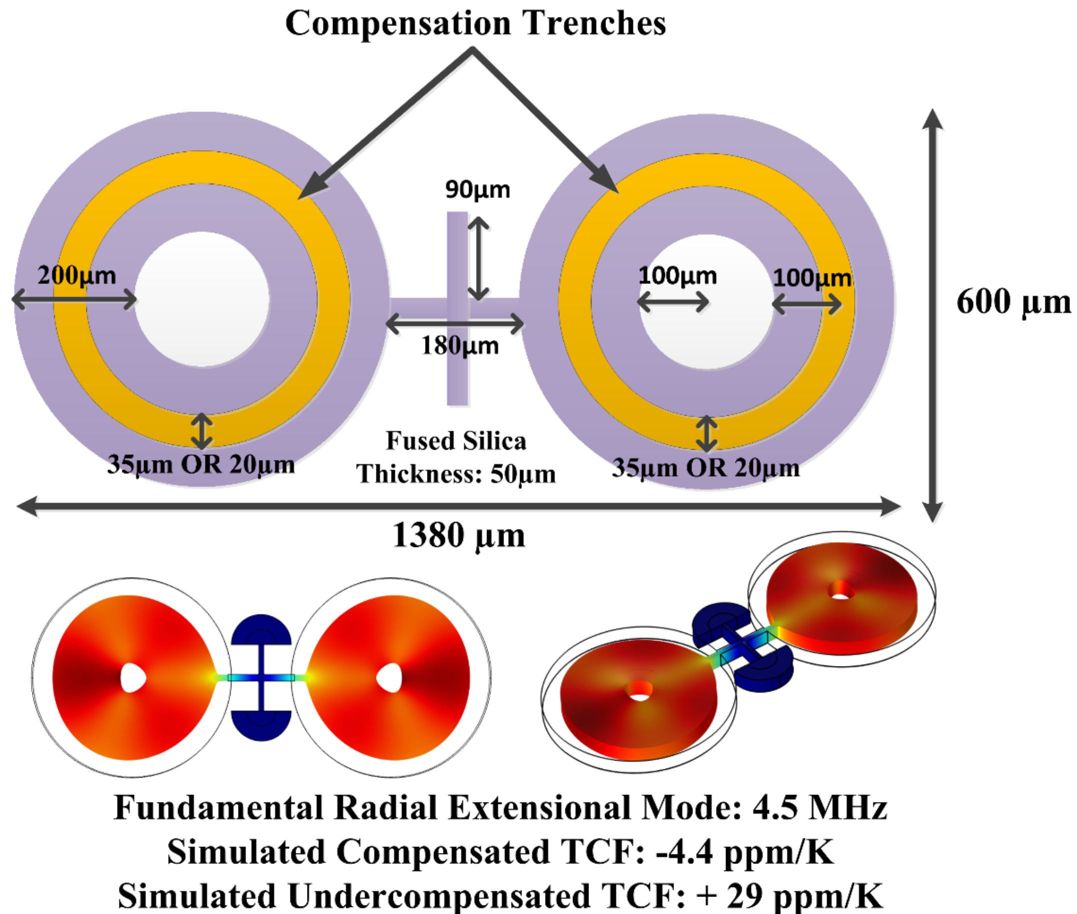

Fig. 4.3: Schematic and simulated mode shapes for the temperature compensated fundamental radial-extensional dogbone devices. The nickel-refilled trenches are placed in the center of each ring to maintain symmetry and maximize strain density across the trench. The simulation data, including predicted TCF, for both trench variations is included. Nickel TCE is assumed to be of -600 ppm/K for these simulations. The nickel trench depth was chosen to be 30 µm out of the 50 µm device thickness, with two different trench widths of 20 µm and 35 µm.

Passive Temperature Compensation with Nickel-Refilled Trenches

To achieve passive temperature compensation in AlN-on-silica devices, embedded nickel-refilled trenches are placed in regions of high strain to achieve maximum compensation with a minimum of added nickel. This is achieved by etching fused silica trenches into the center of each dogbone ring and refilling them with electroplated nickel, allowing the design and placement of trenches as well precise control over the dimensions to achieve accurate compensation. Fig. 4.3 shows the final design schematic for the 50 µm thick compensated dogbone resonator design, with an undercompensated design showing a simulated TCF of +29 ppm/K and a fully compensated

design showing a simulated TCF of -4.4 ppm/K. Due to the fully definable nature of the trenches, almost any TCF can be targeted through the modification of trench geometries.

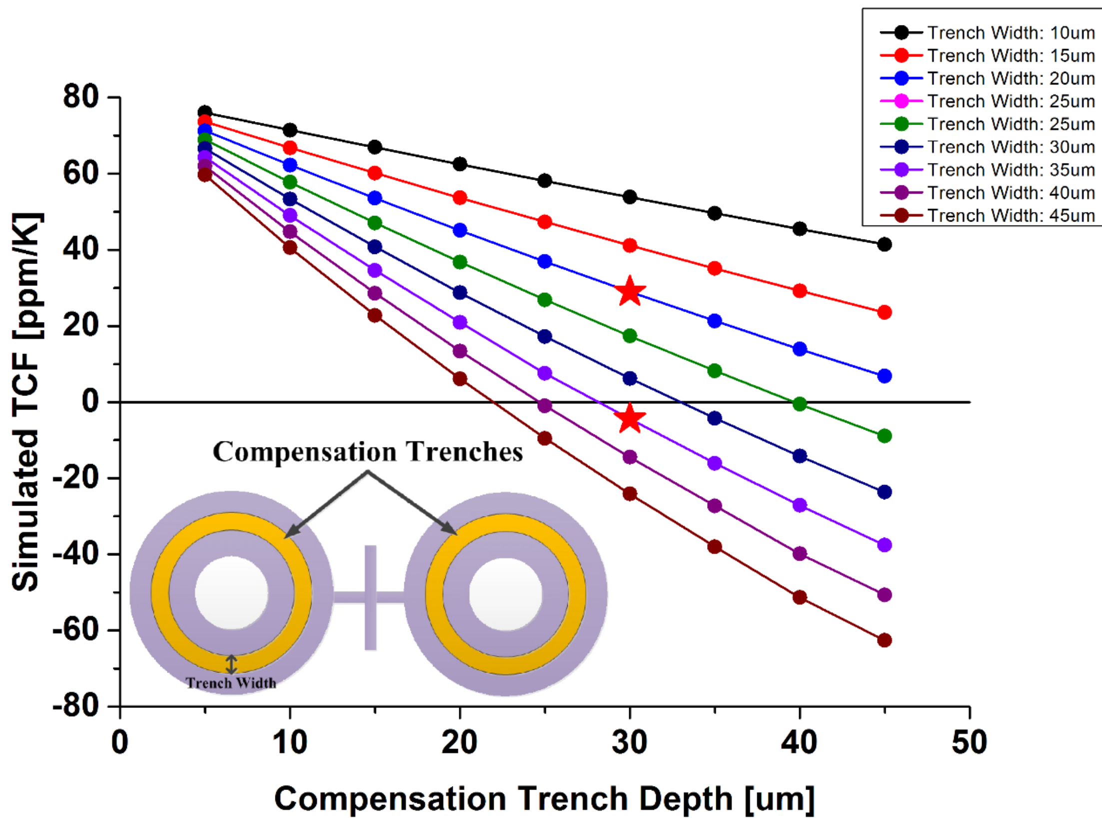

Fig. 4.4: Simulated TCF design space for the temperature compensated dogbone resonators with varied compensation trench and depth and width. Starred data points correspond to the selected dimensions for the fabricated resonators outlined in Fig. 4.3. Nickel is simulated with a TCE of -600 ppm/K. Inset shown sketch of compensated resonator.

The dimensions of the compensation trenches were chosen through COMSOL simulation using the material parameters noted in Table 2.1, specifically assuming a nickel TCE of -600 ppm/K. Fig. 4.4 shows the simulated design space for TCF compensation, a sweep of embedded nickel-refilled trench dimensions was performed with the two finalized compensation trench dimensions starred on the figure. It can be noted that a wide range of trench sizes are achievable with this method, corresponding to a wide range of desired TCF values.

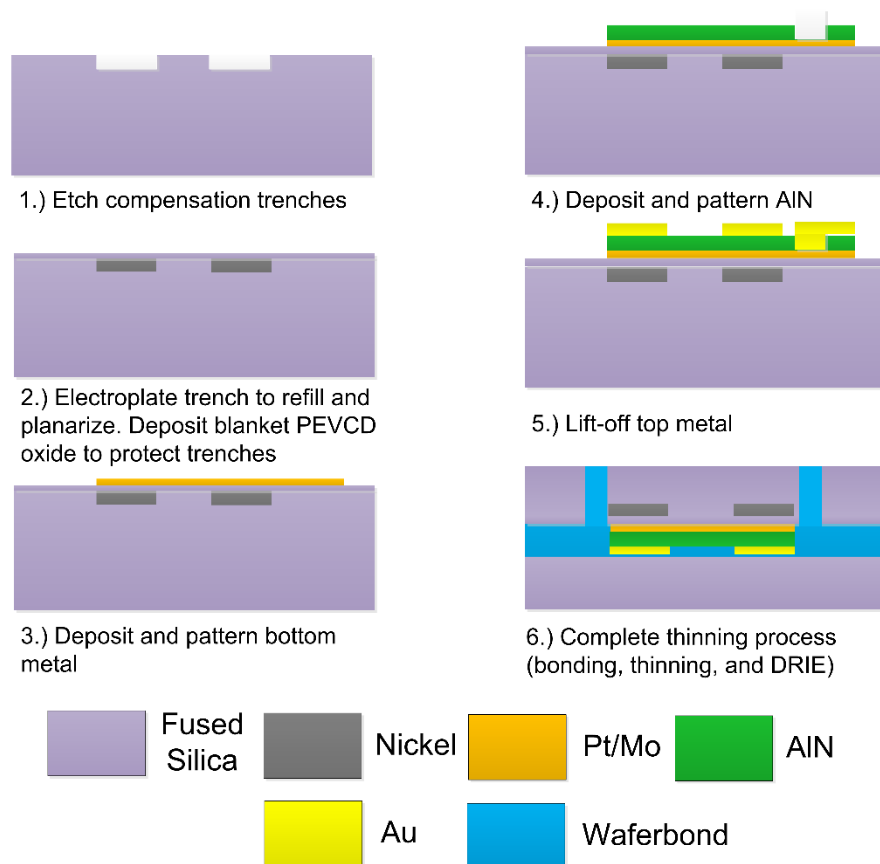

Fig. 4.5: Fabrication flow for the temperature compensated nickel-refilled embedded trench AlN-on-silica resonators

The fabrication process of the passively compensated AlN-on-silica resonators follows a similar flow as discussed in the previous chapters and is outlined in Fig. 4.5. The process begins with a 375 µm thick double side polished Corning 7980 fused silica wafer. The wafer is etched using fused silica DRIE to define the compensation trenches. The wafer is then smoothed in a buffered hydrofluoric acid etch (BHF) to partially smoot the device sidewalls post-etch. Next, a 300 Å titanium and 5000 Å thick gold seed layer is sputter deposited. This seed layer is sputter deposited to ensure full sidewall coverage of the high aspect ratio compensation trenches. Next, low-stress nickel electroplating is performed to refill the compensation trench. The electroplating is done at low power to minimize stress during the thick electroplating. The trenches are slightly overplated to ensure a total refill and then polished back using mechanical lapping to planarize the surface. A 250 nm PECVD SiO_2 layer is then deposited to cover the embedded trenches and protect

them from further processing steps. After this point, the fabrication process proceeds as normal with piezoelectric stack deposition, wafer bonding, release, and cleaning. A SEM image of the fabricated resonator in shown in Fig. 4.6, with a cross-sectional SEM image of a nickel-refilled trench which demonstrates a complete trench refill. More accurate measurements done post-fabrication in a SEM show that non-idealities during the planarization process caused over-etch of the fused silica substrate, decreasing the effective depth of the nickel trench to 20 μm from the designed 30 μm. Additionally, the planarization caused a large amount of surface roughness to the fused silica substrate, causing poor AlN growth and reducing the piezoelectric coupling of the device. Both of these issues can be addressed in future fabrication runs through minor process adjustments to the planarization step, including an updated mounting process for improved leveling and a finer final polish slurry to improve surface roughness.

Measured S-parameters from the temperature-compensated AlN-on-silica resonators are shown in Fig. 4.7. Three resonator designs were measured, an uncompensated design without any nickel-refill trenches as a control, an undercompensated design, and a fully compensated design. The dimensions for the undercompensated and fully compensated design are outlined in Fig. 4.3. It can be seen that the performance of these devices do not match the results presented in earlier chapters, which can partially be attributed to the addition of nickel-refilled trenches but also to the poor ALN piezoelectric coupling from the large substrate surface roughness from planarization. This performance can be significantly improved through the process improvements discussed above and will increase the Q of these devices in future runs.

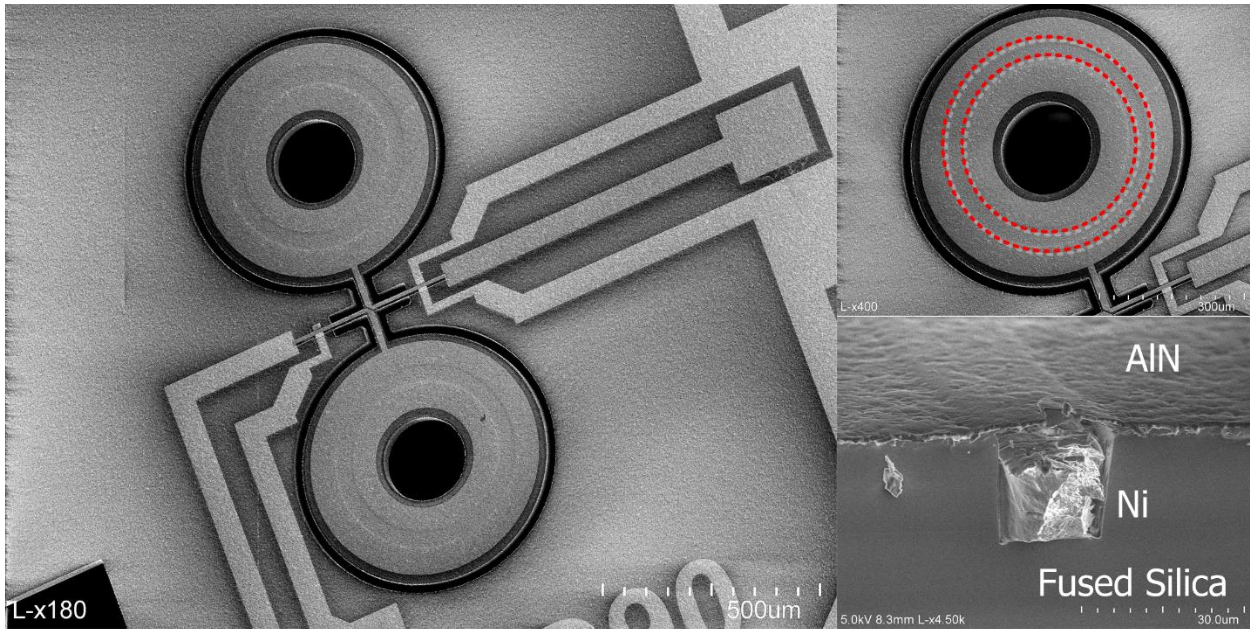

Fig. 4.6: (Left) A SEM image of a fabricated temperature compensated AlN-on-silica resonator. (Top Right) A zoomed in image of a single dogbone ring with the embedded nickel-refilled trench outlined in red. (Bottom Right) A cross-section SEM of a nickel-refilled trench showing complete refill of the trench. The measured depth of this trench was shown to be 20 μm, 10 μm shallower than designed.

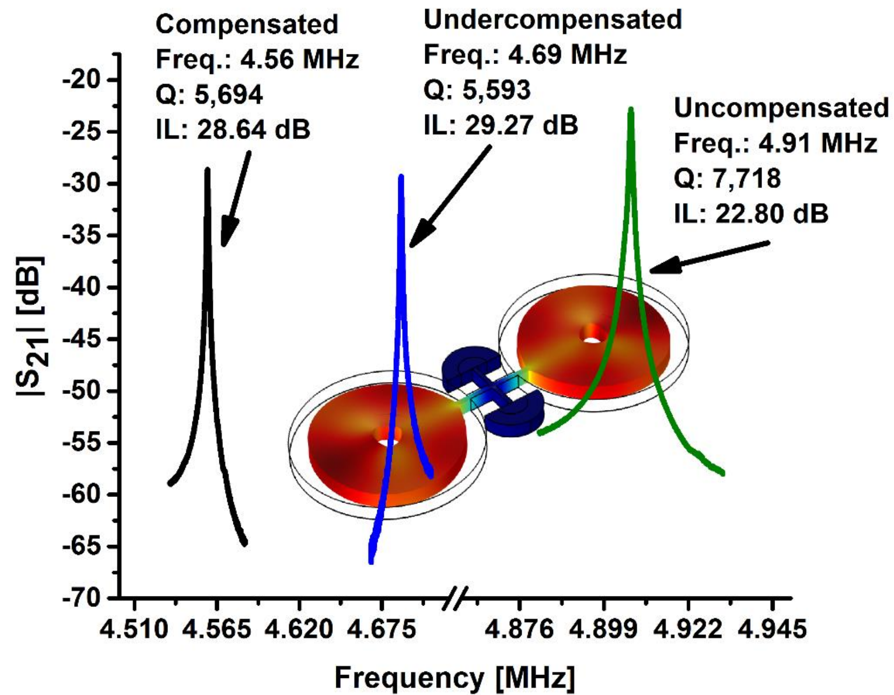

Fig. 4.7: S-parameter response and measured parameters for a compensated, undercompensated, and uncompensated dogbone in the fundamental radial extensional mode. Background image shows the simulated mode shape.

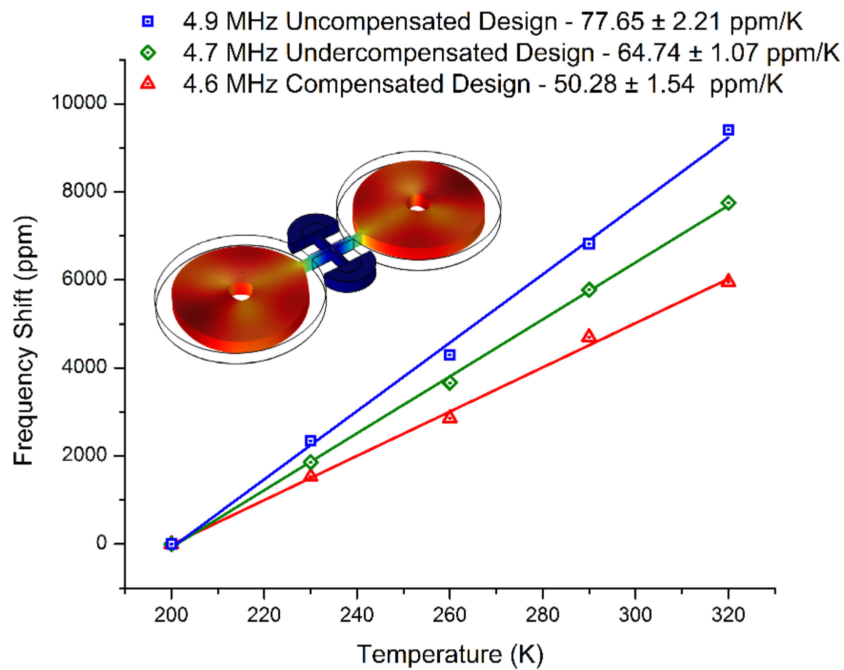

Fig. 4.8: Measured temperature sensitivity of the fabricated temperature compensated AlN-on-silica resonators. The TCF of three designs are shown, the uncompensated reference resonator, the undercompensated trench design, and the fully compensated trench design. The inset shows the simulated mode shape.

The temperature sensitivity of these resonators, shown in Fig. 4.8, was measured in vacuum inside a cryostation chamber at five temperature points between 200 K (-73°C) and 320K (47°C). These data points were linearly fitted to extract a first-order TCF for each resonator along with its respective fitting error. The measured TCF results show a noticeable difference from the simulated TCF results presented in Fig. 4.3 and Fig. 4.4, with the compensated design showing a 27 ppm/K decrease in TCF. This can be partly attributed to the shallower-than-designed compensation trenches, but cannot fully explain the observed TCF difference. By performing SEM-based geometry measurements of fabricated devices and re-simulating the expected TCF with the updated dimensions it is possible to fit the nickel TCE to measured results. A re-simulated graph of TCF results is shown in Fig. 4.9, where the device thickness is reduced to 40 µm and the nickel trench depth is reduced to 20 µm. These fitted simulated results suggest that the actual TCE of nickel in these resonators is just -200 ppm/K as compared to the -450 ppm/K or higher reported in

literature. This large discrepancy in values suggests that another factor may be in play with these temperature-compensated devices, such as mode shape distortion due to the large added mass of nickel. This effect would distort the mode shape of the radial extensional mode and move regions of high strain away from the nickel-refilled trench regions, reducing effective compensation. Further investigation is required to better understand the effects in this system, but as shown in Fig. 4.9, the low effective TCE of nickel makes it extremely difficult to fully compensate these AlN-on-silica devices with only passive compensation. Even so, in combination with ovenization this reduced sensitivity can minimize the effects of thermal gradients and noticeably improve the frequency stability of the timing references.

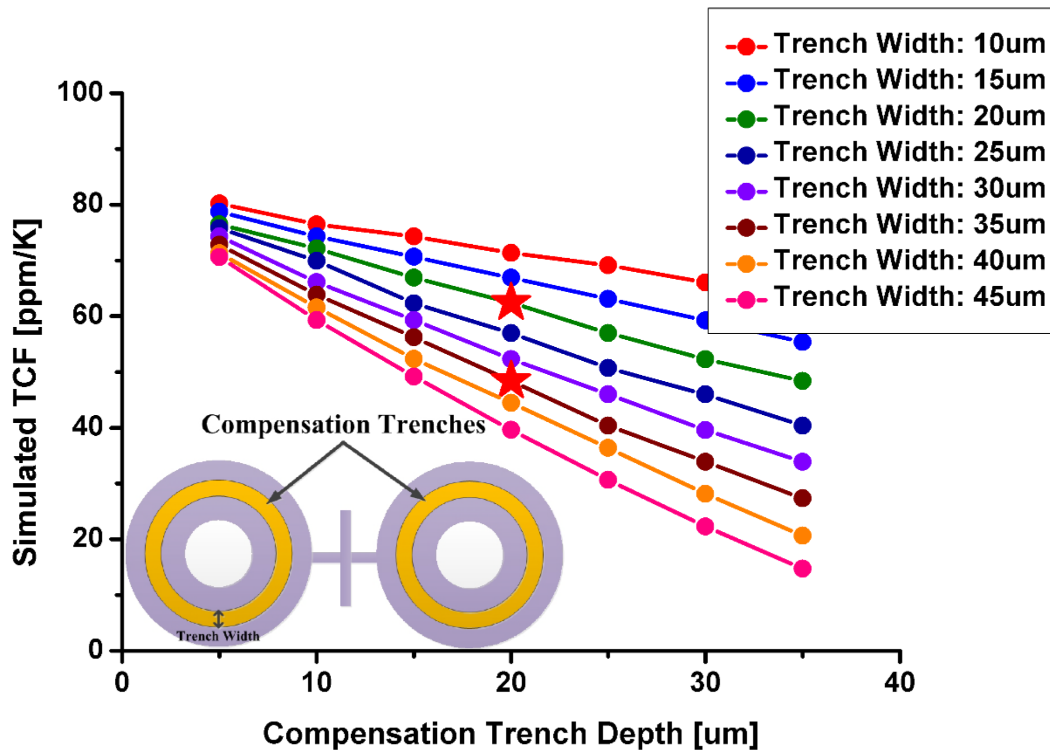

Fig. 4.9: Simulated TCF design space for the fitted temperature compensated AlN-on-silica devices with the device schematic in the inset. With data taken from SEM geometry measurements, the trench depth was reduced to 20 µm from 30, and the overall device thickness was reduced to 40 µm from 50. The assumed nickel TCE for these simulations was -200 ppm/K. It is important to note that complete compensation of these devices will require a large amount of added material.

An important consideration in these devices, as noted in Chapter 2, is the long-term stability of the devices and its aging properties. Stress in the electroplated nickel is a critical factor, as when the compensation material ages residual stress from the material and polycrystalline boundaries in the nickel will change. This shift in stress will affect both the resonance frequency and the Q of the final device. The addition of a compensation material also introduces another interface into the device stack, and as the stress at this interface changes over time additional instability is expected. While the long-term stability of these passively compensated AlN-on-silica devices has not been investigated, published literature results show electroplated nickel devices with a total drift of 200 ppm over a 1200-hour period [20]. This is a significant amount of drift in these devices, which makes it a factor that must be addressed to reach the ppb levels of stability required. Burn-in periods and careful package design for the devices can reduce some of this effect, but frequency shifts in these materials are a serious issue for long term stability.

Combining Passive and Active Compensation Methods

While passive temperature compensation cannot fully compensate the first order effects of TCF on fused silica, a method of significantly increasing device stability by combining passive and active temperature compensation is possible. By using designable temperature compensation trenches, it is possible to compensate specific modes over others, leading to the same device supporting multiple resonance modes that have widely varying TCF values. An example of this is shown in Fig. 4.10, where TCF for two different modes from the same device volume are extracted. The first mode is the traditional fundamental radial extensional mode and shows a measured TCF of 50.28 ppm/K, while a higher order mode, thought to be a third order radial extensional mode, shows a TCF of 21.84 ppm/K, an almost 29 ppm/K difference in TCF between these two modes. This difference is almost as large as the TCF of uncompensated silicon and utilizes the naturally

large TCF of fused silica to make an extremely temperature sensitive mode. This large sensitivity can be utilized as a temperature sensor, replacing the RTD or thermistor of the ovenized system with a second resonator.

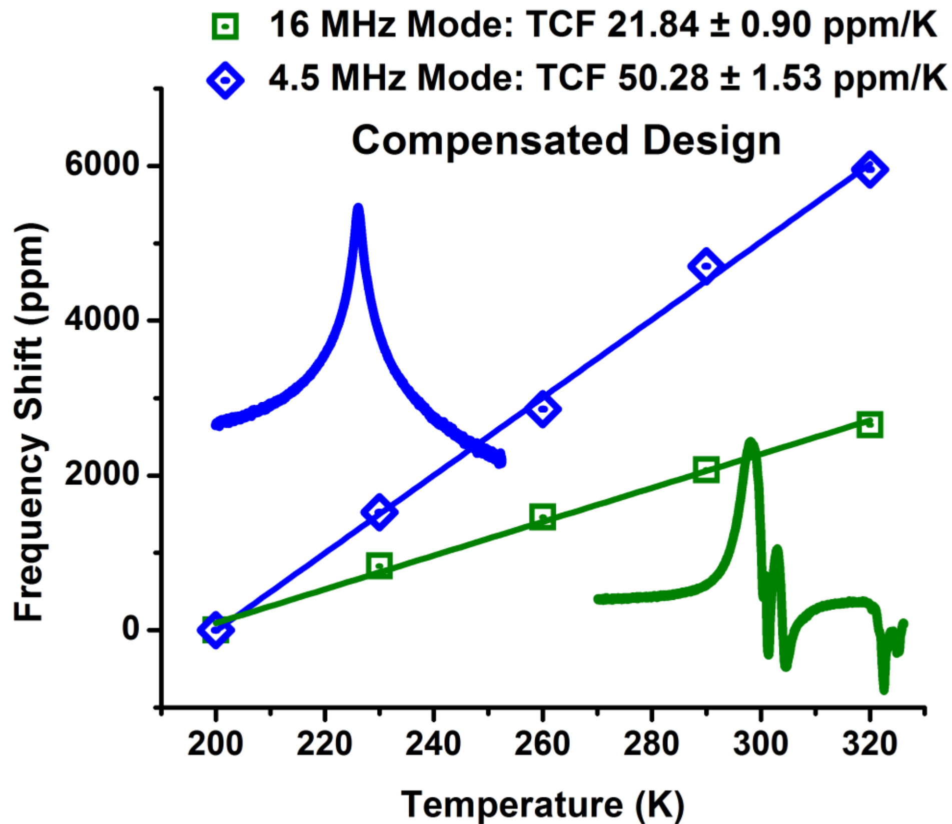

Fig. 4.10: Measured TCF results of a fabricated temperature compensated AlN-on-silica device with multiple modes on the same device. The first mode, a traditional fundamental radial extensional mode, shows a TCF of +50 ppm/K. In comparison, a second mode on the same device, thought to be a third-order radial extensional mode, has a TCF of +21 ppm/K. There is a TCF different of +29 ppm/K between modes on the same device volume, which opens up a potential application as dual-mode resonators.

This idea can be extended to a system with two similar device geometries, each one operated in a different resonant mode with a different TCF. One of these devices will be highly compensated, giving a stable reference frequency, while the other device will have a larger TCF and be used as a temperature sensor. The similar device geometries will allow for minimal thermal resistance between devices on the same platform, leading to a minimal thermal drift and therefore increased device stability [8]. Extending this same idea further, it should also be possible to sustain two resonant modes on the same device volume, each with a different TCF. This setup, known as

a dual-mode resonator, would effectively eliminate the thermal gradients found in the ovenized platform as the temperature sensor and the resonant device are contained in the same volume. An investigation of dual-mode resonator design and implementation is discussed in the next chapter.

References

[1] Z. Wu, A. Peczalski, V. A. Thakar, Z. Cao, Y. Yuan, G. He, R. L. Peterson, K. Najafi and M. Rais-Zadeh, "Piezoelectrically transduced high-Q silica micro resonators," in *Proceedings of the 26th IEEE International Conference on Micro Electro Mechanical Systems (MEMS),* San Francisco, CA, USA, 2013, pp. 122-125.

[2] M. A. Hopcroft, W. D. Nix and T. W. Kenny, "What is the Young's modulus of silicon?" *J. Microelectromech. Syst.,* vol. 19, pp. 229-238, Apr., 2010.

[3] V. A. Thakar, Z. Wu, A. Peczalski and M. Rais-Zadeh, "Piezoelectrically transduced temperature-compensated flexural-mode silicon resonators," *J. Microelectromech. Syst.,* vol. 22, pp. 815-823, May, 2013.

[4] R. Tabrizian, M. Pardo and F. Ayazi, "A 27 MHz temperature compensated MEMS oscillator with sub-ppm instability," in *Proceedings of the 25th IEEE International Conference on Micro Electro Mechanical Systems (MEMS),* Paris, France, 2012, pp. 23-26.

[5] A. K. Samarao and F. Ayazi, "Temperature compensation of silicon resonators via degenerate doping," *IEEE Trans. Electron Devices,* vol. 59, pp. 87-93, Jan., 2012.

[6] M. H. Perrott, J. C. Salvia, F. S. Lee, A. Partridge, S. Mukherjee, C. Arft, J. Kim, N. Arumugam, P. Gupta, S. Tabatabaei, S. Pamarti, H. Lee and F. Assaderaghi, "A temperature-to-digital converter for a MEMS-based programmable oscillator with +/-0.5 ppm frequency stability and less than 1 ps integrated jitter," *IEEE J. Solid State Circuits,* vol. 48, pp. 276-291, Jan., 2013.

[7] M. Li, C. Chen, C. Li, C. Chin and S. Li, "A monolithic CMOS-MEMS oscillator based on an ultra-low-power ovenized micromechanical resonator," *J. Microelectromech. Syst.,* vol. 24, pp. 360-372, Mar., 2014.

[8] Z. Wu and M. Rais-Zadeh, "A temperature-stable piezoelectric MEMS oscillator using a CMOS PLL circuit for temperature sensing and oven control," *Journal of Microelectromechanical Systems,* vol. 24, pp. 1747-1758, June, 2015.

[9] J. R. Vig, "Quartz crystal resonators and oscillators," *US Army Communications-Electronics Command,* Jan., 2001.

[10] R. Tabrizian and F. Ayazi, "Acoustically-engineered multi-port AlN-on-silicon resonators for accurate temperature sensing," in *Proceedings of the IEEE International Electron Devices Meeting (IEDM),* Washington D.C., USA, 2013, pp. 18.1.1-18.1.4.

[11] C. M. Jha, M. A. Hopcroft, S. A. Chandorkar, J. C. Salvia, M. Agarwal, R. N. Candler, R. Melamud, Bongsang Kim and T. W. Kenny, "Thermal isolation of encapsulated MEMS resonators," *J Microelectromech. Syst.,* vol. 17, pp. 175-184, Feb., 2008.

[12] B. Kim, R. H. Olsson and K. E. Wojciechowski, "Ovenized and thermally tunable aluminum nitride microresonators," in *Proceedings of the IEEE International Ultrasonics Symposium,* San Diego, CA, USA, 2010, pp. 974-978.

[13] Z. Wu, A. Peczalski and M. Rais-Zadeh, "Low-power ovenization of fused silica resonators for temperature-stable oscillators," in *2014 IEEE International Frequency Control Symposium (FCS);* 2014, pp. 1-5.

[14] Z. Wu, A. Peczalski and M. Rais-Zadeh, "Device-layer ovenization of fused silica micromechanical resonators for temperature-stable operation," in *Proceedings of the Solid-State Sensors, Actuators and Microsystems Workshop (Hilton Head),* Hilton Head Island, SC, USA, 2014, pp. 87-90.

[15] Z. Wu, "Microelectromechanical systems for wireless radio front-ends and integrated frequency references," *University of Michigan, Ph. D. Thesis,* 2014.

[16] R. Melamud, B. Kim, S. A. Chandorkar, M. A. Hopcroft, M. Agarwal, C. M. Jha and T. W. Kenny. Temperature-compensated high-stability silicon resonators. *Appl. Phys. Lett. 90(24),* pp. 244107. 2007.

[17] R. Tabrizian, G. Casinovi and F. Ayazi, "Temperature-stable high-Q AlN-on-silicon resonators with embedded array of oxide pillars," in *Proceedings of the Solid-State Sensors, Actuators, and Microsystems Workshop (Hilton Head),* Hilton Head Island, SC, USA, 2010, pp. 100-101.

[18] J. Giner, L. Valdevit and A. M. Shkel, "Glass-blown pyrex resonator with compensating ti coating for reduction of TCF," in *International Symposium on Inertial Sensors and Systems (ISISS 2014),* Laguana Beach, CA, USA, 2014, pp. 1-4.

[19] T. Nagourney, J. Y. Cho, A. Darvishian, B. Shiari and K. Najafi, "Effect of metal annealing on the Q-factor of metal- coated fused silica micro shell resonators," in *Proceedings of the IEEE International Symposium on Inertial Sensors and Systems (ISISS),* Hapuna Beach, HI, USA, 2015, pp. 1-5.

[20] M. W. Putty, "Micromachined vibrating ring gyroscope," *University of Michigan, Ph. D. Thesis,* 1995.

[21] L. L. Chu, Long Que and Y. B. Gianchandani, "Temperature coefficients of material properties for electrodeposited MEMS," in *Proceedings of the 14th IEEE International Conference on Micro Electro Mechanical Systems (MEMS),* Interlaken, Switzerland, 2001, pp. 68-71.

[22] V. B. Braginsky, V. P. Mitrofanov and V. I. Panov, *Systems with Small Dissipation.* Chicago, IL: The University of Chicago Press, 1985.

[23] W. Huang, Z. Ren and C. Nguyen, "Nickel vibrating micromechanical disk resonator with solid dielectric capacitive-transducer gap," in *Proceedings of the IEEE International Frequency Control Symposium and Exposition (IFCS),* Miami, FL, USA, 2006, pp. 839-847.

Chapter 5: Dual-Mode Fused Silica Resonators

Substantial temperature compensation is possible for fused silica devices using a combination of active and passive techniques, but residual thermal gradients on the ovenized platform still create residual error that can lead to unacceptable amounts of frequency instability. One method of resolving these temperature gradients is through the use of dual-mode resonators. Dual-mode resonators work through the utilization of two resonant modes on the same device volume, both actuated simultaneously [1]. This approach has been used before in quartz crystals, as a method to compensate for thermal gradients in ovenization [1] or to compensate for packaging or operational stresses [2]. These modes, using the techniques outlined in the previous chapter, can be designed to have different temperature coefficient of frequency (TCF) values. One mode would act as a stable reference frequency, providing the timing reference signal, and the second mode with the larger TCF would act as a temperature sensor. Ideally, the stable reference frequency will have a near-zero TCF value while the temperature sensing mode would have as high a TCF as possible. Because these two modes share the same device volume; there is no thermal lag between the modes and any thermal gradients would be entirely eliminated, greatly increasing the temperature stability of the ovenized system.

Acoustic Phonon Trapping

One issue with dual-mode resonators lies in the difficulty in supporting multiple resonance modes on a single device geometry without incurring significant anchor losses. As the mode shape shifts, the best tether points to minimize anchor losses will shift as well, causing one mode to suffer in terms of performance. Both modes in the dual-mode resonator are critical to providing stable performance, whether through the timing reference itself or through accurate temperature sensing, and so a method of cleanly sustaining both modes is needed.

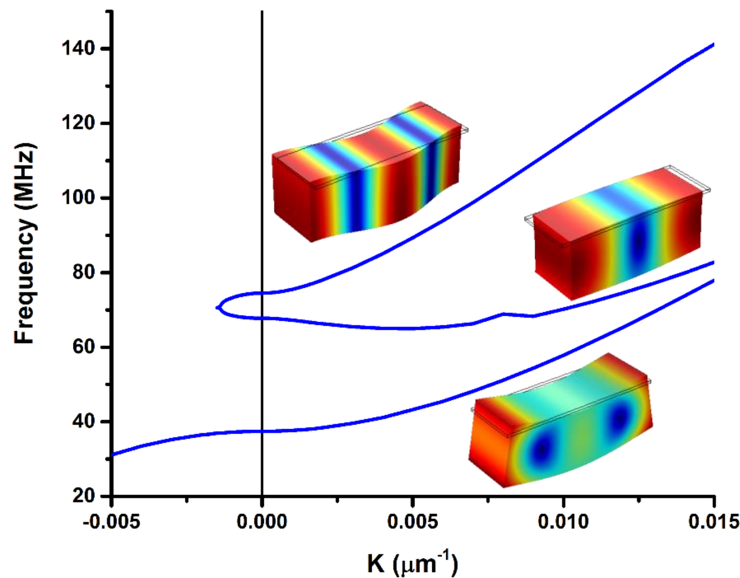

Fig. 5.1: Simulated dispersion curve (wavenumber versus frequency) for a selection of possible branches for an infinite beam 62.5 μm wide and 20 μm thick. The vertical black line notes the line between propagating (positive K) waves and evanescent (negative K) waves. Inset shows the simulated mode shapes for each wave branch, from top to bottom: a fundamental flexural mode, a fundamental width extensional mode, and a fundamental shear mode.

One such method of anchor loss reduction is known as phonon trapping or acoustic engineering [3, 4]. This method takes advantage of the evanescent region of the acoustic dispersion curve to effectively trap acoustic energy in the center of the device and maintaining low anchor loss. An example dispersion curve is shown is Fig. 5.1, and was simulated using COMSOL. A more robust discussion on the calculation and derivation of dispersion curves can be found in [5]. This dispersion curve shows a selection of the possible standing-wave solutions on an AlN-on-

silicon beam, with the fundamental flexural mode, fundamental width extensional mode, and fundamental shear mode shown. The beam is 62.5 µm wide and 20 µm thick with 1 µm of AlN film on top, and for the purposes of the dispersion curve calculations is considered to be infinitely long. This graph has two regions, a positive wavenumber (K) region which contains propagating solutions and a negative wavenumber (K) region that is composed of evanescent, or exponentially decaying solutions. While most resonators use propagating standing wave solutions, acoustically engineered phonon traps take advantage of a synthesized mode combining the properties of both wave types to trap an acoustic wave in a specific area. An example of this is shown in Fig. 5.2, where a dispersion curve for a flexural mode is shown with a slowly decreasing width. As the width decreases the mode begins to couple to evanescent modes, which exponentially decay in strength and reflect energy back towards the center. This approach is used to acoustically engineer dual mode devices, and has the benefit of avoiding the typical anchor limitations due to anchor loss while increasing potential power handing [6].

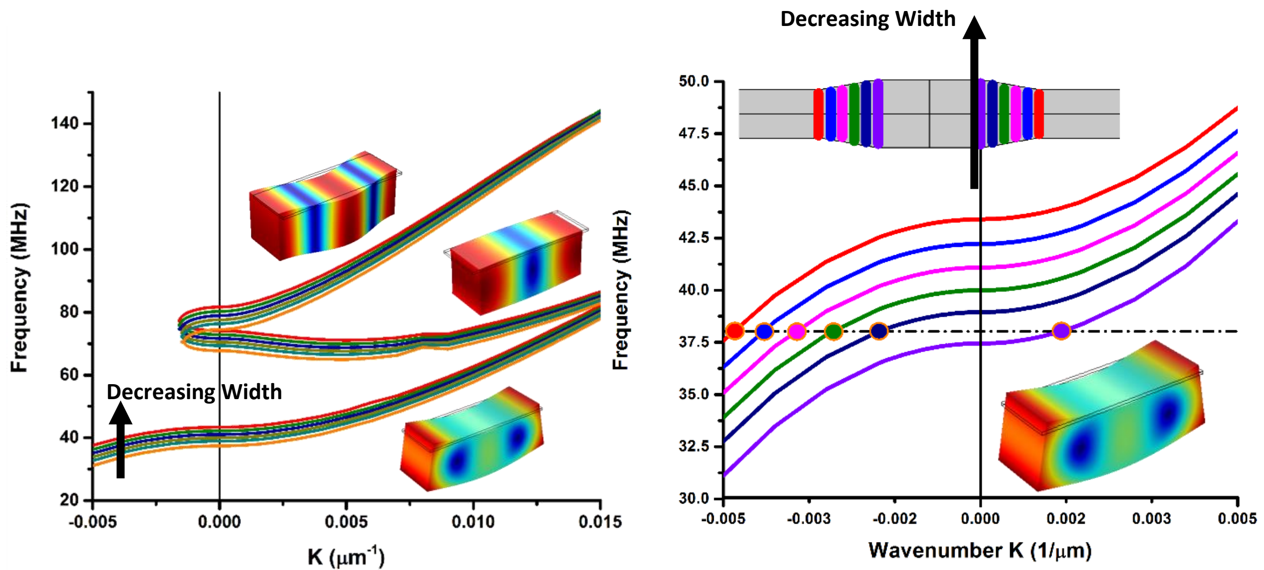

Fig. 5.2: (Left) Simulated dispersion curves for a selection of possible branches for a series of infinite beams 57 µm to 62.5 µm wide and 20 µm thick. Insets show the simulated mode shapes for each branch. (Right) A zoomed view of the flexural branch for a device that slowly decreases in width. Each dispersion color represents a specific region on the geometry shown above, effectively synthesizing a propagating mode with a number of evanescent modes. The inset shows the simulated mode shape of the flexural branch. The vertical black line notes the line between propagating (positive K) waves and evanescent (negative K) waves for both images.

Design of Dual-Mode Phonon Trap Devices

By using the phonon trap technique outlined above, it is possible to acoustically confine a mode to the center of a structure, avoiding anchor losses from the wider tethers. This allows more freedom in choosing modes for a wide TCF differential while maintaining high performance. For these devices, a flexural and width extensional mode was chosen for the two modes due to their difference in maximum strain positioning. The flexural mode has maximum strain at ¼ and ¾ of its width, whereas the width extensional mode experiences maximum strain exactly in the middle of the body. By placing refilled trenches in the middle or at the quarter and three-quarter points of the resonator, either mode can be selected for temperature compensation. This is achieved using the trench-refill based temperature compensation methods outlined in the previous chapter.

The chosen dimensions for these devices are shown in Fig. 5.3, with an overall device length of 900 µm and an initial width of 125 µm for the phonon trap region slowly tapering to 116 µm. The device structure is composed of three regions: the 250 µm tether regions that connect to the device substrate, the 100 µm transition region where the width slowly shifts from the 116 µm width at the anchors to the 125µm center trapped region, and the 200 µm phonon trapped region where the mode is confined. Thickness-wise, this structure is 20 µm thick with a 1 µm piezoelectric AlN region for actuation. The simulated mode shapes and frequency for the designed flexural and width extensional mode are included in Fig. 5.3. Both the flexural and width extensional mode are contained within the phonon-trapped region, with simulated frequencies at 11 MHz and 33 MHz, respectively.

These device geometries were found through optimization of COMSOL simulations to minimize strain density in the tether region, which correspond to the effectiveness of the evanescent mode coupling in the width transition region. The strain versus position graph for the two designed

phonon trapped modes can be seen in Fig. 5.4. Both the flexural and width extensional modes are plotted with their mode shape for reference, and both modes show a concentration of stain energy in the center of the device.

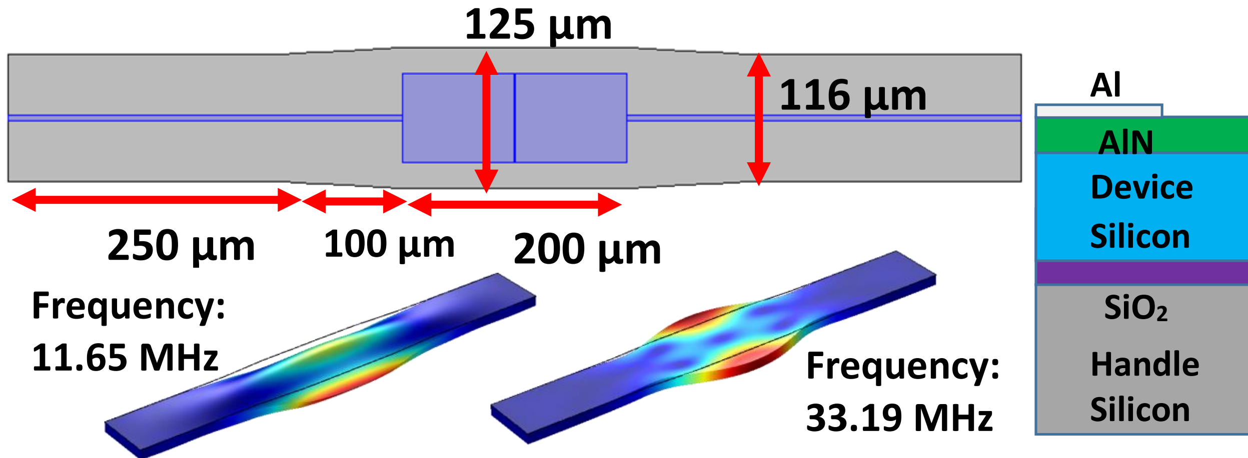

Fig. 5.3: A schematic of the dual-mode phonon trap resonator. The overall length of the device is 900 µm, a 250 µm tether region which is 116 µm wide, a 100 µm transition region that slowly transfers from 116 µm to the final width of 125 µm for the main phonon trapped region, which is 200 µm in length. The device is 20 µm thick with a 1 µm thick AlN piezoelectric layer. The simulated mode shapes for each trapped mode are shown with their respective frequency.

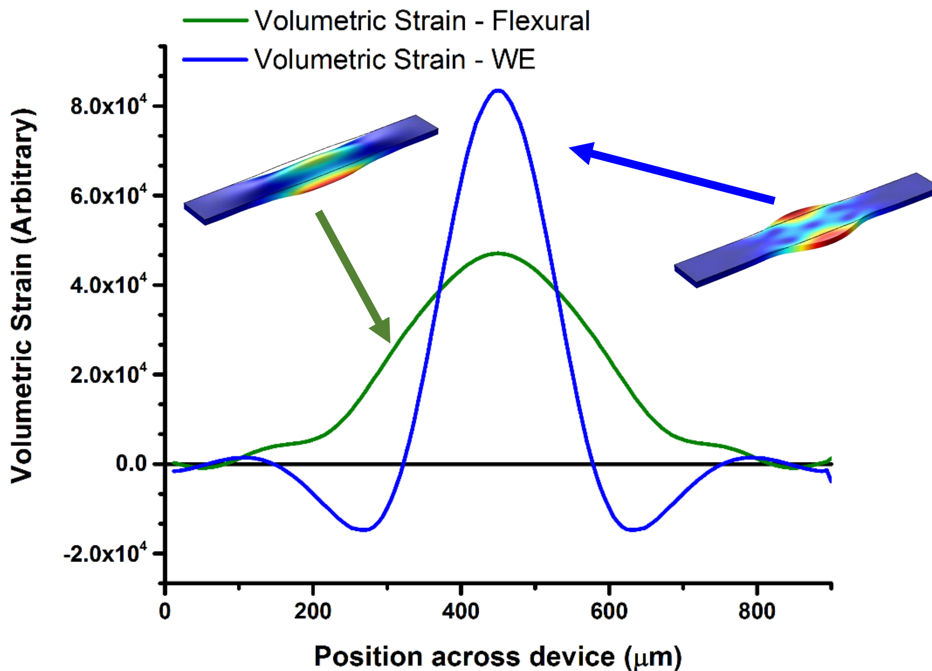

Fig. 5.4: Simulated strain density for the designed dual-mode phonon trap resonators versus position across the device. Each strain line is matched to a simulated mode shape for reference. Note that the majority of energy in each mode is isolated in the center of the device, demonstrating successful phonon trapping.

Temperature Sensitivity of Dual-Mode Phonon Trap Resonators

With the two mode shapes successfully confined in the phonon trap region, a method of temperature compensation needs to be determined. While the geometry of the resonator is designed to allow for passive temperature compensation through embedded trenches, the prototype of the dual-mode phonon trap resonator was made in silicon rather than fused silica. Silicon was chosen as the fabrication material due to the ease of fabrication and faster turnaround for prototype designing. However, due to silicon's single crystal nature, there are other methods of passive temperature compensation other than the use of compensation materials. This alternative method of temperature compensation uses degenerate doping of single-crystal silicon. It has been reported that the concentration and type of doping in silicon has a direct effect on the temperature sensitivity of the material [7]. Recently published work [8] has outlined an equation based on experimental data to determine elastic parameters and temperature sensitivity in doped silicon. From this, elastic parameters outlined in Table 5.1 were obtained and used to simulate the temperature sensitivity and overall TCF of the devices.

With a method to estimate material parameters and temperature sensitivity in silicon, it is possible to further investigate how acoustic engineering affects the TCF of the phonon trapped mode. Fig. 5.5 outlines the simulated TCF across the dispersion branches for each of the selected modes. The silicon doping used for this simulation is phosphorus doping with a concentration of 4.59e19 cm^{-3} with a <100> orientation, which was also used in device fabrication. A noticeable difference was seen in between <100> and <110> device orientation for temperature sensitivity [8], mainly with the change of TCF in the evanescent regions. In order to best utilize the evanescent

mode to increase the TCF of the width extensional mode while maintaining the flexural mode at near-zero TCF, it is necessary to utilize <100> device orientation.

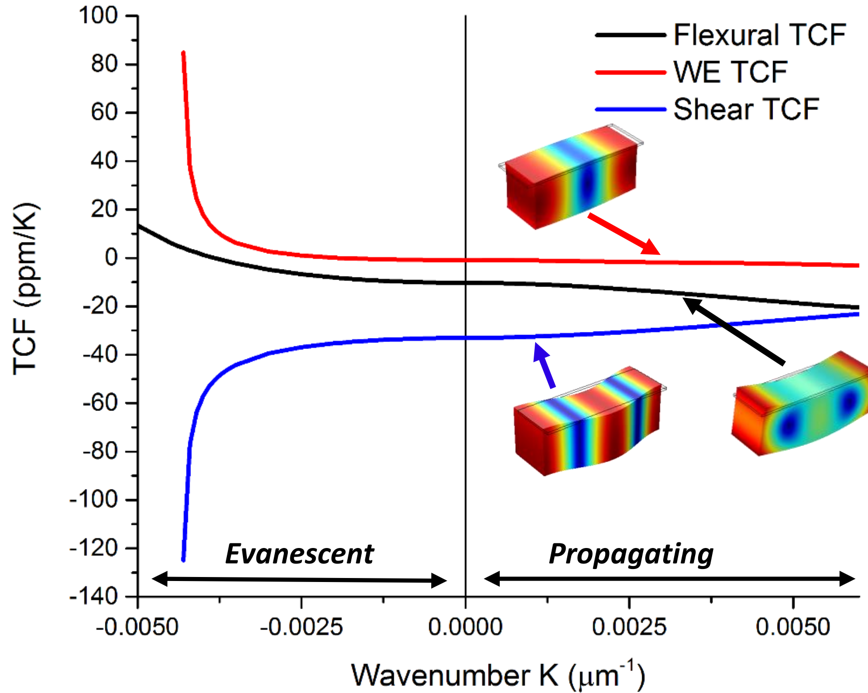

Fig. 5.5: Simulated TCF for each dispersion branch. Inset shows simulated mode shape for each branch. Note how the evanescent mode shows a large shift in TCF over the evanescent modes. This allows for some TCF modification of the synthesized mode.

Due to the influence of the evanescent modes on the overall TCF of the device, the temperature difference between the two modes can be increased through synthesized mode design. Once simulated, the temperature sensitivity of the two modes was found to be -2.43 ppm/K for the flexural mode and 11.52 ppm/K for the width extensional mode. The TCF of these two modes is varied by almost 14 ppm/K though doping compensation, with a potential for further improvement through the use of material compensation (for example using SiO_2 trenches). For the prototype of the devices, no extra compensation material was added in order to maximize performance and to test the phonon-trapping and evanescent mode TCF effectiveness. When this approach is utilized

in an AlN-on-silica system, the nickel-refilled trench method is required to properly compensate the device.

Table 5.1

Material Parameters of Doped Silicon and AlN for Phonon Trap Simulations

Coefficients of Elasticity	**Phos. N-type Silicon – 4.59e19 cm^{-3} [8]**	**AlN [9]**
C_{11} (GPa)	162.95	345
C_{12} (GPa)	65.68	125
C_{13} (GPa)	-	120
C_{33} (GPa)	-	395
C_{44} (GPa)	78.87	118
C_{66} (GPa)	-	110
Temperature Coefficient of Elasticity – First Order		
$T_{C11}^{(1)}$ (ppm/K)	-35.13	-80
$T_{C12}^{(1)}$ (ppm/K)	132.59	-180
$T_{C13}^{(1)}$ (ppm/K)	-	-160
$T_{C33}^{(1)}$ (ppm/K)	-	-100
$T_{C44}^{(1)}$ (ppm/K)	-66.84	-50
$T_{C66}^{(1)}$ (ppm/K)	-	-50
Temperature Coefficient of Elasticity – Second Order		
$T_{C11}^{(2)}$ (ppm/K)	-108.11	-
$T_{C12}^{(2)}$ (ppm/K)	17.39	-
$T_{C44}^{(2)}$ (ppm/K)	46.26	-

Fabrication of Dual-Mode Phonon Trap Resonators

The fabrication of the dual-mode phonon trap resonators is fairly straightforward due to the use of silicon as the substrate material. An overview of the fabrication process is outlined in Fig. 5.6. The process starts with a double side polished silicon-on-insulator (SOI) wafer, consisting of a 500 μm handle layer and a 20 μm highly doped device layer. The device layer is n-type phosphorus doped at 1.59 mΩ-cm, or 4.59×10^{19} cm^{-3}. The process starts by blanket depositing AlN directly on to the highly doped silicon layer. Because the silicon is highly conductive, it can serve as the ground layer for the piezoelectric stack and minimize additional layers, decreasing interface loss and insuring a highly orientated AlN layer. Next, the metal routing is defined through lift-off of a 75 nm Al layer. Al was chosen as the routing metal due its excellent adhesion to AlN and its

similar acoustic match to reduce losses. The resonator dimensions are then defined through a front-side silicon DRIE to the buried oxide layer (BOX) beneath. The device is then released from the wafer backside and the BOX layer is removed, ensuring the resonators are free-standing. A SEM of a fabricated device is shown in Fig. 5.7. The Al routing layer does not have much contrast against the AlN layer, but can be seen due to the charging effect on the dielectric AlN.

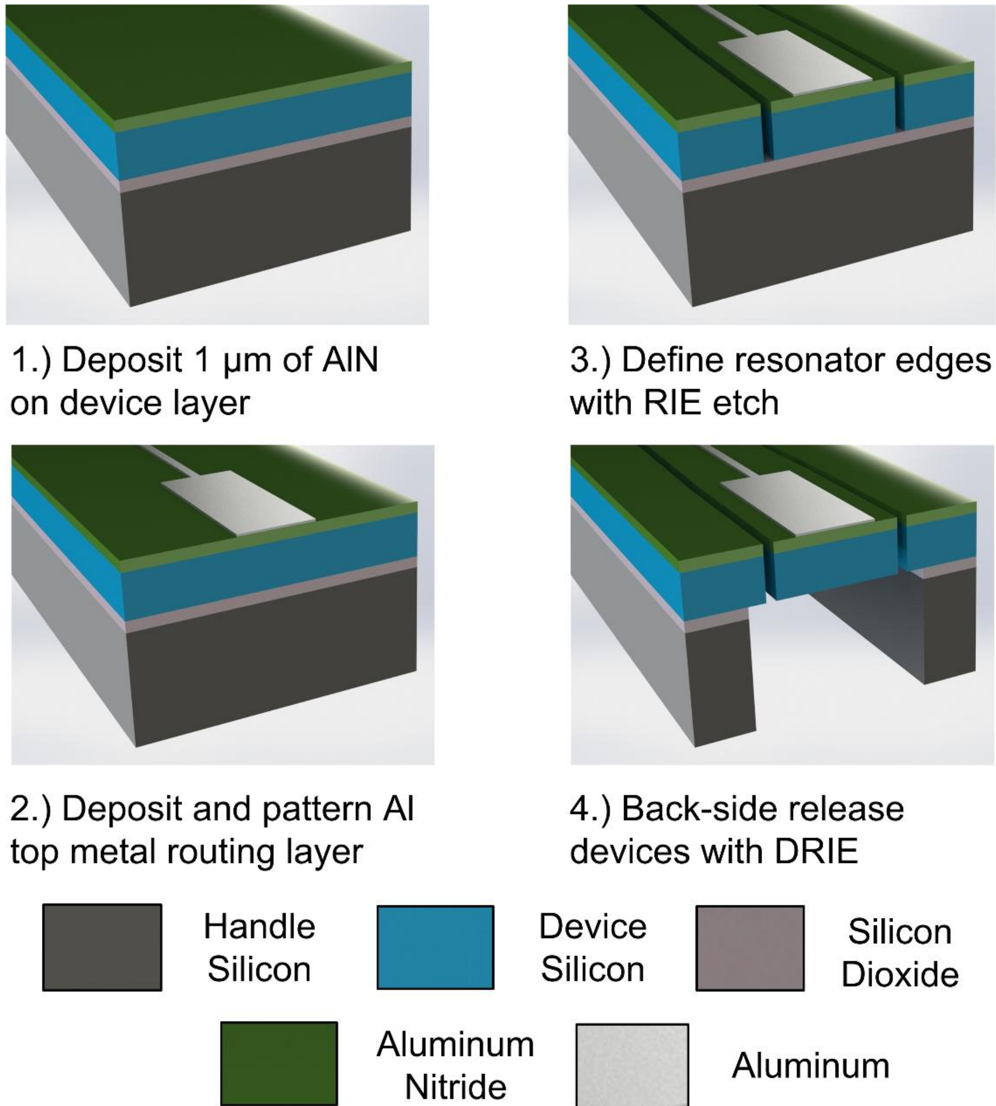

Fig. 5.6: Process fabrication flow for the silicon dual-mode phonon trap resonators.

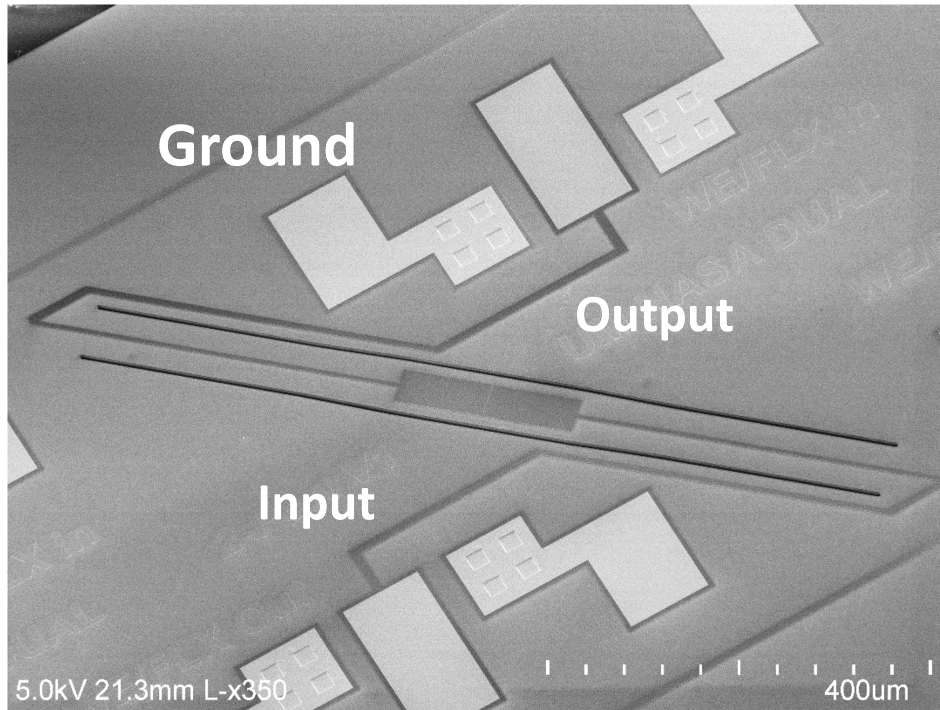

Fig. 5.7: SEM image of a fabricated dual-mode phonon trap resonator. Input and output pads are labeled with a ground pad that allows access to the highly doped silicon layer.

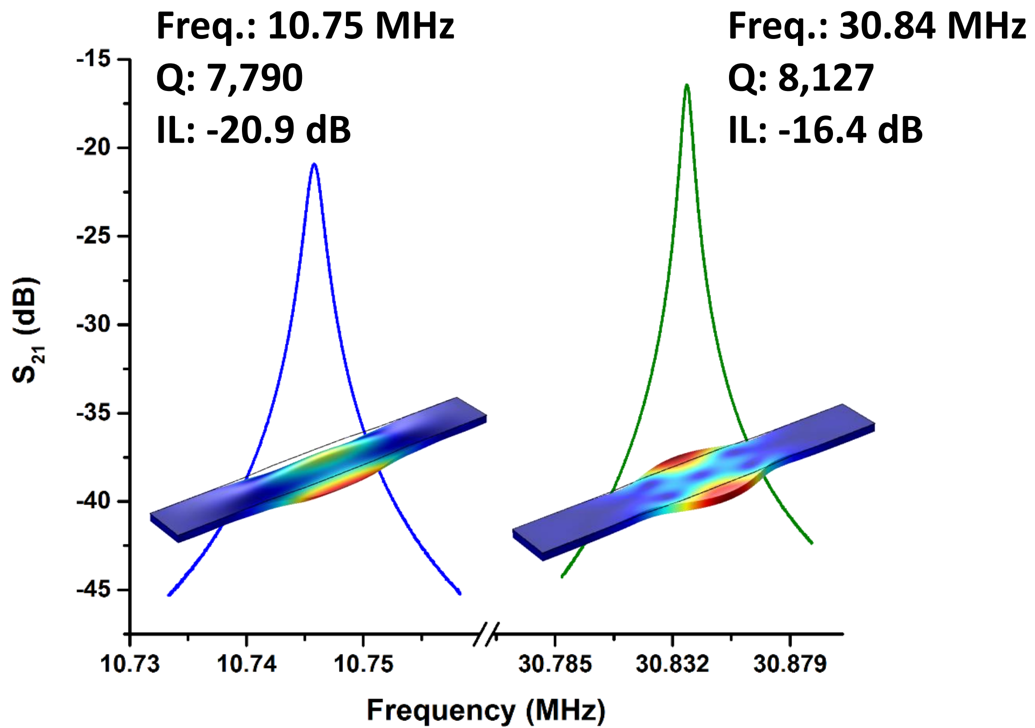

Fig. 5.8: Measured S-parameters for the fabricated dual-mode phonon trap resonators. Background shows the simulated mode shapes and measured resonator parameters.

Measured Results of Dual-Mode Phonon Trap Resonators

The S-parameter responses of fabricated resonators were measured using an Agilent E5061b vector network analyzer in a Lakeshore TTPX cryogenic probe station at room temperature in a vacuum less than 10 mTorr. The measured results for the dual-mode resonators are shown in Fig. 5.8. It can be seen that both designed modes are successfully contained in a single device, with a frequency of 10.75 MHz for the flexural mode and a frequency of 30.84 MHz for the width extensional mode.

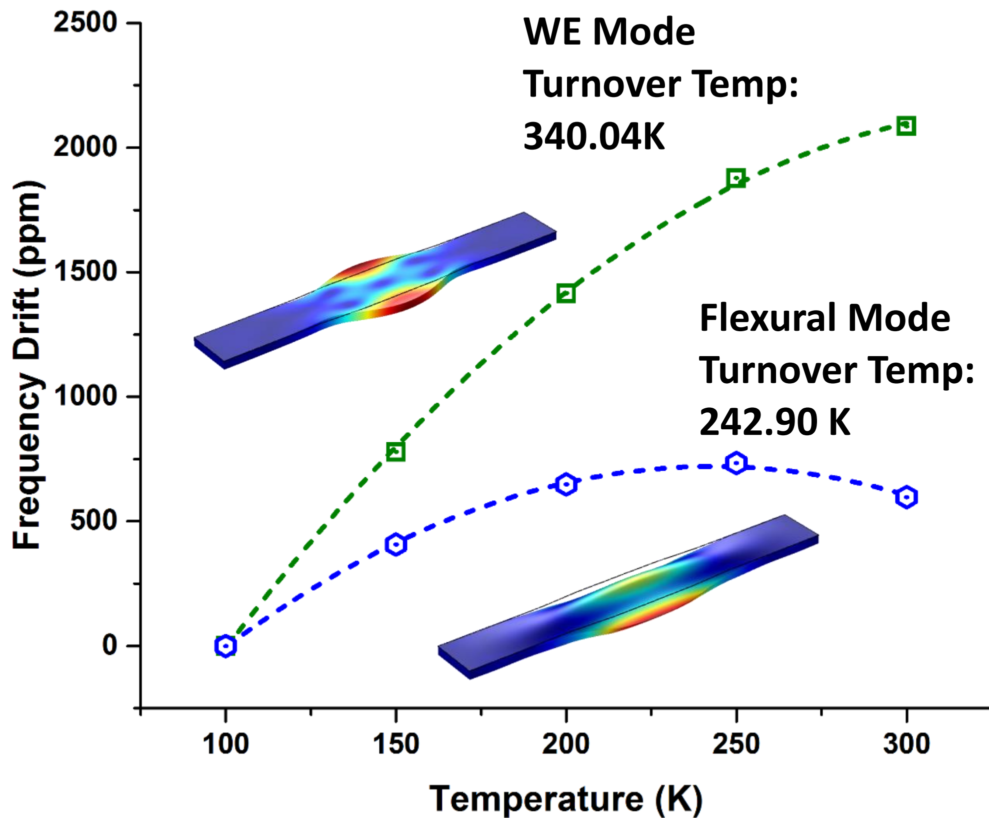

Fig. 5.9: Measured frequency drift on a dual-mode phonon trapped resonator due to temperature fluctuation. Inset shows the simulated mode shape and extracted turnover temperature from second-order polynomial fitting. At the WE mode's turnover point the equivalent TCF of the flexural mode is extracted to be -6.89 ppm/K.

The temperature sensitivity of these resonators, shown in Fig. 5.9, was measured in a cryostation between 100 K and 300 K in 50 K increments. From these data points, a second order

polynomial temperature curve can be fitted and the turnover temperature of the resonator can be determined. Turnover temperature refers to the point of zero temperature-based frequency drift and is based on the maxima of a second-order polynomial fitting curve. This point is the most temperature stable point to ovenize a resonator at, as small fluctuations in the ovenized temperature will have limited effect on the output frequency. For the measured modes, the turnover temperature of the flexural mode was extracted as 242.90 K while the turnover temperature of the width-extensional mode was 340.04 K. If the flexural mode is ovenized at its turnover point of 243 K, the width-extensional (WE) mode will have an equivalent temperature sensitivity of +7.31 ppm/K. Oppositely, with the WE mode ovenized at its turnover temperature the flexural mode has a TCF of -6.89 ppm/K. This, while not as large as the difference shown in compensated fused silica, is a substantial temperature difference for passive compensation in silicon. This can be further increased through the use of SiO_2 temperature compensation trenches in addition to the doping techniques. The turnover temperature of the WE mode, measured at 340K (~67 °C), is relatively close to the ideal ovenization temperature in normal environments. Most ovenized resonator operate at a higher temperature point, typically between 80-90 °C, to ensure that any changes in the environment do not raise the operating point above its designed temperature. As a heater can only change the temperature in one direction, operation above the oven set point needs to be avoided. As the doping is modulating the TCE of the material, any adjustment in the doping concentration of the wafer would move the turnover temperature as well, allowing for modification to match the application requirements. Utilizing this dual-mode method, it is possible to achieve large TCF differences between modes on the same device volume, creating an excellent temperature sensing system for an ovenized system.

References

[1] J. R. Vig, "Dual-mode oscillators for clocks and sensors," in *Proceedings of the IEEE Ultrasonics Symposium,* Caesars Tahoe, NV, USA, 1999, pp. 859-868.

[2] J. A. Kusters, M. C. Fischer and J. G. Leach, "Dual mode operation of temperature and stress compensated crystals," in *Proceedings of the 32nd Annual Symposium on Frequency Control,* Atlantic City, NJ, USA, 1978, pp. 389-397.

[3] R. Tabrizian and F. Ayazi, "Acoustically-engineered multi-port AlN-on-silicon resonators for accurate temperature sensing," in *Proceedings of the IEEE International Electron Devices Meeting (IEDM),* Washington D.C., USA, 2013, pp. 18.1.1-18.1.4.

[4] R. Tabrizian and F. Ayazi, "Thermo-acoustic engineering of silicon microresonators via evanescent waves," *Appl. Phys. Lett.,* vol. 106, pp. 263504, June, 2015.

[5] K. F. Graff, *Wave Motion in Elastic Solids.* New York: Dover Publications, Inc., 1991.

[6] A. Ansari, R. Tabrizian and M. Rais-Zadeh, "A high-Q AlGaN/GaN phonon trap with integrated hemt read-out," in *2015 18th International Conference on Solid-State Sensors, Actuators and Microsystems (TRANSDUCERS 2015),* Anchorage, AK, USA, 2015, pp. 2256-2259.

[7] A. K. Samarao and F. Ayazi, "Temperature compensation of silicon resonators via degenerate doping," *IEEE Trans. Electron Devices,* vol. 59, pp. 87-93, Jan., 2012.

[8] E. J. Ng, V. A. Hong, Y. Yang, C. H. Ahn, C. L. M. Everhart and T. W. Kenny, "Temperature dependence of the elastic constants of doped silicon," *Journal of Microelectromechanical Systems,* vol. 24, pp. 730-741, June, 2015.

[9] J. H. Kuypers, Chih-Ming Lin, G. Vigevani and A. P. Pisano, "Intrinsic temperature compensation of aluminum nitride lamb wave resonators for multiple-frequency references," in *Proceedings of the IEEE International Frequency Control Symposium (IFCS),* Honolulu, Hawaii, USA, 2008, pp. 240-249.

Chapter 6: Summary and Future Work

Effort in this work thus far has centered on creating an ultra-stable, robust timing reference in an attempt to replace currently available ovenized quartz resonators at a fraction of the size, power, and cost of the currently available state-of-the-art. To achieve this, high-quality AlN-on-silica dogbone resonators were fabricated and characterized, demonstrating the first reported piezoelectric fused silica resonator. The loss mechanisms of the AlN-on-silica resonators were then investigated, analytically and experimentally eliminating a variety of loss methods as the dominant mechanism. A new source of loss was proposed to be a dominant loss mechanism, and preliminary simulation results were shown to follow the proposed theory. With a path drawn out to high-performance fused silica resonators, a method was presented to stabilize the large temperature instability of fused silica as a resonant material. Both active and passive temperature compensation of fused silica was investigated and experimentally demonstrated, greatly reducing the TCF of fused silica. From this, a method of further improving the stability was presented using acoustic engineering to create phonon-trapped dual-mode AlN-on-silicon resonators. These resonators can contain two simultaneous resonance modes in the same device volume, allowing for a temperature sensing mode and reference frequency to stem from a single device volume, reducing ovenization error and further improving device performance. By combining these methods into an ovenized platform using a high-quality, temperature compensated dual-mode resonator as both the temperature sensor and reference frequency, maximum stability can be achieved and comparable performance to ovenized quartz resonators can be achieved at a fraction of the size, power, and cost.

Experimental Verification of Charge Redistribution

As noted in Chapter 3, the currently measured charge redistribution results cannot be fully decoupled from the interface losses. Two interface regions on the devices, the Si/AlN interface and the AlN/Al interface, both contribute interface losses that complicate the results shown in Tables 3.5-3.7. Some method of decoupling these two losses is required to accurately verify the effects of charge redistribution on these devices. One potential method of decoupling is the use of optical interrogation and readout. This method allows for non-electrically complete devices to be measured, such as devices with no piezoelectric stack, or devices with just a Si/AlN interface. This can also be extended to directly compare the performance of a device between optical and electrical read-out methods. The comparison of Q for these device types will shine light on the effect of each additional layer, as well as allow for efficient comparison of interface loss versus the system presented in Chapter 3 which shows both interface and charge redistribution losses. In order to completely isolate the effect of charge redistribution in the AlN-on-silicon devices, it would be necessary to include an oxide layer between the Si/AlN interface to prevent the doping-enabled charges in the silicon substrate from causing additional charge redistribution. This would create additional layers in the structure and therefore increase interface losses, but an AlN-on-silica structure could be used instead to minimize the number of interfaces in the system. This would provide valuable data on the nature of loss in these resonators and move towards the verification of charge redistribution loss.

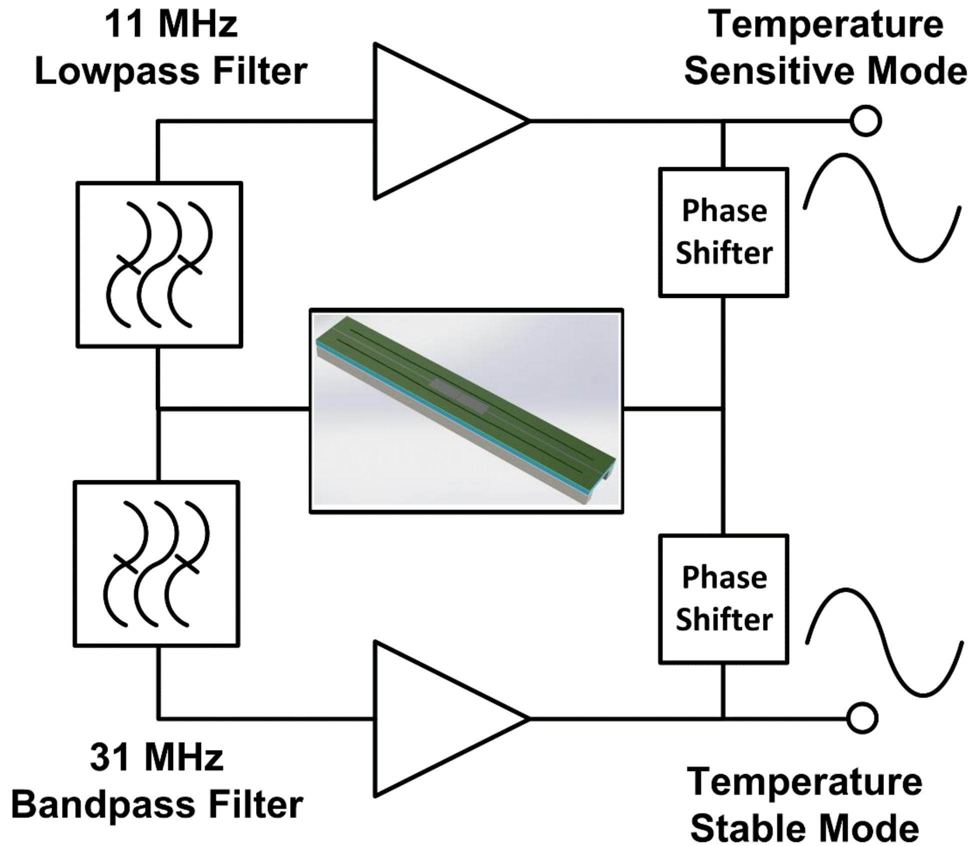

Fig. 6.1: A schematic of a dual-mode oscillator made from a single dual-mode phonon trapped resonator. Each amplification path is isolated through the use of a bandpass filter, leading to two separate output frequency signals with different temperature characteristics.

Implementation of Dual-Mode Acoustically Engineered Oscillators

Given the successful fabrication of dual-mode resonators, the next step in creating ultra-stable timing references is to design a system that can support two simultaneous resonance signals and process them into two unique oscillator outputs. Traditional oscillator circuits use an amplification method, typically an transimpedance amplifier (TIA) or high gain BJT, to amplify the signal and maintain the oscillation condition. For a dual-mode resonator, achieving a stable oscillation is slightly more complicated due to the multiple simultaneous signals. Because there are two electrical signals from the same device volume, a single amplifying path would “lock-in” to only one of the two signals, as only one can satisfy the oscillation critera at any given point. To get around this, two amplifying paths can be used to separate the two signals. Since the paths are

not electrically isolated both will contain two amplified signals, a bandpass or lowpass filter is added to supress the other branch and maintain the desired oscillation mode. With one filter on each branch, the signal for each mode is unique to that branch and will singularly satisfy the oscillation critera, creating two oscillating signals from a single device volume. A basic schematic of this dual-mode oscillator is shown in Fig. 6.1.

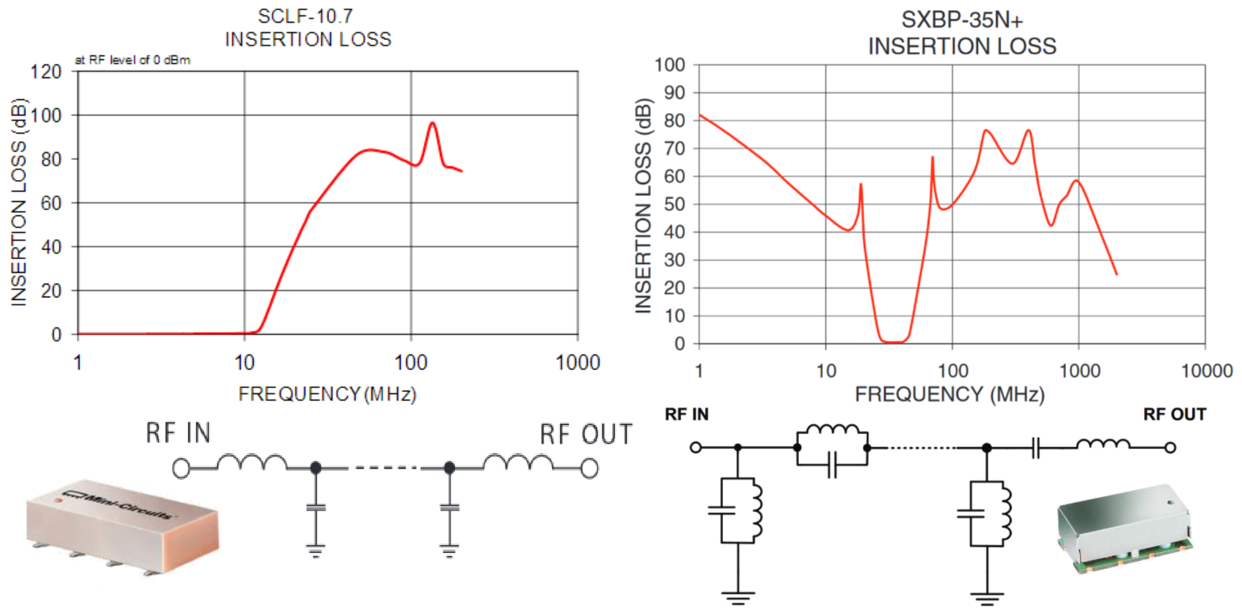

Fig. 6.2: Filter response for the 11 MHz lowpass filter and the 31 MHz bandpass filters provided through Mini-Circuits. Insertion loss is plotted versus frequency for both branches, while photographs of both surface mount filters and generalized layout for the LC filters are shown below. Images for lowpass filter adapted from [1] and 31 MHz filter adapted from [2].

The bandpass filters for these devices were chosen to minimize losses and maximize suppression of the other branch. For the first oscillator prototype filters from Mini-Circuits, SCLF-10.7 [1] and SXBP-35N+ [2], were chosen. These filters are LC type ladder filters that can be surface mounted onto a PCB for miniaturization and to allow for ovenized testing. A typical response for these circuits are shown in Fig. 6.2, where over 40 dB of rejection is shown for the 31 MHz mode from the 11 MHz branch and 40 dB of rejection is shown for the 11 MHz mode from the 31 MHz branch. Further work is ongoing to determine ideal bandpass filtering for these two branches, and a custom bandpass filter can be designed to further improve performance as needed.

A prototype circuit schematic for a dual-mode oscillator system using the schematic shown in Fig. 6.1 was created using commercial off the shelf components on a custom PCB. Each branch is amplified using a TI OPA 656 TIA [3] with a feedback resistor for stability, and a second-stage TI OPA 657 [4] where additional gain is required, such as in the 11 MHz branch. The gain provided by the OPA 656 is sufficient for the 31 MHz branch, whereas a dual-stage approach is needed for the 11 MHz approach to overcome the slightly larger insertion loss of that mode. In that case, the OPA 657 is used for additional voltage gain to ensure the oscillation conditions are met. A zero gain buffer using an OPA 656 is placed outside of the loop prior to oscillation output to buffer any output resistances from the final timing application. A schematic of this circuit layout is shown in Fig. 6.3. Implementation of this design is ongoing, and oscillator testing and optimization in necessary in order to maximize oscillator stability of this design.

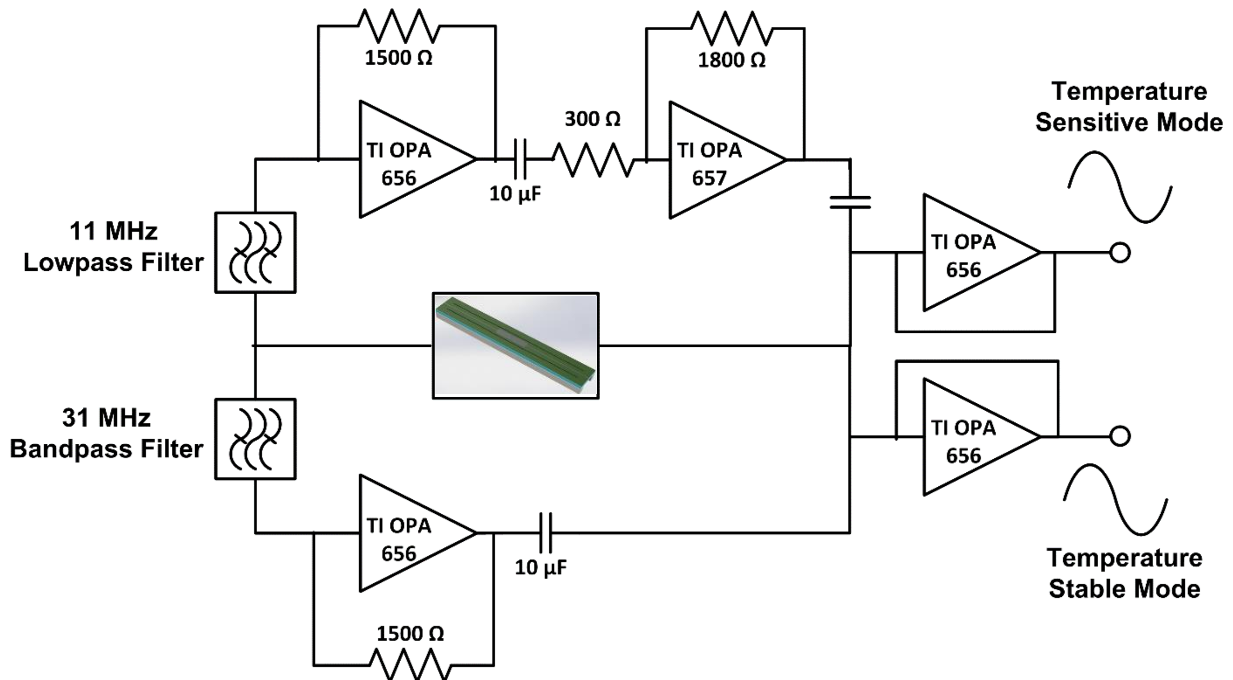

Fig. 6.3: Dual-mode circuit layout for the fabricated acoustically engineered resonators. Top branch is for the 11 MHz resonance mode and has two-stage amplification for extra gain. Bottom branch is for the 31 MHz mode and has only single stage amplification. Both output stages use a buffer prior to oscillator output.

Given the circuit prototype, the first step of the process is to test the oscillator branches singularly to ensure that the branches oscillate on their own. By isolating a single branch, in this

case the 31 MHz mode, oscillation of a single mode was achieved using the circuit schematic outlined in Fig 6.3. The measured power output of this oscillator is included in Fig. 6.4, showing a main peak at 30.83 MHz with its harmonics showing 30-40 dB lower signal power. The time domain response of the oscillator shown in the inset of Fig 6.4 shows a typical sine wave, suggesting successful suppression of harmonics due to the bandpass filter. A matching network was added to the branch to adjust for the 50 Ω termination of the filter on both the input and output ends of the filter. This matching network allows for proper input matching and prevents unwanted suppression of the oscillating mode.

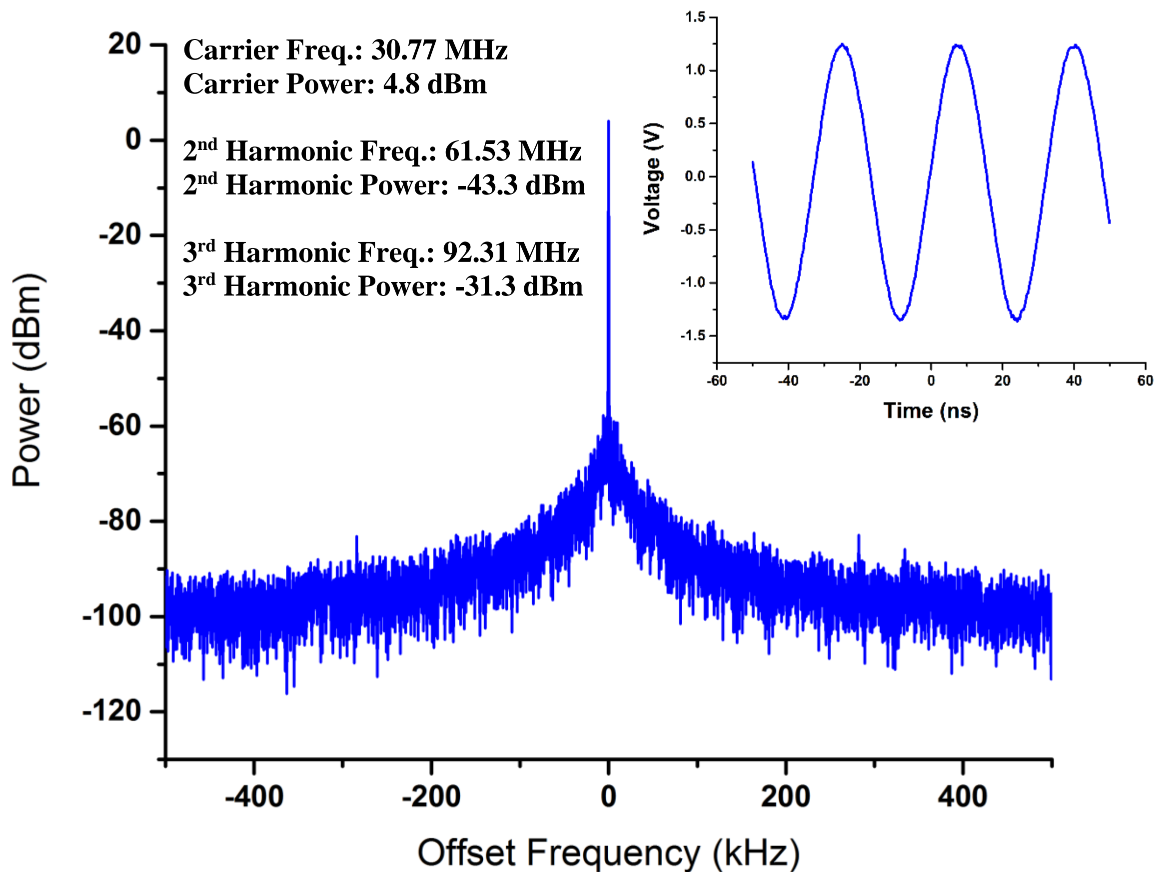

Fig. 6.4: Frequency spectrum measurement of the 31 MHz oscillator around its carrier frequency. The major harmonic frequency and powers are included in the left inset. Right inset shows a time domain measurements of the oscillator output showing a sine wave with little harmonic influence.

With successful oscillation of a single branch, the next step towards dual mode devices is to oscillate both branches simultaneously and test the efficacy of each filter in isolating the branches. This step needs to be done experimentally, as no simulation software currently exists that supports two simultaneous oscillations. The lack of simulation capability makes it difficult to iterate on the dual-mode oscillator architecture without extensive prototyping and testing, and adds to the complexity of implementation.

Dual-Mode Oscillators for Use in Ovenized Architecture

After successful testing and characterization of a dual-mode oscillator, it needs to be integrated into an ovenized architecture for maximum effect. There are two temperature sensing methods that could be utilized for this purpose, beat frequencies or phase locking. Beat frequencies use two modes that are of integer-divisible frequencies and use a mixer to linearly combine the two frequencies, creating a much larger TCF than either of the two input modes [5]. For example, if two modes exist that are integer multiples of each other so $f_2 = nf_1$, then when mixed the beat frequency $f_{total} = f_2 - nf_1$ with a 1 °C change in temperature gives:

$$f_{total}(1 + TCF_{total}) = f_2(1 + TCF_2) - nf_1(1 + TCF_1) \quad \text{(Equation 6.1)}$$

And by using the property $f_2 = nf_1$and rearranging:

$$TCF_{total} = \frac{f_2}{f_{total}}(TCF_2 - TCF_1) - 1 \quad \text{(Equation 6.2)}$$

It can be seen with these equations that a close match between f_1 and f_2 leads to a very small f_{total} and therefore an extremely large TCF_{total}. For the dual-mode devices shown in Chapter 5, the TCF difference shown there can be substantially amplified through this method. This has been shown in a similar dual-mode structure, achieving a beat frequency TCF of 8,300 ppm/K for two modes on an AlN-on-silicon platform [5]. This beat frequency will then function as a temperature sensor

for the ovenized resonator with little to no thermal lag, as both modes are contained on the same device.

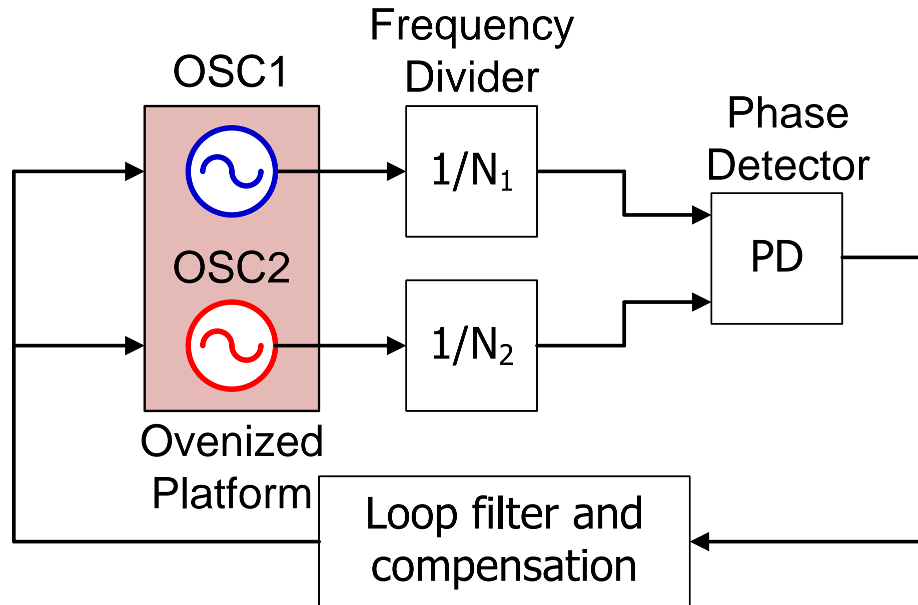

Fig. 5.5: A schematic for an ovenized platform architecture utilizing a phase detector as part of a PLL. The accuracy of this system increases as the TCF difference between the two modes increases. Image adapted from [6].

A second method to achieve temperature sensing with these two modes is through phase locking of the two MEMS oscillators. In this method, an arbitrary frequency divider is used to bring the frequencies together at the oven set temperature point, so integer multiples of frequencies are not required as in the beat frequency method. This single frequency is then run through a phase detector which detects any difference in phase between the two modes and adjusts the ovenization power to bring the phases back in line. A basic schematic of this setup is seen in Fig. 6.5. For best results, one resonator mode should be extremely stable, ideally ovenized at its turnover temperature, and the other mode with as high as TCF of possible. The large TCF difference creates the largest frequency shifts and therefore phase difference, improving accuracy. This method is more flexible and potentially more accurate at the cost of additional complexity and power

consumption. A more in depth discussion of the design consideration and accuracy can be seen in [6, 7], albeit for a two-resonator ovenized platform.

With a prototype ovenized implementation of the dual-mode resonator system, the next step is to translate this system to a fused silica platform. The dual-mode implementation of a fused silica system will follow a very similar design to that shown in Chapter 5, except with the use of nickel-refilled trenches as opposed to doped silicon. The same mode shapes can also be used, as the high-strain regions differ between the modes and so a TCF difference can be created. The acoustic engineering design method works regardless of material or crystallinity, and so the same phonon trapping method also applies. The use of fused silica over silicon is expected to improve performance in this case, as the larger natural TCF of fused silica allows for a larger TCF differential. Successful implementation of these ovenized dual-mode AlN-on-silica resonators would form the foundation of a batch-fabricated ultra-stable timing reference that shows performance at or above that of currently available ovenized quartz resonators.

References

[1] Mini-Circuits, "Surface Mount Low Pass Filter SCLF-10.7+," *Low Pass Filter SCLF-10. 7+ Datasheet,* REV. E M151107.

[2] Mini-Circuits, "Surface Mount Bandpass Filter SXBP-35N+," *Bandpass Filter SXBP-35N+ Datasheet,* REV. OR M112217.

[3] Texas Instruments, "OPA656 Wideband, Unity-Gain Stable, FET-Input Operational Amplifier (Rev. H)," *OP656 Datasheet,* Sep. 2015, 2015.

[4] Texas Instruments, "OPA657 1.6-GHz, Low-Noise, FET-Input Operational Amplifier (Rev. F)," *OP657 Datasheet,* Aug. 2015, 2015.

[5] R. Tabrizian and F. Ayazi, "Acoustically-engineered multi-port AlN-on-silicon resonators for accurate temperature sensing," in *Proceedings of the IEEE International Electron Devices Meeting (IEDM),* Washington D.C., USA, 2013, pp. 18.1.1-18.1.4.

[6] Z. Wu, "Microelectromechanical systems for wireless radio front-ends and integrated frequency references," *University of Michigan, Ph. D. Thesis,* 2014.

[7] Z. Wu and M. Rais-Zadeh, "A temperature-stable piezoelectric MEMS oscillator using a CMOS PLL circuit for temperature sensing and oven control," *Journal of Microelectromechanical Systems,* vol. 24, pp. 1747-1758, June, 2015.